A STUDY OF MEDIUM INDUCED JET MODIFICATION AT THE RELATIVISTIC HEAVY ION COLLIDER VIA TWO PARTICLE CORRELATIONS AND IDENTIFIED JET SPECTRA

by

ESSAM OTHMAN ELHALHULI

A thesis submitted to
The University of Birmingham
for the degree of
DOCTOR OF PHILOSOPHY

School of Physics and Astronomy
The University of Birmingham

November 7, 2010.

Synopsis

The production and subsequent survival of jets has been shown to be sensitive to the nature of the medium produced in high energy heavy ion collisions. This work has studied the particle composition of jets by determining the ratios $p^{\pm}/\pi^{\pm}$ and $K^{\pm}/\pi^{\pm}$ in $Au + Au$ and $d + Au$ collisions at $\sqrt{s_{NN}} = 200$ GeV measured by the STAR experiment at RHIC.

Jets were found by measuring the angular azimuthal correlation between particles at high transverse momentum. Jets were then identified by their back-to-back correlation. Differences in the jet hadrons ratios for the different colliding systems could indicate that the jet spectra have been modified by the presence of a deconfined medium, wherein parton degrees of freedom are manifest over nuclear rather than nucleonic scales. A technique was developed to identify charged particles using their specific ionisation measured in the STAR Time Projection Chamber (TPC).

Previous studies have shown strong attenuation of hadronic jets in central $Au + Au$ at RHIC. The requirement of a high transverse momentum trigger biases the measurement of jets to those emitted close to the surface of the medium when using hadron triggers. This thesis contains one of the first implementations of using direct photons to tag jets in heavy ion collisions. An attempt was made to extract a trigger sample rich in direct photons from neutral triggers.

The particle composition was studied for both the near side jet (particles associated along with a neutral trigger particle) and the away side jet (particles emitted close to π with respect to the trigger). The hadron ratios were calculated from the jet yields as a function of transverse momentum in each collision system. Although the away side yield is suppressed in central $Au + Au$ as seen in previous studies, there is no evidence that the relative particle yields are changed. No medium modification of the relative particles yields suggests that the fragmentation process is unchanged by the energy loss experienced in the medium. This implies that the high p/π ratio seen in earlier studies of central $Au + Au$ is caused by the underlying event and not by jet modification.

The hadron ratios for the three systems were found to be consistent with simulated $p + p$ events generated using the Pythia Monte Carlo event generator. This reinforces the conclusion that the fragmentation process is unchanged by interactions with the medium.

Author's Contribution

In 2006, when the electromagnetic calorimeter was fully installed, the author was assigned the task of studying two-particle correlations in $Au + Au$ collisions at $\sqrt{s_{NN}} = 200$ GeV using calorimeter triggers. After developing the correlation techniques using the 2004 $Au + Au$ data, the techniques were applied to the 2007 $Au + Au$ and 2008 $d + Au$ data.

In addition to the correlations, an analysis was developed to identify the charged hadron spectra using the specific ionisation measured in the STAR TPC in the relativistic rise region of the Bethe-Bloch formula. The analysis used calibrated Bichsel function (modified Bethe-Bloch calculation) predictions for charged kaons, charged pions, electrons and protons to identify particles.

To calibrate the TPC ionisation, neutral Λ particles were reconstructed in order to produce high purity samples of protons taken from the baryon daughter of the Λ decay. The cuts for identifying Λ particles were developed by colleagues studying strange particles directly.

Back-to-back azimuthal correlations between high transverse momentum hadrons were used to identify jets. The charged tracks that were deemed to be part of the jet were then identified using the technique developed using the energy loss data. From the identified jet spectra, the charged hadron ratios p/π and k/π could be determined. The determined hadron ratios were compared with simulated $p + p$ data.

As a member of the STAR collaboration, the author contributed to experimental operations. A continuous three week period was spent in 2007, where the author was part of the detector operating team. The task of a detector operator included monitoring the detectors, starting and shutting down the detectors, initialising data collection and responding to detector faults.

The author also contributed to the STAR collaboration through weekly phone conferences where analyses were discussed. The author participated in quarterly collaboration meeting and analysis meeting. The author presented a preliminary version of these results during the Hot Quarks 2008 conference at Estes Park, Colorado, USA.

Acknowledgments

I would like to acknowledge those who have contributed significantly to my project. Without doubt, this project would not be where it is today without the input and guidance of those mentioned below.

I would like to reserve my greatest thanks for my supervisor Peter Jones who on numerous occasions has shown his faith in me. Firstly, for allowing me to join the Nuclear Physics group after a difficult start to life at the University of Birmingham and then his continuing support and insight throughout the writing of this thesis. I feel I have learnt a lot from Peter throughout my analysis and I can only hope that my work has contributed to his wealth of knowledge.

Special thanks are reserved for those who I worked most closely with during my three years in the Nuclear Physics group. To Lee Barnby, with whom I spent many hours discussing the developments of my analysis and determining the path forward. Our discussions of family life were very insightful and assisted me in adapting to a new stage of my life. Thanks also to Léon Gaillard and Anthony Timmins who shared with me their analysis skills and subject knowledge during my first year. Léon and Anthony were always available to answer my questions, making my transition into the group far smoother and easier.

Last but certainly not least of those I worked closely with is Thomas Burton. Thomas's thorough approach to analysis and thirst for research certainly inspired my own research ambition. His superior knowledge of computing and his willingness to share that knowledge certainly improved my own understanding and allowed me to get beyond what at the time seemed insurmountable hurdles. I hold our many physics conversations as invaluable as they allowed me to improve my grasp of the subject I was studying.

I would like to thank members of the STAR collaboration that provided me valuable feedback and direction. Most notably I would like to thank Marco van Leeuwen and Jana Bielcikova who supported my work and provided guidance on how to take my analysis forward. I would like to thank Ahmed Hamed for his help with understanding the EMC detector and analysis methods. Others that I would like to thank are Matthew Lamont, Rene Bellwied, Helen Caines, Olga Barannikova and Lijuan Ruan for their discussions on my analysis.

Finally, I would like to thank EPSRC/STFC for providing the funding throughout my study in Birmingham.

Contents

List of Figures

Chapter 1

INTRODUCTION

The strong force continues to be a challenging and fascinating phenomenon to study. Unlike the weak or electromagnetic forces, the coupling constant for the strong force is large, hence strong interactions cannot be calculated using peturbative theories as the strong force potential diverges at large distances. Furthermore, strongly interacting particles or partons have not been observed individually as they are confined within hadrons. The inability to observe partons in isolation limits any experimental investigation into how they behave.

In 1973, Gross and Wilczek proposed that non-Abelian gauge theories have free field theory asymptotic behaviour [1]. This discovery suggested that above a critical density, greater than that found in the nucleus, partons would become deconfined from their hadronic states. High energy nucleus-nucleus collisions provide a unique opportunity to study this novel state of matter.

1.1 Quantum Chromodynamics

The theory governing the strong force is Quantum Chromodynamics (QCD). The strong force binds together quarks to form colour neutral hadrons. Quarks carry one of six possible colour charges, analogous of electric charge, that are symbolised as red, blue, green and their corresponding anti-colours. By using colours it can be easily seen how combining quarks of different colour charge can lead to colour neutral hadrons.

Hadrons are either mesons, a colour-anticolour combination of a quark-antiquark, or baryons, three quarks, one of each colour. These are the two simplest colour neutral combinations that are possible.

1.1.1 Gauge theory of the strong interaction

The behaviour of interacting particles can be described by specific quantum field theories known as gauge theories. The strong force is one of the gauge theories tested by experiment. In gauge theories, the interactions between matter particles is generated by the exchange of gauge bosons, or force particles. QCD has been established as a gauge invariant theory based on a group of symmetries. Local gauge invariance implies that the QCD gauge boson is massless since a mass term in the QCD Lagrangian would render QCD not invariant under local gauge transformations [2].

The gauge boson in QCD is the gluon and it is responsible for mediating the strong force. Unlike the photon, the gauge boson of the electromagnetic force, that does not carry electromagnetic charge, the gluons do carry colour charge. Colour charge is conserved by the strong interaction. Figure 1.1 shows how a strong interaction between two quarks can conserve colour using a coloured gluon. The inclusion of gluons in the theory of hadons led to the development of the quark parton model [3].

Experimental evidence for gluons came from e^+ + e^- collisions. The hadrons produced by the collision were found in some events to be localised into three streams of hadrons, jets, violating any gluon free parton model where $e^+e^- \to q\bar{q} \to q\bar{q}g$ [4].

As colour charge exhibits a SU(3) symmetry, there can be eight linear combinations of colour that correspond to coloured gluons. Coloured gluons are able to interact with one another making QCD an example of a non-abelian Yang-Mills theory [5]. It is this property of gluons that complicates the long range component of the strong potential.

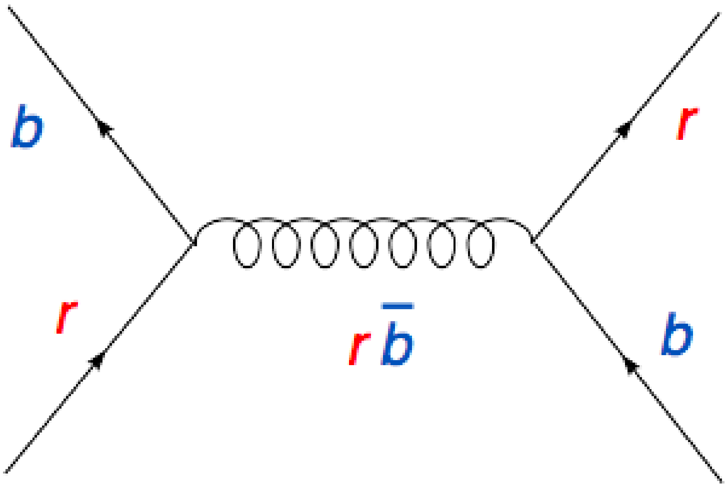

Figure 1.1: A Feynman diagram illustrating a strong interaction where colour is exchanged via a gluon. The quarks are represented by the arrowed lines and the gluon is represented by the looped line

1.2 The Strong Potential

A potential, which governs the spatial dimensions of hadrons, is created by strongly interacting quarks. If a quark anti-quark pair of a meson is considered, the resulting potential can be described by equation 1.1:

$$V(r) = -\frac{4\alpha_s(r)}{3r} + kr \tag{1.1}$$

where r is the quark spacing, α_s is the strong coupling constant and k is a constant that describes the long range interactions. At short distances, strong interactions can be described by the exchange of a single gluon with the resulting potential exhibiting a $\frac{1}{r}$ dependence. However, at larger separations, the strong potential takes on a different form. Increasing the separation increases the strength of the force binding the quarks together. Gluons carry colour and consequently they self interact. At large separations the gluon field collapses into a flux tube between the two quarks. The resulting potential follows a linear dependence with r. This long distance behaviour of the strong force confines quarks and gluons to hadrons and accounts for why free colour charges have not been observed in experiment.

1.2.1 Confinement and the running coupling constant

Confinement is the phenomenon that has prevented individual quarks from being isolated. Naively speaking, equation 1.1 suggests that an infinite quantity of energy is required to remove a quark from a hadron. Yet it is evidently possible to create particles from high energy collisions questioning the notion that quarks are forever bound to a specific hadron. As the quark separation increases, at some threshold, the creation of more particles is energetically more favourable than maintaining the original hadron structure.

A possible second conclusion that could be taken from equation (1.1) is that as $r \to 0$ the repulsive force due to the first term on the right hand side becomes infinite. However α_{s} is known from experiment to change as a function of the separation r and is described as a running coupling constant [6]. Working at leading order $\alpha_{\mathrm{s}}(Q^2)$ can be described by equation 1.2.

$$\alpha_s(Q^2) = \frac{\alpha_s(Q_0^2)}{1+\beta_0\alpha_s(Q_0^2)ln(Q^2/Q_0^2)} \tag{1.2}$$

In equation 1.2, $\beta_0 = \frac{11C_A - 4T_F n_f}{12\pi}$ where $C_A = 3$ and $T_F = \frac{1}{2}$ are the conversion factors of a gluon splitting into two gluons or two quarks respectively and n_f is the number of quark flavours used in the calculation. Using the value of a measured strong coupling constant at a known Q^2 scale, $\alpha_{\mathrm{s}}(Q_0^2)$, it is possible to solve $\alpha_{\mathrm{s}}(Q^2)$ at any higher value of Q^2 where Q^2 is greater than Q_0^2 and perturbative methods are valid.

The critical observation taken from this equation is that as $Q^2 \to \infty$, $\alpha_s \to 0$. Considering that $Q^2 \propto \frac{1}{r^2}$, the strong interaction asymptotically decreases as $r \to 0$. Experimental studies at LEP have indeed shown that α_s decreases with increasing Q^2 [7].

1.3 Quark-Gluon Plasma

Given that at high Q^2 the strong coupling constant decreases asymptotically, as described in section 1.2.1, one could hypothesize that the strong interaction would become negligible at very small separations. A vanishing coupling constant would allow quarks and gluons to become deconfined, meaning that hadrons would cease to exist. In other words, a new state of nuclear matter, with free quarks and gluons demonstrating colour degrees of freedom, could be observed. In 1975, Collins and Perry realised that asymptotic freedom implied that quarks could become deconfined in the centre of stellar objects such as neutron stars, black holes or the early universe [8]. This new state of matter is commonly referred to as a Quark-Gluon Plasma (QGP). For asymptotic freedom to occur the hadronic matter must be subject to extreme pressures that compress the matter beyond a critical energy density. The critical conditions may be created in heavy ion collisions if the critical energy density can be exceeded.

1.3.1 Debye Screening

In a sufficiently high energy nuclear collision, matter is compressed beyond a density where hadron boundaries overlap. The increased density of colour charges perturbs the potential within each hadron. The long range component of the strong potential within the hadron is screened by the presence of extra colour charge. This screening effect results in the deconfinement of strongly interacting particles that can now propagate through the critically dense matter. The medium would transform from a colour insulating material (normal nuclear matter) to a colour conducting material similar to the Mott transition where insulators transform to conductors when subjected to high external pressure [9].

The potential between nuclei and outer lying electron orbitals is rewritten to include a Debye screening effect. Equation 1.3 illustrates how the density of charge perturbs the effective potential experienced by electrons in the outlying orbitals where r_D is the Debye screening length, k_B is the Boltzmann constant and ρ is the density of electrons. The QCD Debye screened potential shown in equation 1.4 is very similar to equation 1.3 [10]. The primary consideration is that the linear term in equation 1.1 vanishes when the quark separation is much less than the radius of a hadron, due to the overlapping hadronic wave functions, leaving only the Coulomb-like potential. The onset of Debye screening allows deconfinement, and thus QGP formation, to occur at an energy density that may be achieved in high energy nuclear collisions.

$$^{QED}\phi(r,T) = \frac{Q}{4\pi\varepsilon_0 r} e^{\frac{-r}{r_D^{QED}(T)}} \tag{1.3}$$

$$r_D^{QED} = \sqrt{\frac{\varepsilon_0 k_B T}{\rho e^2}}$$

$$^{QCD}\phi(r,T) = \frac{1}{9T^2}\alpha_s(T)^2 e^{\frac{-r}{r_D^{QCD}(T)rT}} \tag{1.4}$$

$$r_D^{QCD} = \frac{1}{\sqrt{4\pi\alpha_s(T)}T}$$

1.3.2 Lattice QCD

Lattice QCD is a non-perturbative method of performing QCD calculations. The lattice grid consists of quarks and gluons, where the quarks are represented by the lattice points and the gluons are the links between each point. The spacing of the lattice points dictates the momentum for the lattice as the momentum is of the order $1/a$, where a is the lattice spacing.

Calculations are computationally intensive and are generally limited to small lattices. Calculations performed on different size lattices gives an indication of the sensitivity of the lattice size.

By performing calculations at several lattice spacings, extrapolation to the continuum of lattice spacings, by letting $a \to 0$, can be performed to determine physical properties that are a function of a. Lattice QCD presents a useful tool for investigating the properties of the QGP.

Lattice QCD calculations have provided estimates of the critical parameters necessary for nuclear matter to transform into a QGP. The critical temperature T_c for the phase transition has been calculated using 2 and 3 quark flavour senarios and has been determined to be in the region $T_c \sim 150 - 175$ MeV. The critical energy density ε_c predicted by lattice QCD is $\sim 0.7\ GeV fm^{-3}$ [11].

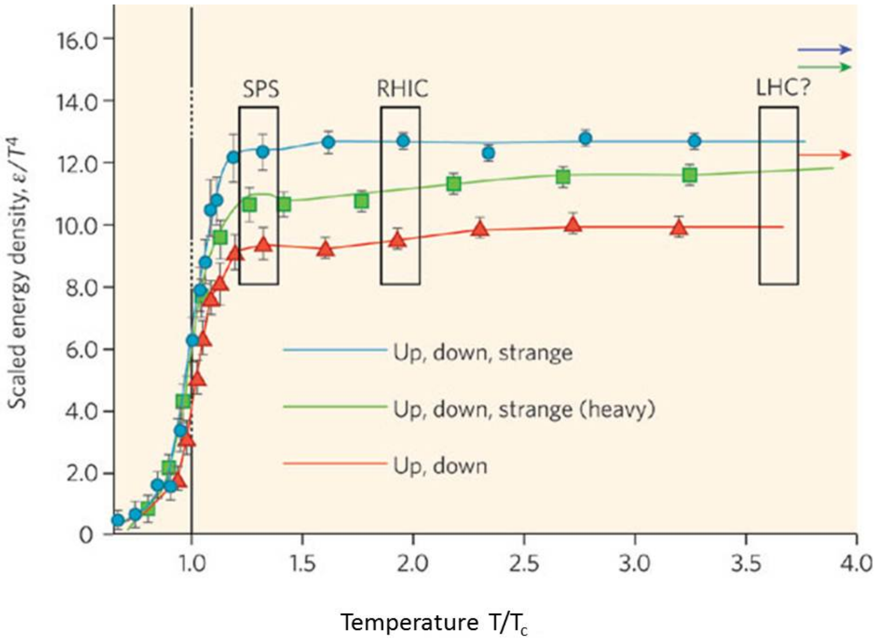

Figure 1.2: Energy density lattice QCD calculations as a function of the critical temperature for the formation of a QGP. The three coloured arrows indicate the relativistic Stefan-Boltzmann predictions. Also shown are the predicted temperatures for three heavy ion experiments [13]

What can be seen from the lattice calculations in figure 1.2 is that as the temperature reaches T_c there is a sharp increase in the energy density indicating an increase in the number of degrees of freedom. At the asymptotic limit, $\alpha_s \to 0$ where the strong force is negligible, quarks and gluons can be described as point-like non interacting particles much like in an ideal gas. In this case the relativistic Stefan-Boltzmann law can be used to describe how the pressure p_{SB} of the matter relates to the temperature T [12].

$$\frac{p_{SB}}{T^4} = \left[2(N_c^2 - 1) + 2N_c N_f \frac{7}{4}\right] \frac{\pi^2}{90} \tag{1.5}$$

The two terms in the bracket of equation 1.5 sum the contribution of the gluons and quarks where N_c is the number of colours and N_f is the number of quark flavours. From equation 1.5, the energy density, ε, for a relativistic gas can be computed using the relationship $\varepsilon = 3p_{SB}$.

When comparing the results for a ideal relativistic gas at T_c to the results obtained from lattice QCD, figure 1.2 shows there is clearly a deficit in ε from the lattice QCD calculations. This deficit was originally dismissed as a limitation of lattice QCD but is now believed to indicate that the partons are not asymptotically free and continue to interact strongly. The sharp increase in ε, after the critical temperature, remains indicative of a phase change from a hadron gas to a new state, possibly a QGP, as this sharp increase would be due to the liberation of new degrees of freedom. The onset of this new phase is likely to be the result of colour screening as described in section 1.3.1. There remains the possibility that at temperatures much greater than T_c, perhaps those obtainable at the LHC, asymptotic freedom could be established before then cooling to a state where screening allows for deconfinement and then finally freezing out to a hadron gas.

1.4 Relativistic Heavy Ion Collisions

A series of images taken from a simulation of a relativistic heavy ion collision, illustrating the various stages of the temporal evolution, is depicted in figure 1.3. The incoming ions are Lorentz contracted in the centre of mass frame forming two disks. Hard scattering (high Q^2) elastic collisions can occur in the initial interaction. Soft (low Q^2) interactions also occur leaving a dense medium of gluons in the wake of the collision. These gluons can fuse or fragment to $q\bar{q}$ pairs producing further quarks and gluons. If the critical energy density is achieved, hadronisation is delayed and a deconfined phase will form. A QGP will have been achieved once the dense medium has reached thermal equilibrium. The QGP will expand and cool due to internal pressure and will eventually form a hadron gas. The time scales required for the evolution of the collision are calculated using hydrodynamic models that rely on the system reaching thermal equilibrium [14]. Current studies of the medium produced in Au + Au collisions at a centre of mass energy per nucleon ($\sqrt{s_{NN}}$) = 200 GeV at RHIC suggest that the matter produced is thermally equilibrated very early in the evolution as will be discussed in chapter 2. Unfortunately the QGP can not be observed directly by experiment. The detectors used in heavy ion experiments detect the $\sim$1000 particles that are produced after the expansion. The goal of experiments is to search for experimental signatures of quark deconfinement.

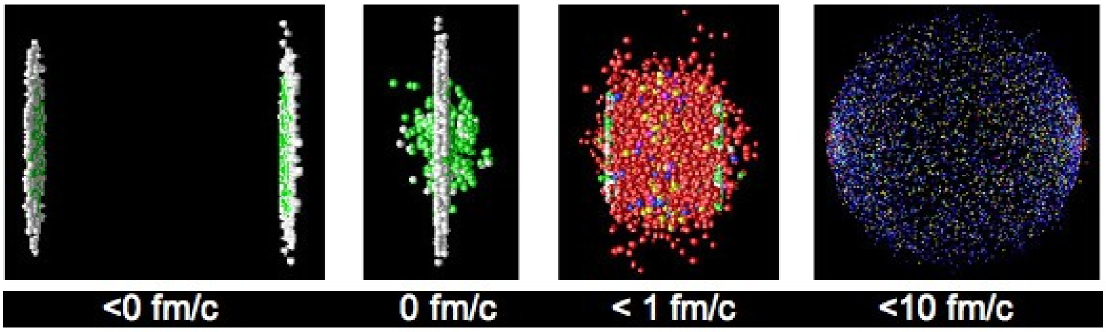

Figure 1.3: Simulation of a relativistic heavy ion collision showing the various stages of the temporal evolution as seen from the centre of mass frame [15]

1.4.1 Heavy ion experiments

Heavy ion experiments have been conducted since the 1980s. The Bevelac accelerator at the Lawrence Berkley National Laboratory was the first heavy ion facility, colliding a beam of ions with a fixed target that could achieve a $\sqrt{s_{NN}}$ of 2.5 GeV. The Alternating Gradient Synchrotron constructed at Brookhaven National Laboratory in the late 1980s was another fixed target facility obtaining a $\sqrt{s_{NN}}$ of 4.9 GeV. The SPS at CERN could reach a $\sqrt{s_{NN}}$ of 17 GeV. RHIC, the first purpose built collider designed to investigate nuclear matter at high temperature and density commissioned at Brookhaven National Laboratory in 1999, has a $\sqrt{s_{NN}}$ of 200 GeV. RHIC consists of two concentric rings that collide two ion beams, thus enabling a much larger centre of mass energy to be achieved than fixed target experiments.

Relativistic heavy ion collisions, created in modern particles accelerators, are believed to be capable of reaching the critical temperature, estimated by lattice QCD, for the onset of a QGP phase. Two accelerator facilities have calculated a temperature above this critical temperature. They are the CERN Super Proton Synchrotron and the Relativistic Heavy Ion Collider (RHIC) at Brookhaven National Laboratory.

The QCD phase diagram shown in figure 1.4 illustrates the phase boundary between hadrons and a QGP. The red labels indicate the chemical freeze-out temperatures of subsequent collider facilities. As the chemical freeze-out temperature at RHIC has been determined to be approximately equal to the critical temperature, the initial temperature after the collision must have been higher, which suggests that a QGP phase has been created.

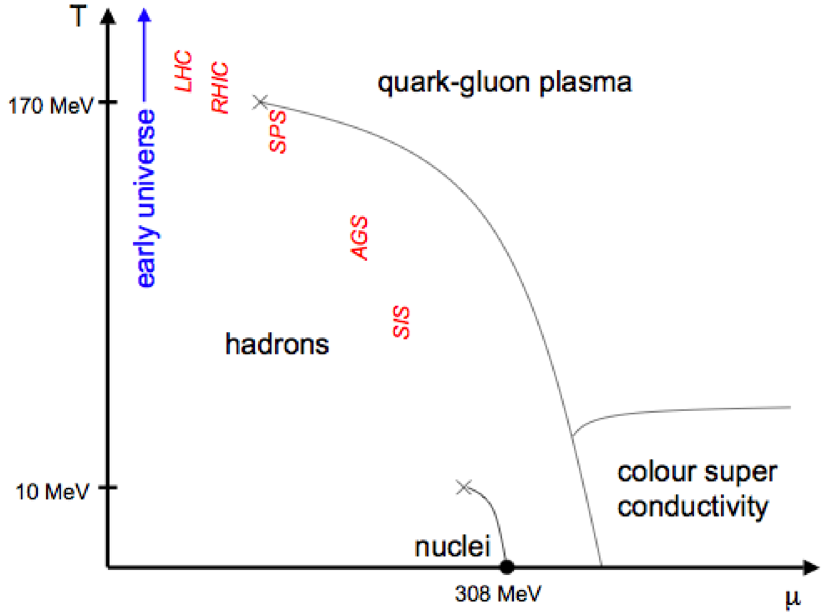

Figure 1.4: The QCD phase diagram showing the boundary between a hadronic state and a QGP state of matter. The chemical freeze-out temperatures of different experiments are indicated by the red labels.

The CERN Large Hadron Collider is expected to produce collisions temperatures in excess of those currently being produced at RHIC. Figure 1.2 shows where the calculated temperatures of these three heavy ion accelerators lie on the lattice QCD T_c calculations. Judging by these calculations, the critical temperature has indeed been surpassed. However verifying that a temperature above T_c has been reached would not be sufficient evidence to prove that deconfinement has been achieved.

There have been four experiments running during the RHIC operating period yet only the STAR experiment shall be discussed in detail as the research entailed in the following chapters was conducted using data taken by the STAR experiment. A summary of the results taken from the first five years of RHIC operations has been published by each experiment: BRAHMS, PHENIX, PHOBOS, and STAR [16, 17, 18, 19]. A detailed description of the RHIC facility and the STAR experiment will follow in chapter 4.

1.5 Thesis Outline

The matter created in heavy ion collisions at RHIC can be studied by analysing jets created during the initial collision. Jets are streams of correlated particles that are created from the fragmentation of high momentum partons, which have been scattered through large angles during the initial collision. A high momentum parton will traverse the medium created in the collision and will act as a *probe* whose information can be detected once it has fragmented into a jet.

Jet modification, as a consequence of high transverse momentum suppression in $Au + Au$ collisions, is one of the key results taken from RHIC and will be discussed in detail in section 2.1. The present analysis will investigate jet modification by searching for a modification signature in the spectra of particles associated with jets. By distinguishing jet cone hadrons from hadrons produced in the underlying event, it will be possible to determine whether modification of the hadronic composition of jets has occurred in $Au + Au$ collisions.

Four different collision systems will be compared to study jet modification in relation to system size. Identified spectra shall be obtained for jets found via two particle correlations from d+Au, central and peripheral Au+Au and simulated Monte Carlo $p + p$ collisions at $\sqrt{s_{NN}} = 200$ GeV.

This thesis comprises of the following chapters. Chapter 2 will summarise the key results from RHIC that have an impact on the current analysis. Chapter 3 will discuss the theory of jet phenomena focusing on jet production and jet modification. Hadron production via fragmentation shall be discussed along with possible modification mechanisms to in vacuum hadron production by the presence of a deconfined medium. Chapter 4 will introduce the RHIC facility and the STAR experiment. There will be a comprehensive review of the detectors key to this analysis. Furthermore, the analytical methods for two particle correlations and hadron identification shall be discussed. Chapter 5 shall provide a precise account of the analytical procedure used to extract the identified spectra from jets. In chapter 6, the results from comparing the hadron composition of jets from four systems will be discussed and the limitations of the methods used shall be scrutinised. Finally, an outlook is proposed that considers the potential for further studies on jets with a look to the capabilities of future heavy ion experiments.

Chapter 2

KEY RESULTS FROM RHIC

Before continuing with the key results, a few key parameters must first be defined. The first parameter is the particle momentum perpendicular to the beam axis, which is the transverse momentum and will be denoted as p_T. The second parameter is rapidity, y, and is calculated as shown in equation 2.1 where E is the energy of the particle and p_L is the particle's longitudinal momentum.

$$y = \frac{1}{2} ln \left(\frac{E + p_L}{E - p_L} \right) \tag{2.1}$$

Pseudorapidity, η, is often used in place of rapidity in the limit where the particle is traveling close to the speed of light or in the approximation that the mass is negligible. η is calculated as shown in equation 2.2 using the particle momentum instead of the energy. Rapidity is a useful tool for measuring the angle of a particle relative to the beam axis.

$$\eta = \frac{1}{2} ln \left(\frac{|p| + p_L}{|p| - p_L} \right) \tag{2.2}$$

2.1 Suppression of High Transverse Momentum Hadrons

The suppression of high p_T hadrons, via hard scattering collisions with partons in the medium, was one of the earliest predicted signatures of a QGP [20]. To quantitatively observe high p_T

suppression, a $p + p$ reference spectra at the same centre of mass energy must be taken to compare with the $Au + Au$ spectra.

In heavy ion collisions there are far more particles produced than in a $p + p$ collisions therefore a suitable scale is required to accurately account for the enhanced particle production due to larger colliding bodies. In the high p_T region, the number of hadrons scales approximately with the number of nucleon-nucleon binary collisions (N_{bin}) [21]. Thus a nuclear modification factor (R_{AA}) is formalised in equation 2.3 where N^{AA} is the hadron yield from *nucleus* + *nucleus* collisions, y is the rapidity or pseudorapidity and N^{pp} is the hadron yield from *proton* + *proton* collisions, which has been scaled by the number of binary collisions.

Within the high p_T region, $Au + Au$ yields should scale to unity with $p + p$ yields in the absence of phenomena unique to heavy ion collisions. At p_T less than $\approx$ 1 GeV/c binary scaling is not an applicable scaling parameter as soft scattering is the dominant hadron production channel. A better scaling parameter for soft scattering production is the number of participating nucleons (N_{part}) in the collision.

$$R_{AA}(p_T, y) = \frac{d^2N^{AA}/dp_T dy}{\langle N_{bin}\rangle d^2N^{pp}/dp_T dy} \tag{2.3}$$

The suppression of high p_T hadrons is shown in figure 2.1. A suppression is shown as the R_{AA} decreases from unity with impact parameter suggesting that a final state interaction with the medium is the cause of the suppression. However, the initial state of the colliding nuclei may still affect the final state observables. The parton distribution function (PDF) describes how the momentum is distributed amongst the partons within a hadron or nucleus. Gluon saturation at low x, where x is the fraction of the hadron longitudinal momentum (p_L) carried by the parton, is a possible candidate for the suppression of high momentum hadrons when comparing $Au + Au$ and $p + p$.

The possible gluon saturation effects can be investigated using a deuterium probe. A suppression of high p_T hadrons in $d + Au$ collisions would strongly indicate that the suppression is due to initial state effects as no QGP will form in these collisions. The $d + Au$ analysis indicated an enhancement of high p_T hadrons when compared to $p + p$ data [22]. The enhancement can be

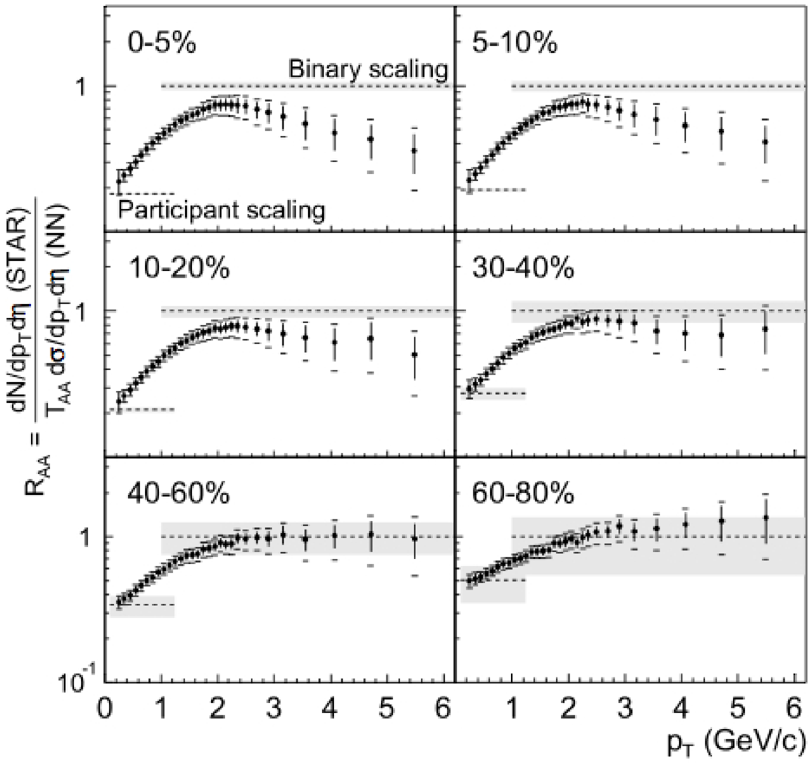

Figure 2.1: R_{AA} for various p_T bins taken from STAR $Au + Au$ collisions data at $\sqrt{s_{NN}} = 130$ GeV [24]. High p_T suppression is shown to increase with centrality, where 0-5% reprsents the most central collisions and 60-80% represents the most peripheral bins.

attributed to the Cronin effect, where the multiple scattering of colliding partons increases the momentum that is transferred into the transverse plane [23]. The $d + Au$ result indicated that the suppression of high p_T hadrons is a final state effect, which supports the hypothesis that a QGP has been formed at RHIC. At low p_T, where soft scattering production dominates the particle spectra, an enhancement is observed in figure 2.1 above participant scaling. The enhancement indicates that the Cronin effect is also present for $Au + Au$. Intuitively, the suppression at high p_T must therefore be larger than the observed factor of five suppression.

A further study to determine the initial/final state effects on high p_T suppression computed R_{AA} for direct photons [25]. Photons do not interact strongly and therefore would be largely unperturbed by the presence of a strongly interacting medium such as a QGP. The analysis carried out by the PHENIX collaboration clearly illustrated that the direct photon yield scales with the number of nucleon-nucleon collisions across all impact parameters. In tandem to the analysis on direct photon production, the hadron yields for the η and π^0 neutral mesons were calculated. Figure 2.2 shows

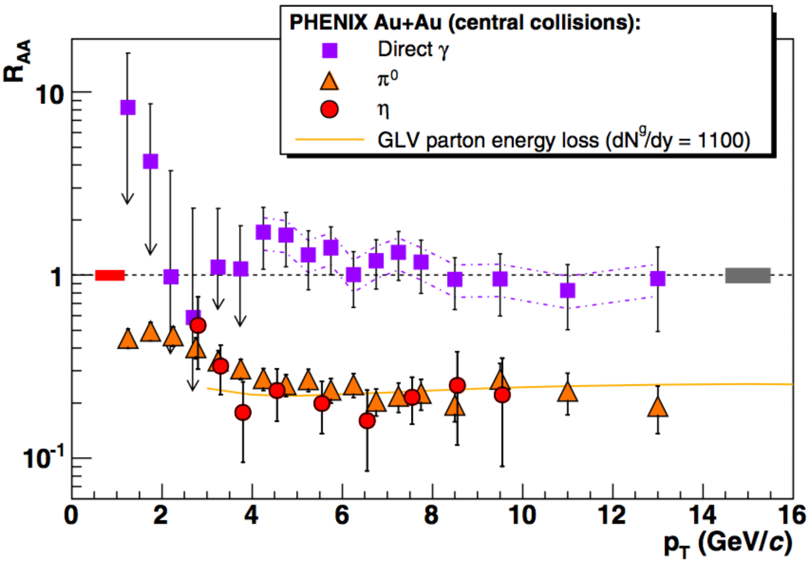

Figure 2.2: PHENIX data showing the R_{AA} for η, π^0 and direct γ [26]. The neutral hadrons exhibit similar suppression in central $Au + Au$ as charged hadrons however the photons show no indication of suppression.

how neutral mesons exhibited a similar suppression profile to the charged particles reinforcing the conclusion that the final state suppression is caused by a strongly interacting medium [26].

2.1.1 Suppression of dijets

When a high Q^2 collision between two partons occurs the partons are often scattered through large angles and propagate back-to-back in the transverse plane. Yet, due to confinement, they cannot exist as free partons. Therefore the two partons fragment into further partons that hadronise to form a cone of new hadrons or a jet. The fragmentation process liberates the scattered parton from the parent hadron, which incidentally will also fragment because the hadron remnant now contains net colour. The hard scattering process that creates dijets occurs during the initial stages of the collision. When the temporal and spatial evolution of the collision are considered, a hard scattered parton would still be within the medium when the QGP state exists.

The QGP formation time T_f can be loosely considered to be less than the hadron formation time (1 fm/c) as quark and gluon creation is an intermediate step to hadronisation. The life time of the QGP phase is dependent on the initial temperature and the rate of expansion and has been calculated for

RHIC energies to be between 3-4 fm/c [27]. If it is assumed that a static QGP has a radius equal to r_{Au}, which is roughly 7 fm, a high p_t parton created at T_0 at the centre of the collision with a trajectory in the transverse plane would encounter QGP matter. Consequently, dijets provide a useful probe of the QGP that had not been available at heavy ion experiments prior to RHIC.

Jet reconstruction is not possible in heavy ion collisions at STAR using traditional jet finding algorithms from hadron-hadron or lepton-hadron collisions due to the large particle multiplicity [28]. The hadrons that make up the jet cone are indistinguishable from the hadrons that form the underlying event. Two particle correlations that consider the angular distribution of particles with respect to the highest p_T particle in the event have been successfully used to indirectly measure a jet signal averaged over many events ($\sim 10^6$ events). Conservation of transverse momentum requires dijets to appear back-to-back in the transverse plane with respect to the beam axis.

In $p + p$ collisions dijets are created via the hard scattering of two impacting high momentum partons that then fragment in the vacuum. In the context of a $Au + Au$ collision, the high momentum scattered parton strongly interacts with the free colour charges of the QGP via scattering or radiating gluons much like an electron radiates photons when in the presence of an electromagnetic plasma via Bremsstrahlung [29]. If the jets have differing path lengths in the QGP, the jet with the longer path is likely to be more suppressed than the other. The trigger selection process for two particle correlations studies strongly favours the jet with the shortest path length.

The STAR collaboration reported a disappearance of back-to-back jets in central $Au + Au$ collisions at $\sqrt{s_{NN}} = 200$ GeV [30]. Figure 2.3(a) shows the result of a two particle correlation where $\Delta\phi$ is the angular distribution of particles relative to a trigger particle. The trigger particle is usually the highest momentum particle in the event which is the best candidate for the leading particle of a jet. The second jet, located at $\Delta\phi = \pi$, vanishes, within a certain p_T range, in the most central events and reemerges in the most peripheral events. Figure 2.3(b) displays the ratio of the corrected $Au + Au$ jet yield to the $p + p$ jet yield, I_{AA}, where the jet yield is the integral of the peaks in figure 2.3(a) above the flow background. I_{AA} is shown to decrease with N_{part} for the away side jet. There is a suggestion that the suppression observed in the lowest N_{part} bin is due to initial state effects implying that although perhaps not the dominant mechanism, initial state conditions contribute to

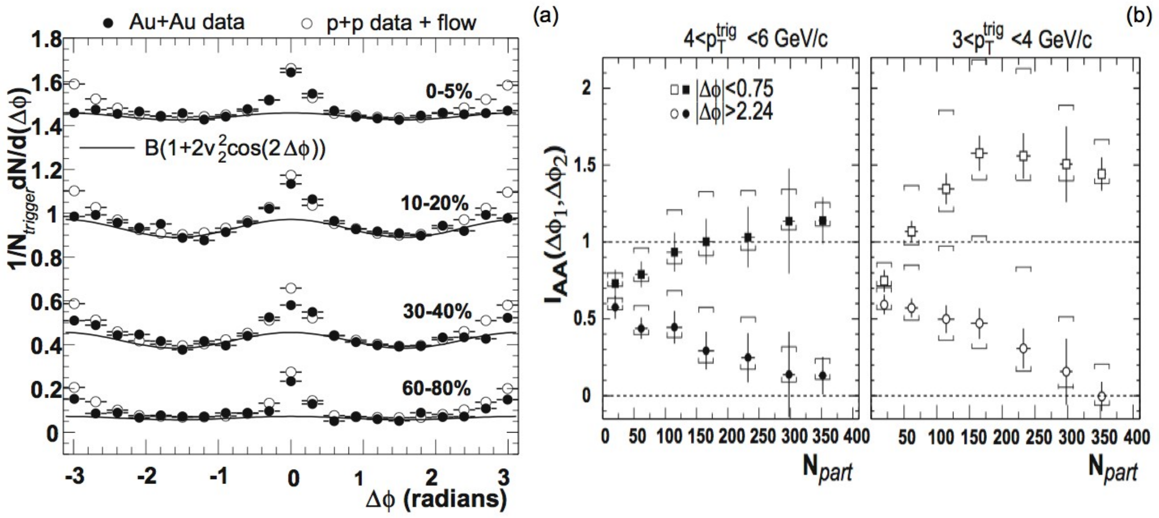

Figure 2.3: Suppression of back-to-back dijet correlation in $Au + Au$ collisions data at $\sqrt{s_{NN}} =$ 200 GeV [30]. Figure (a) compares the $Au + Au$ correlation (black circles) to the $p + p$ correlation (white circles) showing a suppression of a jet signal at $|\Delta\phi| = \pi$. Figure (b) compares the I_{AA} for near side jet ($|\Delta\phi| < 0.75$) and away side jet ($|\Delta\phi| < 2.24$) illustrating that the suppression is manifest in the away side jet.

the overall high p_T suppression observed in $Au + Au$ collisions.

2.1.2 Observation of dijets

The disappearance of the dijet signal was found only within a certain p_T range. When higher p_T hadrons are considered, it was found that the dijet signal reemerges albeit suppressed in central $Au + Au$ [31]. The two particle correlations for $d + Au$, mid-central $Au + Au$, and central $Au + Au$ are compared in figure 2.4. The combinatoric background in central $Au + Au$ reduces as the associated p_T increases due to a sharply decreasing contribution to the correlation from thermal hadrons. The return of the dijet signal can be attributed to both high energy jets that have not been fully suppressed and tangential jets that have had little or no interaction with the medium.

The reemergence of the away side jet at high p_T has strong implications for the current analysis. If the away side jet was completely suppressed at all associated p_T ranges, a jet yield could not be determined for the away side jet and therefore no analysis of the hadron spectra, associated with the away side jet ,could be performed.

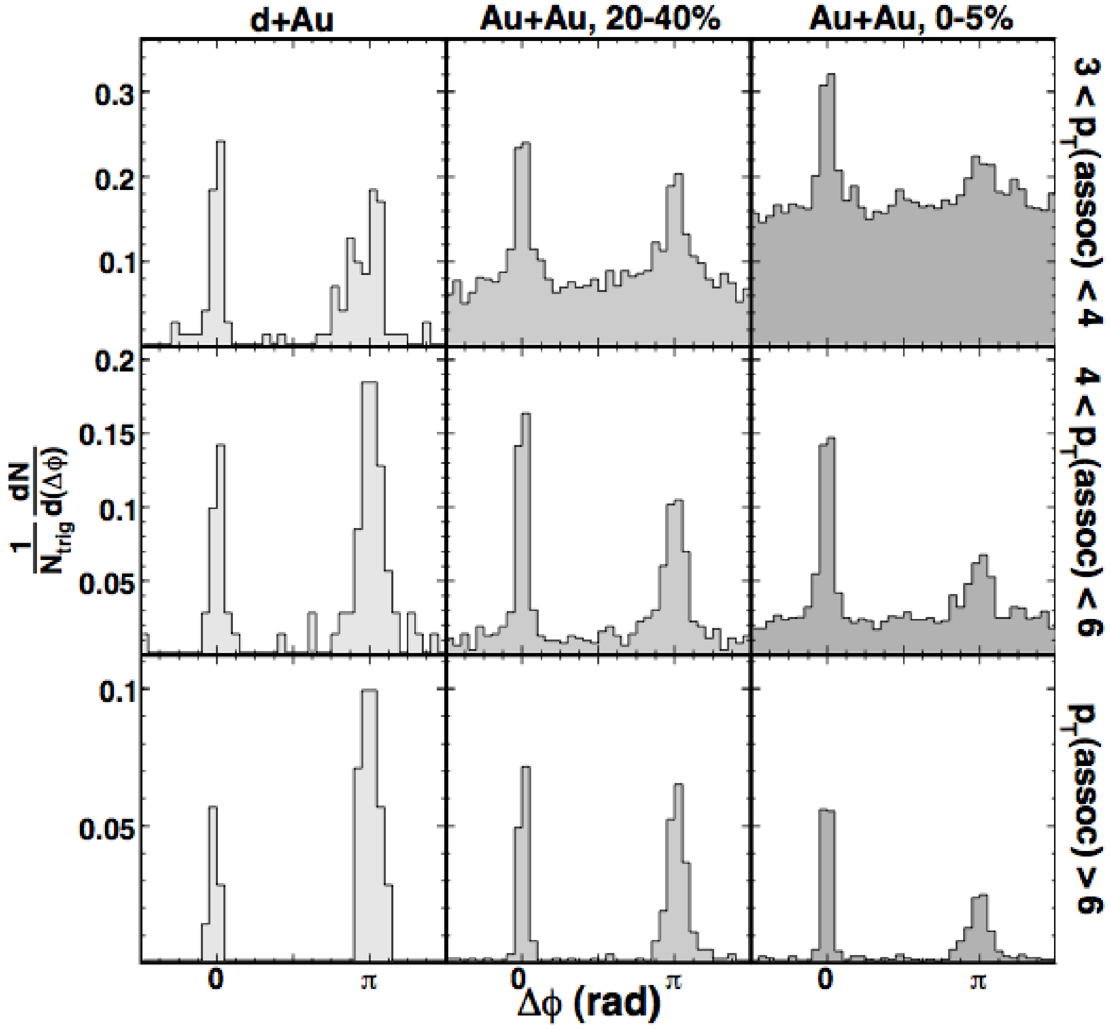

Figure 2.4: Azimuthal correlations of high p_T charged hadrons for $d + Au$, mid-central $Au + Au$, and central $Au + Au$[31]. The trigger p_T range was 8-15 GeV/c and the associated p_T range increases from top to bottom from 3-4 GeV/c to greater than 6 GeV/c

2.1.3 Collective flow

The equation of state of the hadronic matter created in heavy ion collisions at RHIC can be accessed by analysing the medium's collective behaviour. Some of the most compelling evidence for the creation of a QGP have been revealed from studying the collective behaviour of the medium. The crossing paths of the colliding beams of nuclei lead to a range in the impact parameter, b, calculated at RHIC. Physically, a range in b leads not only to a range in the size of the medium created but also in the eccentricity of the overlap region of the colliding nuclei.

The eccentricity of the collision creates differing pressure gradients parallel and perpendicular to the reaction plane resulting in an asymmetry in the transverse flow of the medium [32]. Figure 2.5 depicts a collision at finite impact parameter and shows how the nuclei overlap region creates an anisotropy of pressure parallel and perpendicular to the reaction plane (the plane between the two centres of mass). The anisotropy produces larger pressure gradients in the reaction plane, which boosts the medium expansion parallel to the reaction plane. This boosting of the medium has been observed as a $Cos2\phi$ modulation of the azimuthal distribution of hadrons. It has been argued that the anisotropic transverse flow or elliptic flow, observed in non-central collisions, develops in the early stages of the collision if early thermalisation is achieved indicating an ideal hydrodynamic system [33]. The observation of flow is evidence that the strong coupling constant is finite, hence a strongly coupled QGP. Expansion due to elliptic flow would only persist until the pressure anisotropy had been balanced, which indicates that elliptic flow is only a short lived process. The fact that elliptic flow has been observed indicates that the medium does reach thermalisation early in the collisions evolution. Measuring elliptic flow can provide information about the physics of the early evolution of the collision when the QGP state is expected to form. The elliptic flow represents a background in the two particle correlation structure. The relative size of the back-to-back correlation due to flow is shown by the solid lines in figure 2.3(a).

The hadron distribution in the transverse plane should exhibit a modulation relative to the reaction plane if elliptic flow has developed. The modulation can be measured by the Fourier expansion of the distribution of particles in the transverse plane [35]. The hadron distribution, as a function of rapidity and p_T, has been modified in equation 2.4 to account for this modulation where ϕ

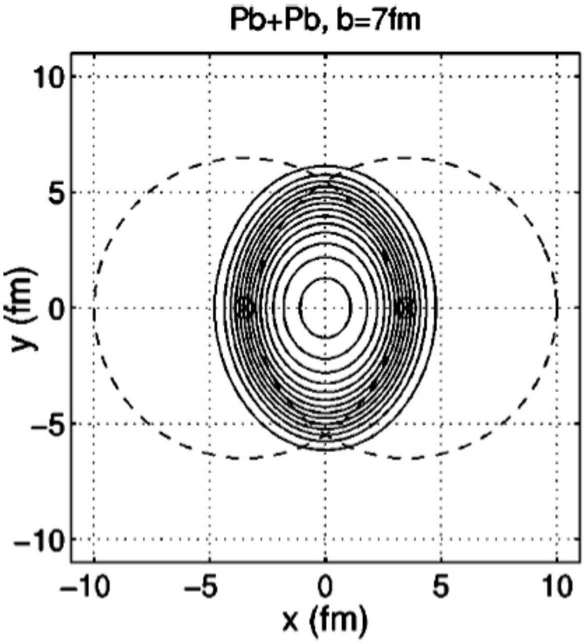

Figure 2.5: A cross section of a peripheral heavy ion collision showing the anisotropy of pressure gradients with respect to the reaction plane [34]. The contours show lines of equal energy density.

describes the azimuthal angle relative to the reaction plane, v_2 is the amplitude of the modulation, and i indicates the particle species.

$$\frac{dN_i}{p_T dp_T dy d\phi} = \frac{1}{2\pi}\frac{d^2N_i}{p_T dp_T dy}(1+2v_2^i(p_T)cos(2\phi)+...) \tag{2.4}$$

The coefficient of the second order term, v_2, of equation 2.4 is expected to dominate and can be extracted via fits to the transverse distributions of hadrons. The STAR experiment first published results on the v_2 of elliptic flow from charged particle spectra in Au + Au collisions at $\sqrt{s_{NN}}$ = 130 GeV. The study showed how, for near central collisions, the elliptic flow was comparable to ideal hydrodynamic models suggesting that early thermalisation had been achieved. There is also evidence of less complete thermalisation in peripheral collisions where hydrodynamic models over estimate the flow [36].

The v_2 of identified hadrons, in Au + Au collisions at $\sqrt{s_{NN}}$ = 200 GeV, has been studied at RHIC [37, 38]. At $p_T < 2$ GeV/c, figure 2.6(a) reveals that v_2 conforms to the particle mass dependence expected from hydrodynamics where the lighter hadrons exhibit larger v_2. This would imply that the QGP behaves like a perfect fluid with a vanishing mean free path and a short time kinetic freeze-out. Above this limit, the v_2 of hadrons no longer scales with mass but appears to split into separate baryon and meson trends. The splitting of baryon and meson trends can be explained by plotting v_2 against p_T where both values have been scaled by the number of constituent quarks [37]. Figure 2.6(b) shows how the v_2 and p_T of hadrons scales with the number of constituent quarks. This constituent quark scaling suggests that elliptic flow develops before the hadronisation of a deconfined medium. In addition, hadrons that exhibit v_2 must therefore be created via the hadronisation of partons that experience anisotropic flow. The controversial aspect of v_2/n scaling is that partons must be constituent quarks with masses equal to those found within hadrons. Furthermore v_2/n scaling can be interpreted as a signature of hadron formation via coalescence.

2.1.4 Quark coalescence

Constituent quarks scaling suggests that hadronisation occurs via quark coalescence. This is supported by the observed baryon enhancement at intermediate p_T in central $Au + Au$ relative to $d + Au$ [39]. The hadron spectra is expected to be dominated by pions for all p_T. Figure 2.7 indicates that the p/π ratio in central $Au + Au$ is greater than unity at p_T between 2-3 GeV/c and is greater than the p/π ratio determined in periperal $Au + Au$ and $d + Au$ in the range 1-6 GeV/c. The lack of an enhancement at high p_T suggests that quark scaling does have a limited reach and above 6 GeV/c fragmentation production mechanisms are expected to dominate. Incidentally, the p/π ratio for the three system sizes all agree within errors above 6 GeV/c.

Hadronisation via quark recombination or coalescence was initially introduced to explain the v_2 enhancement observed for baryons in Au +Au collisions [40]. At a similar time, quark coalescence was introduced as the mechanism responsible for the proton enhancement, described in section 2.1.3, witnessed at intermediate p_T [41]. In the coalescence picture, free quarks in a densely populated phase space can combine to form baryons and mesons. The coalescence mechanism is expected to dominate over the fragmentation mechanism up to $p_T \sim 5$ GeV/c as coalescence is limited by a steeply falling p_T distribution. This is due to fragmentation requiring a much higher initial momentum p, to produce a pion of momentum p_π, where $p = p_\pi/z$. While coalescence

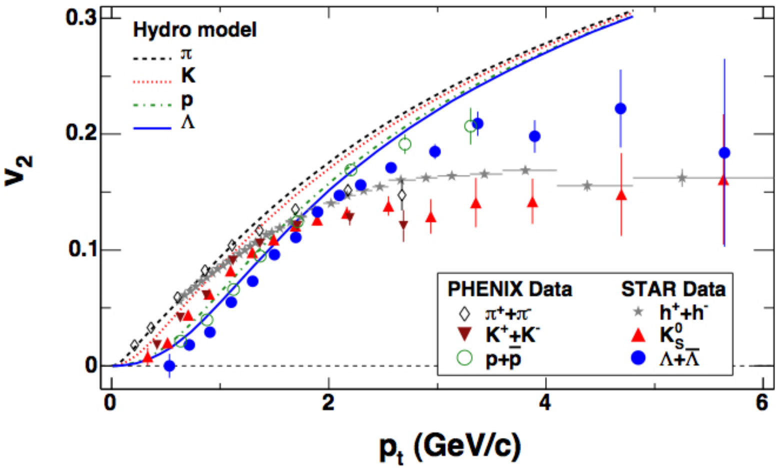

(a)

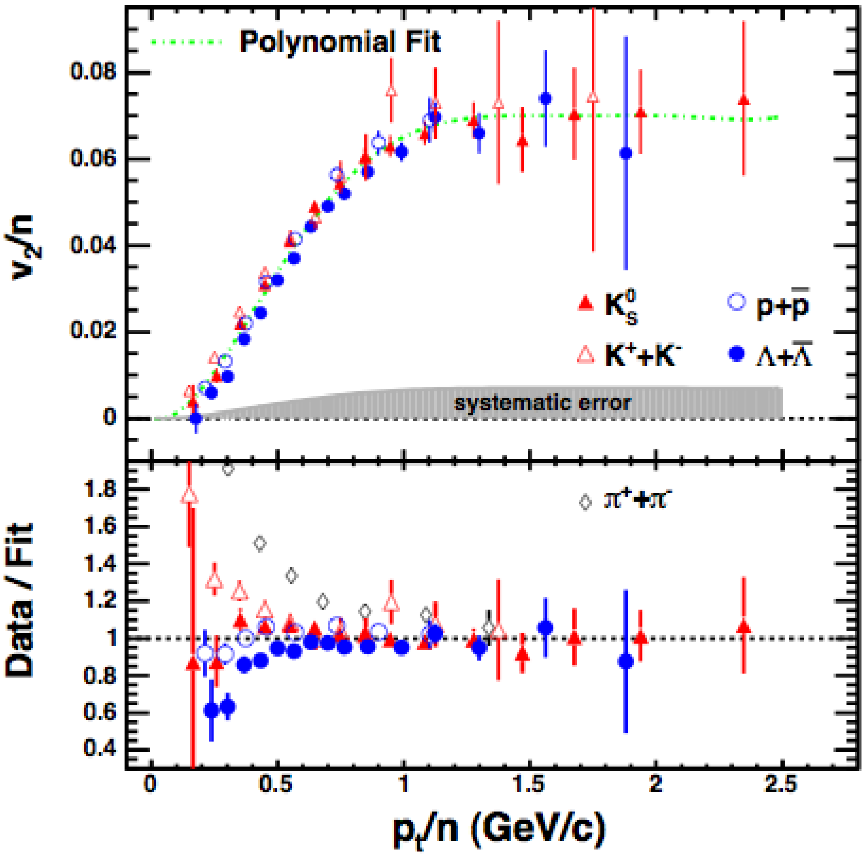

(b)

Figure 2.6: Figure (a) shows v_2 as a function of p_T for different hadron species. Figure (b) reveals that v_2/n as a function of p_T/n for identified hadron species explains the observed v_2 split of baryons and mesons as all hadrons fall upon a single fit function [37].

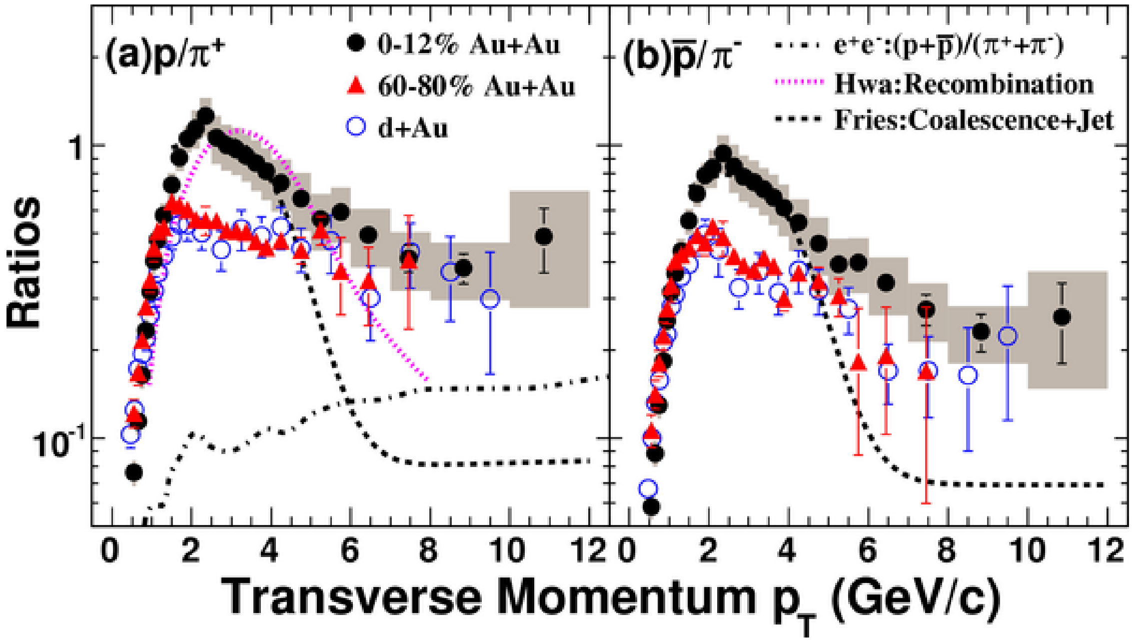

Figure 2.7: The p/π^+ and $\bar{p}/\pi^-$ ratios from d+Au and Au+Au collisions at $\sqrt{s_{NN}}$ = 200 GeV [39].

requires only that the the valence quarks carry $\sim p_\pi/2$ or for baryons $\sim p_B/3$ of the total hadron momentum.

The coalescence models, such as the one described in [41], are not sensitive to the actual recombination process but rely upon the probability of forming hadrons from a single parton distribution of quarks and anti-quarks. The resulting baryon to meson ratio is independent of the hadron momentum and can be calculated by considering the ratio of the number of quark degrees of freedom contributing to each specific hadron such as colour, flavour and helicity. The result for the proton to pion ratio is shown in equation 2.5 where $\frac{C_p}{C_{\pi^+}}$ is the ratio of the summations of the quark degrees of freedom for protons and pions.

$$dN_p/dN_{\pi^+} = e^{\mu_B/T}\frac{C_p}{C_{\pi^+}} = \frac{5}{3}e^{\mu_B/T} \tag{2.5}$$

Charged hadron spectra taken from $Au + Au$ collisions with $\sqrt{s_{NN}}$ = 200 GeV at RHIC have been fit with a function that combines coalescence and high p_T suppressed fragmentation [42]. The resulting function, shown in figure 2.8, shows how recombination and fragmentation dominate at different scales of p_T. In addition the predicted p/π^+ ratio is shown below the spectra fit, which

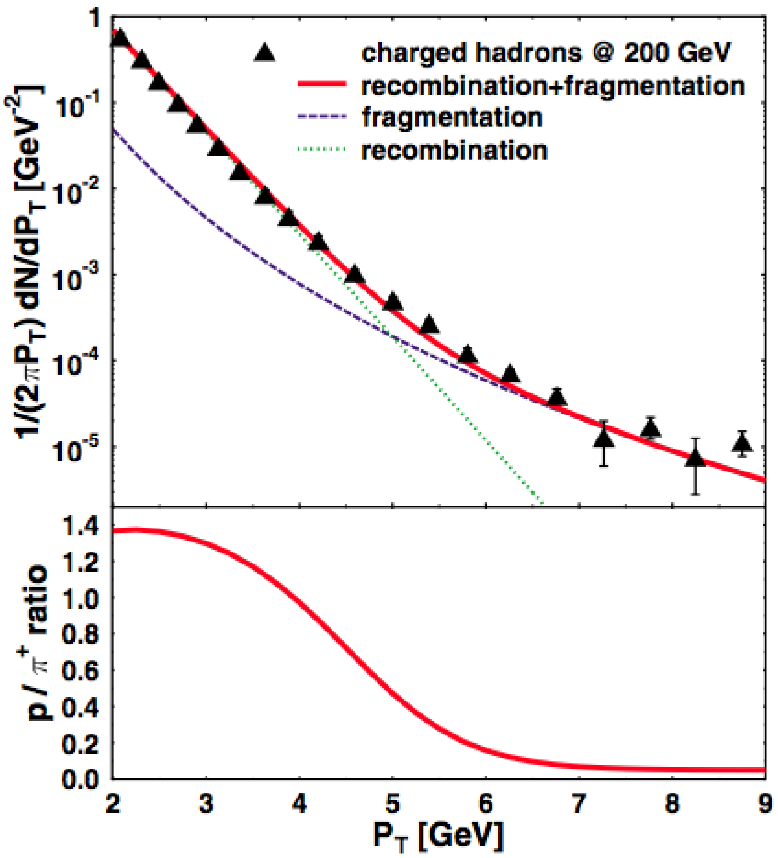

Figure 2.8: A fit to the inclusive p_T spectrum of charged hadrons in central $Au + Au$ collisions at $\sqrt{s_{NN}} = 200$ GeV using a combined recombination and fragmentation function. Below the resulting p/π^+ ratio taken from the fit function [42]. This below curve can be seen as a dashed black line compared to the STAR data in figure 2.7

can be seen in figure 2.7 to accurately describe the RHIC data between 2-4.5 GeV but fails to follow the ratio out to higher p_T. This can be regarded as a reasonable success for coalescence, however the data suggests that a purely fragmentation interpretation does not describe the p/π^+ ratio at p_T greater than 5 GeV/c.

The recombination model has been used to compare the R_{CP} (ratio of central to peripheral collisions) results for identified spectra of neutral strange hadrons (Λ and K^0_S) as well as neutral pions and protons [43]. The model shows reasonable agreement with the data, yet the statistics available were insufficient to extend the fits beyond $p_T = 6$ GeV/c. What the model predicts is that the R_{CP} would simply follow the suppression factor, used for estimating the suppressed fragmentation function, and all hadronic species would lie on the same curve. Although there is a suggestion that the Λ and K^0_S curves join around $p_T = 5$ GeV/c there remains the fact that there are simply insufficient data points to confirm that these hadrons are created from a purely fragmentation mechanism.

The recombination model presented by Hwa, depicted as a pink dashed line in figure 2.7, combines the partons produced by fragmentation with the partons created in the underlying event in a method where all partons hadronise by recombination [44]. This model does not fit as well to the p_T range below 5 GeV/c as the model in [42] but is closer to the data above 5 GeV/c. As the Hwa recombination model is closer to the data, it suggests that there may well be partons from fragmentation coalescing with thermal partons to some degree at RHIC.

Chapter 3

THEORY

In this chapter, the theory regarding the process of jet production will be reviewed from the initial cross section for hard scattering to hadronisation via fragmentation. The current theoretical approaches that are being developed to describe the nature of the suppression in heavy ion collisions will also be reviewed. Proposed jet modification signatures that could be discovered in the jet spectra will be discussed.

3.1 Hard Scattering

A hard scattering event is an elastic collision between two partons where a large Q^2 is transferred allowing for a perturbative calculation of the cross section in QCD.

The cross section for hard scattered hadron production can be calculated using a factorisation theorem, which is a convolution of three components. The Parton Distribution Function (PDF), describing the initial state conditions of the colliding bodies, a pQCD hard scattering cross section and a fragmentation function, which provide the probability of a given parton fragmenting into a specific hadron. Equation 3.1 illustrates a generic cross section for the production of a given hadron, h, per unit of pseudorapidity, η, and p_T. In the PDF i is the incident parton, either q,$\bar{q}$ or

g and $ab \to cd$ can be any of the possible hard scattering processes $qq \to qq$, $qg \to qg$, $gg \to gg$.

$$\frac{d\sigma_h}{d\eta dp_T^2} = \sum_{abcd} \int dx_a dx_b dz \, PDF(i,x_a) PDF(i,x_b) \otimes \frac{d\sigma}{d\hat{t}}(ab \to cd) \otimes D(h,z_c) D(h,z_d) \tag{3.1}$$

3.1.1 Parton distribution functions

Before calculating the cross section for hard scattering events, it is necessary to predict the distribution of momentum amongst the partons within the colliding bodies. The internal structure of hadrons cannot be described using pQCD as the structure is determined by the long range component of the strong interaction. Deep inelastic scattering experiments have not only revealed that protons are a multi-parton entity of gluons and quarks, they have also shown that the proton PDF is a function of x and Q^2. The structure of the proton has been studied for $10^{-4} < x < 0.65$ and $1 \lesssim Q^2 \lesssim 30000$ GeV^2 using $e+p$ collisions at HERA [45].

The PDFs were determined for positive and negative (anti)quark species and gluons at fixed values of Q^2. Figure 3.1 reveals how the momentum distribution of partons in a proton depends upon the parton species. The model fits are in good agreement with experimental data and demonstrates that the proton PDF is dominated by gluons. However in the high x region ($x > 0.3$) valence quarks dominate the PDF. The probability of hard scattering events can be calculated by integrating over all possible initial states, provided by the PDF, and the hard scattering cross section [46].

Due to the vast majority of partons being low x ($x < 0.01$) gluons, $qg \to qg$ scattering can be seen to dominate the jet cross section in figure 3.2(a). At higher jet p_T, high x partons are the only suitable candidates for jet production if the centre of mass energy remains constant. The jet cross section at $p_T > 40$ GeV/c is therefore dominated by valence quark scattering. Yet figure 3.2(b) shows that the hard scattering cross section of jets with $p_T > 40$ GeV/c at RHIC energy is orders of magnitude smaller than the jet events at $p_T < 20$ GeV/c. Therefore the jet production cross section at RHIC is dominated by gg and qg scattering.

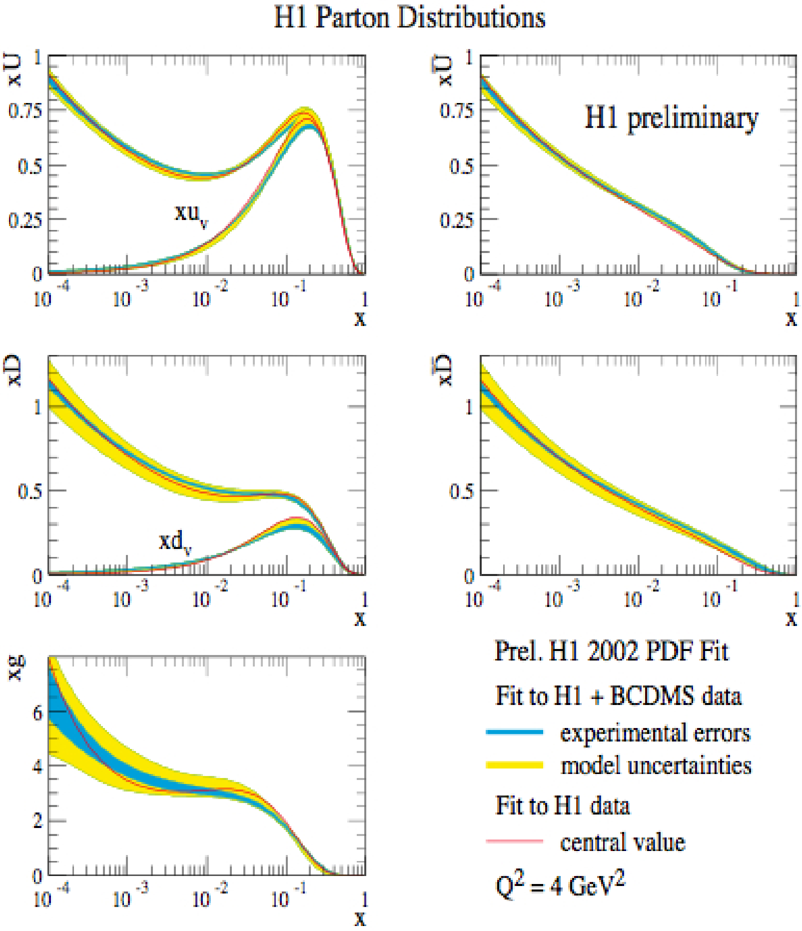

Figure 3.1: Proton PDFs xU = x(u + c), x$\bar{U}$ = x($\bar{u}$ + $\bar{c}$), xD = x(d + s), x$\bar{D}$ = x($\bar{d}$ + $\bar{s}$) and xg as determined from the H1 fits at the starting scale Q^2 = 4 GeV^2 [45]. Valence quarks are shown to dominate in the high x region while gluons dominate the remaining distribution

3.1.2 Fragmentation functions

Fragmentation functions, denoted as $D(h,z)$, can be used to represent the probability of a given parton fragmenting into a specific hadron, h, where the hadron carries a certain fraction of the parton's energy, z. Fragmentation functions represent the final state after a hard scattering event whereas PDFs represent the initial state before the event. In high energy collisions the energy of the scattered parton can be established by reconstructing the jet to which the parton fragmented by summing the energy of each hadron within the jet. Experimentally, e^+e^- experiments allow for a simple method of identifying the energy of the hard scattered parton as the two quarks are produced with equal and opposite momenta, $\pm\sqrt{s}/2$. In hadron collisions the hard scattering is only a sub event of the entire collision as soft scattering also occurs between the remaining partons

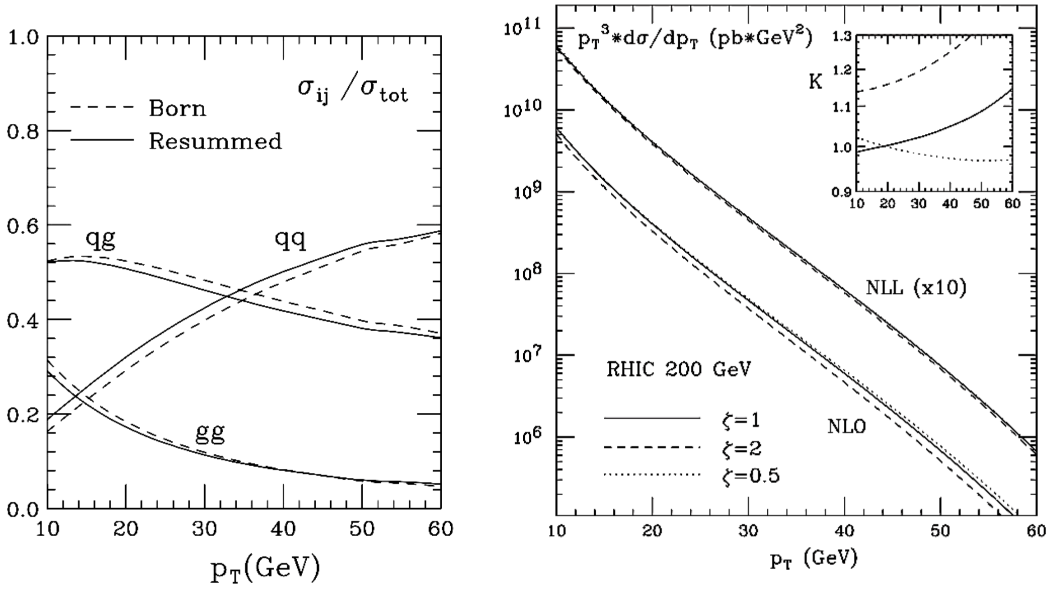

(a) (b)

Figure 3.2: Results from pQCD calculations for the jet cross section at RHIC energy in $p + p$ events. Figure (a) shows the relative contributions of the various partonic initial states to the single-inclusive jet cross section. Figure (b) shows NLO and NLL results for the single-inclusive jet cross section [46].

taking part in the collision.

As fragmentation functions are part of a factorisation theorem, they are independent of any initial state effects and are only determined by the flavour of the parton and Q^2. The fragmentation of any given parton should therefore be independent of the colliding body allowing for e^+e^- data to be used to measure the fragmentation functions that may be applied to hadron-hadron collisions [47]. A study of jet fragmentation by the UA1 collaboration at CERN compared the fragmentation functions from $p\bar{p}$ collisions to those from e^+e^- collisions for similar jet energies. The conclusion was that the observed fragmentation function into charged hadrons in $p\bar{p}$ collisions is indeed very similar to that seen in e^+e^- jets [48].

The inclusive fragmentation functions for light and heavy charged hadrons were studied by ALEPH at LEP and SLD at SLAC [6, 49]. The inclusive particle spectra from e^+e^- collisions at LEP is shown in figure 3.3. The inclusive spectra has also been separated into quark flavour categories, where the quark flavour corresponds to the initial pair of particles created from the decay of Z^0 bosons. Figure 3.3 revels that experimental results can be used to constrain next-to-leading order

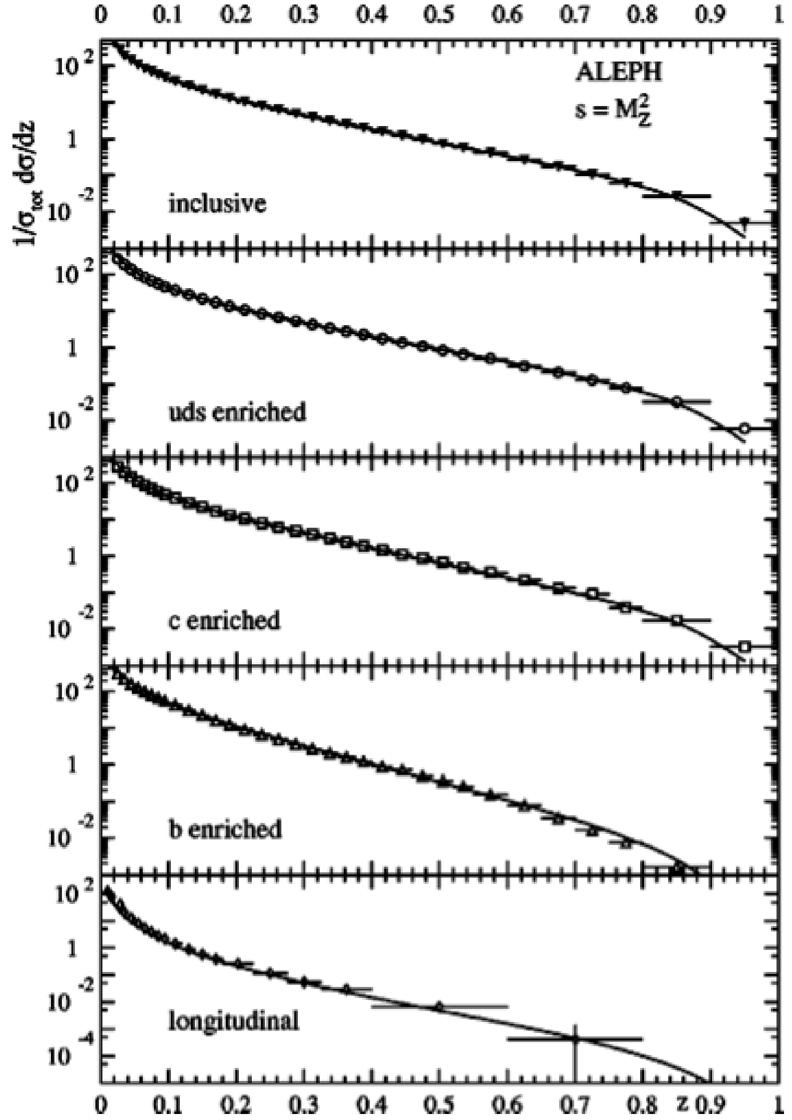

Figure 3.3: ALEPH inclusive particle spectra, measured at the Z^0 pole from e^+e^- annihilation [50]. The particle spectra has been split into hadrons rich in *b*, *c* and *uds* quarks.

QCD fragmentation functions by using the function to fit the data. An observation from figure 3.3 is that there is a steep curve dependence with z, where z is $2E_{hadron}/\sqrt{s}$, implying that the vast majority of jet fragments are soft low momentum particles.

Evidence for a single particle carrying the majority of the jet energy was found at the CERN ISR and can be seen in figure 3.4. The z dependence of hadrons, where z is now referring to the fraction of the momentum carried by a hadron with respect to the highest momentum hadron in the jet, is shown to also have a steep curve dependence like the inclusive spectra. Further studies at FERMILAB have supported the leading particle observation and found that the leading

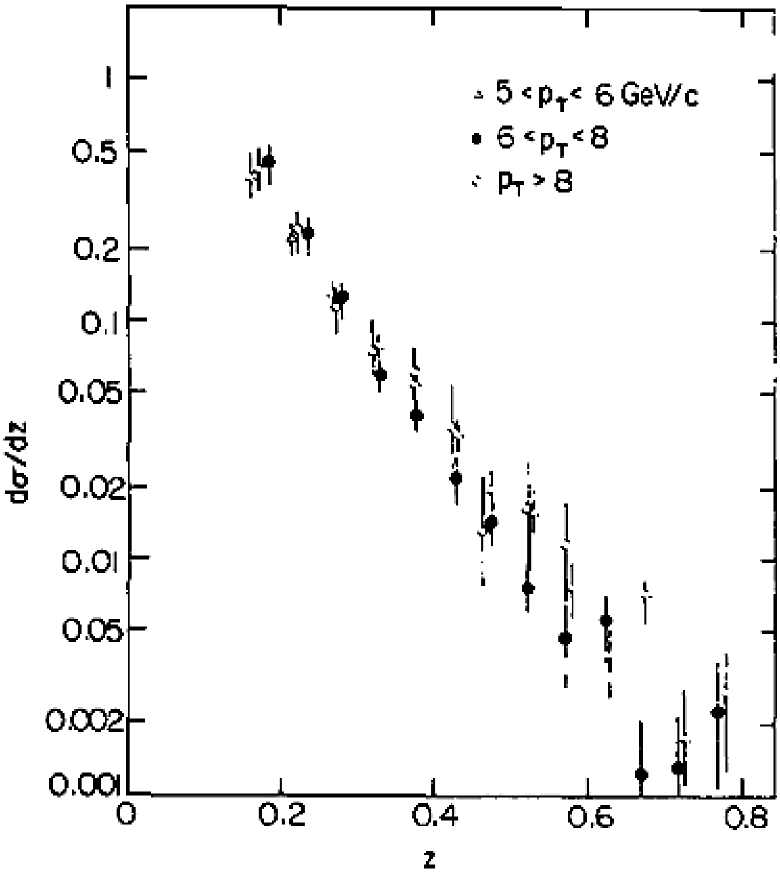

Figure 3.4: Fraction of trigger momentum z taken by charged secondary hadrons from $p + p$ collisions at CERN ISR [52]. The three data sets reference different trigger particle p_T acceptance.

particle carried up to 90% of the total jet momentum in $p + A$ collisions [51]. The significance of the leading particle observation to the current analysis is that it motivates using the two particle correlation method, which relies exclusively on a single high p_T trigger, for jet finding.

3.2 Fragmentation

Once the hard scattering has taken place the scattered partons will fragment into further partons and finally hadronise to form colour neutral hadrons. There are currently three leading theories regarding hadronisation, the string model [53], the independent fragmentation model [54] and the cluster model [55], which has been subject to recent modification [56].

The string model uses gluons as field lines, utilising the self-interaction of gluons to justify compressing gluons into narrow colour rich strings that propagate between quarks. The independent fragmentation model treats the collided partons independently and uses a quadratic fragmentation function to determine the relative momentum of a given hadron to that of the parent parton. The cluster model creates a parton shower of gluons. Once all the gluons have been created, they are converted to quark-antiquark pairs that are then clustered into groups of pairs that decay into hadrons. The string model will be discussed in the following section as this theory forms the basic particle production principles that are used by the Monte Carlo event generator package *Pythia* that shall be used to simulate $p + p$ events for this thesis.

All three theories have been tested with experimental data with varying success [57]. The model predictions were compared with the results from the Positron-Electron Project (PEP) at $\sqrt{s} = 29$ GeV. The string model provided a good description of the data while the independent fragmentation model did not. The cluster model was untuned for the test at PEP but has been shown to satisfactorily agree with hadron spectra taken from $p\bar{p}$ collisions at $\sqrt{s} = 200$-1800 GeV [58].

Jet fragmentation has been thoroughly examined using $e^{+}e^{-}$ colliders yet there remains uncertainties when applied to hadron-hadron collisions. The main cause for theoretical concern is that the events produced in hadron-hadron collisions are governed largely by non-pertabative soft processes. Modeling the final state hadron spectra has therefore been notoriously challenging and requires extensive tuning of the Monte Carlo event generator parameters [59].

3.2.1 Lund string model

There are several string models being used to describe fragmentation, yet they are all based on a common starting point. A typical demonstration of the string model is to consider the space-time evolution of a $q\bar{q}$ pair created from the annihilation of $e^{+}e^{-}$. As the pair of quarks separate, the colour field between them collapses due to the self interaction of the gluons. The collapsed colour field can be described as a flux tube of uniform energy density per unit length leading to a linearly dependent potential experienced by one quark due to the other. Experimental evidence has shown that the diverging quarks fragment into jets and not just two separate hadrons. The dynamics of

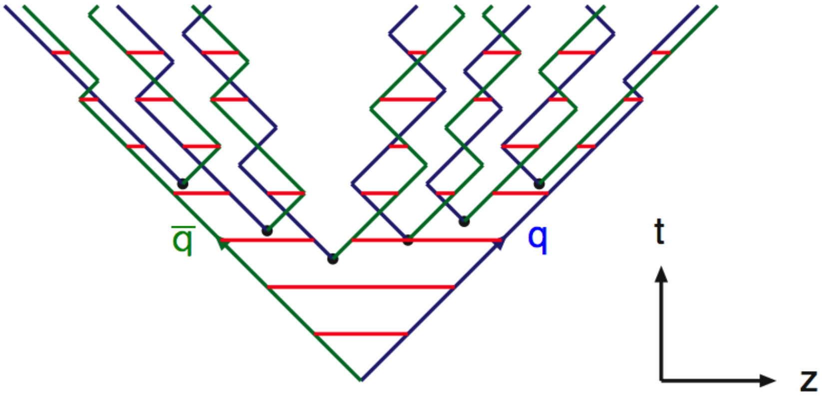

Figure 3.5: Space-time evolution of a string fragmenting into hadrons [2]. Hadronisation commences at the centre of the string where lower momentum hadrons are produced

the flux tube can be described using a massless one dimensional string with negligible transverse excitation [2].

The rupture of the string produces a shock wave that causes the massless string end points (quarks) to oscillate about the rest frame of the string in what are described as yo-yo modes. These yo-yo modes can be seen in figure 3.5 where the position of the quark anti-quark pairs that form the new mesons, which have been created following string fractures, oscillate within their respective meson boundary. Consequently the energy of the whole system fluctuates from the string to the quarks in yo-yo modes [60]. The Lund string model describes a continuous fragmentation process where the scattered quarks fragment over a period of time. The string model has been shown to accurately describe three-jet events indicating that continuous fragmentation is occurring in the vacuum and not a single fragmentation event where all the hadrons are created simultaneously [61]. The scenario of continuous fragmentation is important when searching for jet modification in heavy ion collisions as this conclusion permits the possibility that the fragments of the hard scattered parton may also interact with the medium.

3.2.2 Baryon production

The structure of the valence quarks in baryons is described using a Y shaped string, which would appear reasonable when utilising the collapsing colour field idea, with each end point correspond-

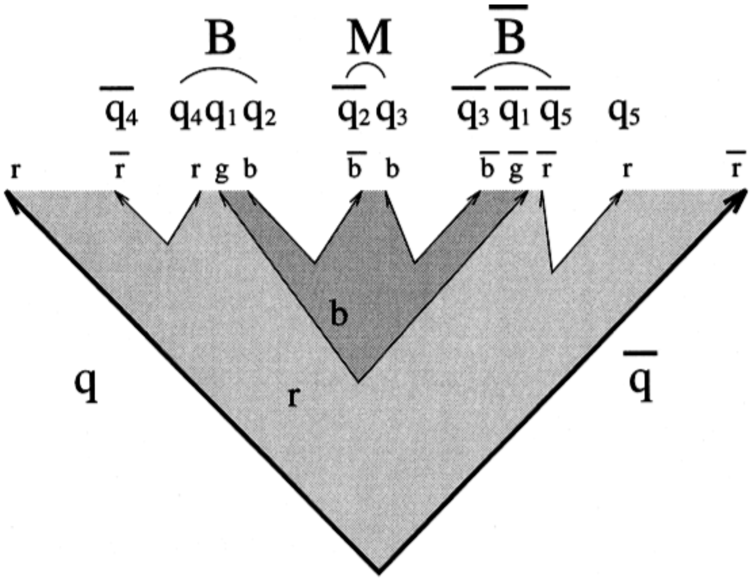

Figure 3.6: BMB configuration in the string-framentation model [66]

ing to a quark. The junction at the centre of the string is considered as the carrier of the baryonic number [62]. The fragmentation mechanism that leads to baryon production is not as simple as the meson description as baryons must be produced in pairs. Not only must they be produced in pairs they cannot contain a mix of quarks and anti-quarks. This essentially gives rise to baryon number conservation as baryons must be formed as baryon anti-baryon pairs.

The most recognized baryon production mechanism from fragmentation is the Baryon, Meson anti-Baryon popcorn model that stemmed from the original Lund string theory [63]. Figure 3.6 illustrates how a meson is sandwiched by a baryon-anti-baryon pair in the popcorn model. This method of producing baryons has been successfully matched to data from the PEP4-TPC collaboration, the OPAL collaboration at LEP and the TOPAZ collaboration at TRISTAN all of which observed the BMB ordering by comparing the angular distribution of $p\bar{p}$ pairs with string model predictions [64, 65, 66].

3.3 Jets in Heavy Ion Collisions

The initial state is different in heavy ion collision than that found in hadron-hadron collisions. By using an appropriate nuclear PDF, the particle spectra from heavy ion collision could be modeled using the same fragmentation function, assuming that factorisation holds. Any deviation from the model using the nuclear PDF would be attributed to a modified fragmentation function.

Establishing the initial conditions is an important step in understanding and predicting the outcome of any given heavy ion collision. There have been experiments, such as the fixed target experiments at FERMILAB, that have studied the nuclear PDF of cold nuclear matter using electron-nucleus collisions and proton-nucleus collisions [67]. However the nuclear PDF of gluons has proved difficult to constrain as the low x region, where gluons dominate the nuclear PDF, has not been probed by experiment.

There has been suggestions that there could be significant differences between the PDF of nucleon matter and that of nuclear matter when accelerated to high energy. This is due to the strong growth in gluon density at low x, which is dependent on the number of nucleons. As a result, parton saturation has been the focus of intense study in recent years in an attempt to understand bulk properties in heavy ion collisions such as the N_{part} scaling of inclusive hadrons at intermediate to high p_T [68].

The latest EPS09 NLO model developed to describe the nuclear PDF uses inclusive pion data measured at RHIC as the pion spectra at intermediate p_T has been found to be sensitive to the gluon distributions [69]. Figure 3.7(a) shows the predicted nuclear modifications, R_i^{Pb}, where R is the ratio of the PDF per nucleon in a nucleus to the PDF per nucleon of deuterium, to the PDF for lead nuclei from the EPS09 NLO model that has been constrained by experimental data. The nuclear PDF taken from these fits shows good agreement with h^- production in $d+Au$ at high rapidity where the greater suppression of negative hadrons than positive hadrons has been said to be a sign of saturation effects [70].

At low Q^2 there appears to be a strong suggestion of both nuclear anti-shadowing at intermediate x and nuclear shadowing at low x resulting in the multiple scattering of the incident parton. The anti-shadowing effect is almost exclusively produced from gluon scattering. However there are large uncertainties attributed to these predictions where little or no experimental data is available. Figure 3.7(a) also shows how the nuclear modification to the PDF is Q^2 dependent. At high Q^2, only a slight modification is predicted to nuclear PDF.

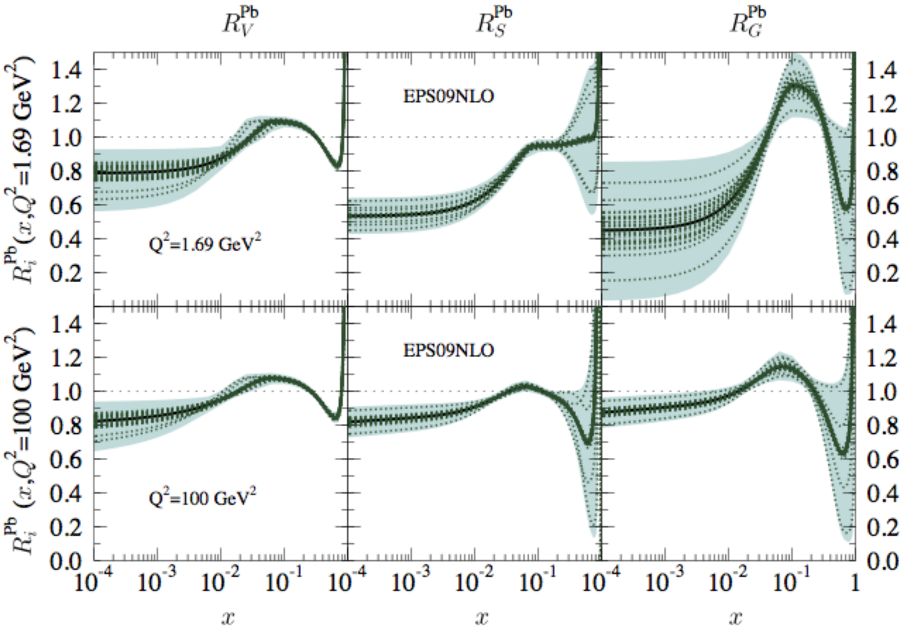

(a)

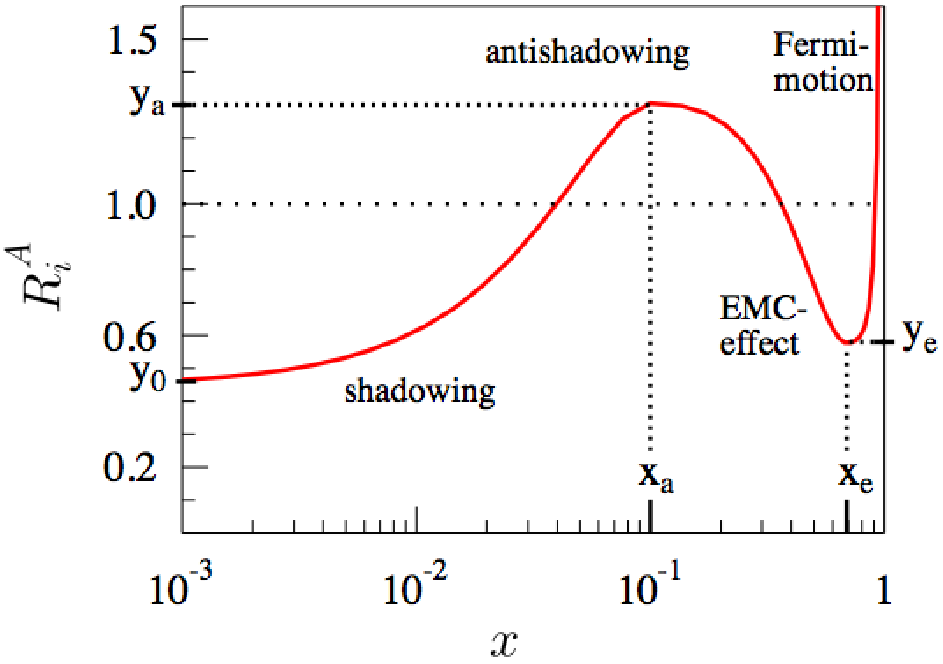

(b)

Figure 3.7: The nuclear modifications $R_{valence}$, R_{sea} and R_{gluon} for low and high Q^2 values are shown in figure (a).. The high x and low x gluon regions show large uncertainties due to lack of experimental data. The physical consequences of the nuclear modification factor at different scales of x are shown in figure (b). The five labels correspond to the parameters used in the fit [67].

3.4 Modelling jet modification

This chapter has so far discussed the creation of jets and how there is evidence to suggest that the incidence of hard scattering in heavy ion collisions should scale with the number of binary collisions. Experimentally this is not the case in $A + A$ collisions, which has already been alluded to in section 2.1. The experimental observations indicate that final state interactions are the cause of the high p_T suppression yet it is non-trivial to decipher what actually constitutes the final state. There have been several attempts to describe the high p_T attenuation observed at RHIC. They can be broadly summarised into two distinguishable categories where either the attenuation is modeled via the multiple radiation of soft gluons or via scattering producing few hard gluons. In the following parts of this section, an example of each category shall be reviewed followed by a summary contrasting the strengths and weaknesses of each approach.

The original work on suppression by Wang, Gyulassy and Plümer incorporates the Landau-Pomeranchuk-Migdal effect into a QCD framework and calculates the resulting elastic and radiative components to the energy loss per unit length, $-dE/dz$ [71]. The calculated radiative energy loss is very sensitive to the colour screening scale which itself is sensitive to temperature. The calculation also predicts that only $\sim 25\%$ of the total energy loss is due to elastic collisions and that the contribution from elastic collisions decreases as a function of parton energy. However, the derivation was performed under the assumption of a weakly interacting QGP where α_s could be treated perturbatively and the interaction range is small compared to the mean free path. A shorter mean free path and larger α_s could possibly favour elastic scattering as the Landau-Pomeranchuk-Migdal effect is enhanced when the mean free path is smaller than or comparable to the radiative gluon formation time.

3.4.1 BDMPS approach to high p_T attenuation

An example of a soft gluon radiation theory is the BDMPS formalisation, named after the authors, Baier, Dokshitzer, Mueller, Peigné and Schiff [72]. Modeling the radiative energy loss of a particle traversing matter has been studied in QED and the BDMPS formalisation is a modification of the theory used to describe the QED case. In the QCD case a $\alpha_s\sqrt{E}$ dependence was calculated for $-dE/dz$ and the total energy loss, ΔE, was found to be proportional to the square of the medium size, L^2. The BDMPS result predicts large attenuation, a result that was initially surprising until the discover of such an attenuation at RHIC. The energy loss mechanism, developed in the parton quenching model by BDMPS, requires the computation of a transport coefficient $\hat{q}$, where the scale of the energy loss is set by the characteristic energy of the radiated gluons, ω_c, shown in equation 3.2 where k_T is the transverse momentum with respect to the parton direction and λ is the mean free path of the energetic parton [73]. In short $\hat{q}$ is related to the density of the medium.

$$\begin{aligned}\omega_c &= \hat{q}L^2/2 \\ \hat{q} &= \langle k_T^2\rangle/\lambda\end{aligned} \tag{3.2}$$

Figure 3.8 shows how $\hat{q}$ can vary by making small adjustments to the simulation parameters. The use of a Glauber model to compute the path length in figure 3.8(b) is more sophisticated than assuming a fixed average path length of 6 fm, which was the case in figure 3.8(a). In Figure 3.8(b) a shaded area is shown as the result for a fixed $\hat{q}$ = 15 Gev^2/fm. The upper limit to the shaded area is where the calculation of energy loss is performed when ΔE is less than E and the lower limit is where if ΔE is greater than E, ΔE is set to E.

Although $\hat{q}$ = 15 Gev^2/fm is an order of magnitude higher when using a Glauber model to compute the path length instead of using a static medium it does not suggest that $\hat{q}$ is arbitrary. Increasing the density of the system does not linearly increase the suppression thus limiting the accuracy to which the high p_T spectra can determine $\hat{q}$ to a range of 5-15 Gev^2/fm [74].

The BDMPS model does show good agreement with the R_{AA} extracted from RHIC data not only with central events but at all centralities. One slight limiting factor is the model can only be used where fragmentation dominates the hadron spectra as initial state effects (i.e Cronin effect) and in-medium hadronisation are expected to play a major role in hadron production at low p_T.

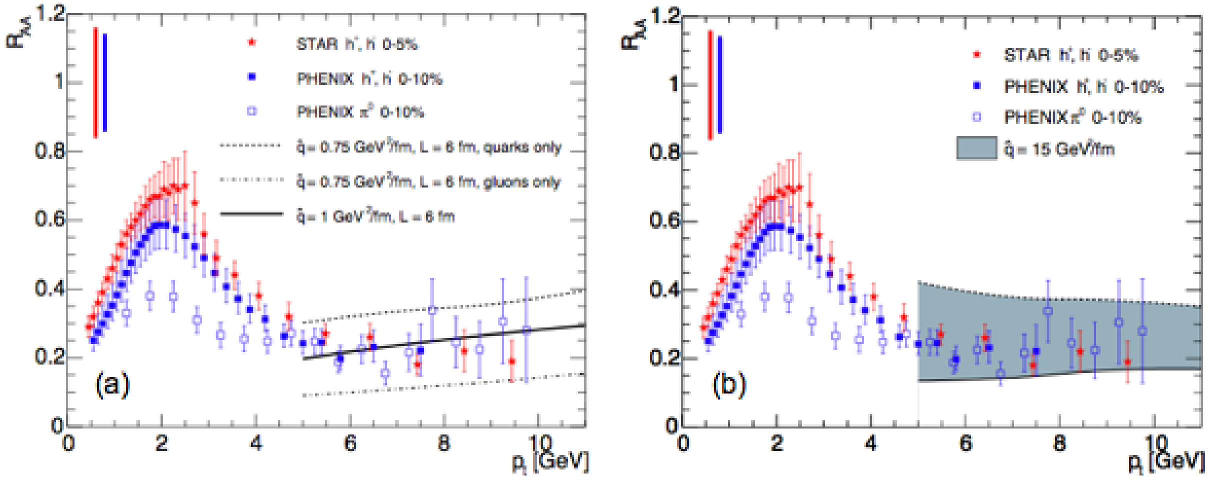

Figure 3.8: BDMPS model R_{AA} predictions using different $\hat{q}$ values compared to the observed R_{AA} for hadons observed at RHIC in central $Au + Au$ collisions [73]. Figure (a) uses a static path length, while the figure (b) uses a Glauber model to describe the geometry of the collision and subsequent path lengths.

3.4.2 GLV approach to high p_T attenuation

An alternative approach to high p_T suppression is to consider energy loss via a few hard gluon emissions. One such approach is the Gyulassy-Levai-Vitev (GLV) model where the key parameter is the opacity of the medium, χ, which is proportional to the medium density, ρ, where $\chi = \sigma\rho L$, σ is the hard scattering cross section and L is the path length [75].

In Figure 3.9, the GLV model for a static medium has been compared to the neutral pion spectra in $Au + Au$ collisions at $\sqrt{s_{NN}}$ = 130 GeV [76]. The pion spectra is most accurately described by an opacity between 3-4, which suggest that the mean number of collisions is also 3-4.

The ratio of the central to peripheral pion yields normalised by the number of binary collisions, denoted in figure 3.10 as R, can be used as a consistency check to see whether it too agrees with an opacity between 3-4. Figure 3.10 shows that R does agree with the previous finding in figure 3.9 where the opacity is between 3-4. It is important to note that static opacities do not account for the rapid expansion and thus dilution of the medium after the collision.

When considering an expanding medium a fixed opacity can not be used. To estimate the medium density, the soft parton rapidity density, dN^g/dy, is related to ΔE in order to account for the system size dependence of high p_T suppression. In the limit of large parton energy, ΔE is proportional

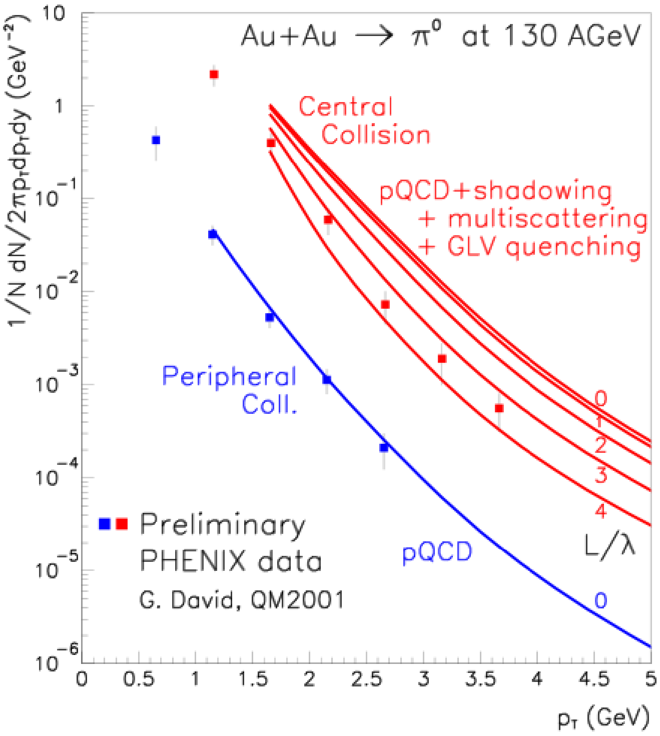

Figure 3.9: π^0 spectra in $Au + Au$ collisions at $\sqrt{s_{NN}}$ = 130 GeV compared to GLV model predictions with different opacity values [76]. The central collisions data most closely matches an opacity that is between 3-4 where λ is the mean free path, while the peripheral data is best fit with an opacity of zero.

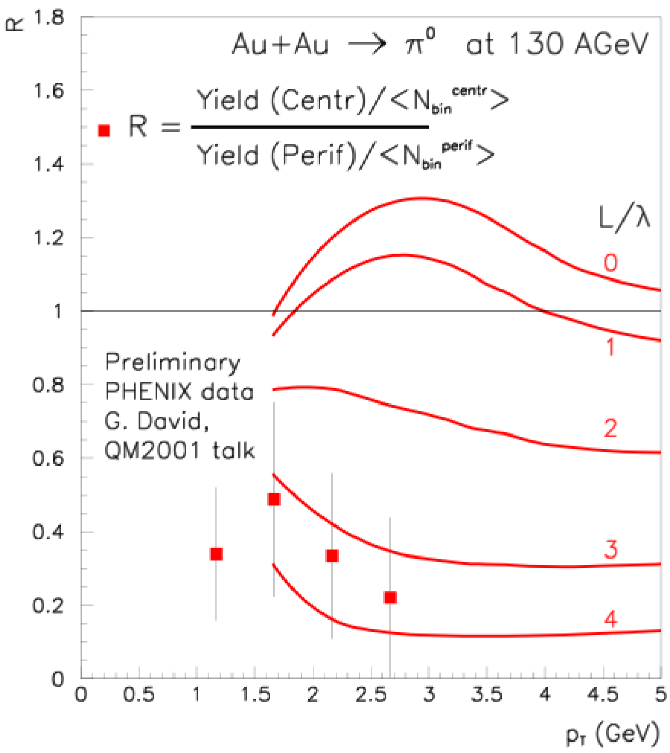

Figure 3.10: Comparison between GLV model and the ratio of the central to peripheral pion yields, R, of π^0 spectra in $Au + Au$ collisions at $\sqrt{s_{NN}} = 130$ GeV [76]. The data most closely matches an opacity that is between 3-4.

to the number of participants, N_{part}, such that $\Delta E/E \propto N_{part}^{2/3}$ [77]. When the GLV prediction is compared with π^0 R, denoted as R_{AA} in figure 3.11, calculated for both $Au + Au$ and $Cu + Cu$, there is found to be reasonable agreement. Within the yellow band in figure 3.11 is where the π^0 data is expected to be found if there is good agreement with the GLV prediction. The upper and lower bounds of the yellow band use a dN^g/dy equal to 800 and 1175 for $Au + Au$ and 255 and 370 for $Cu + Cu$.

3.4.3 Collisional energy loss

An additional approach to high p_T suppression is to consider collisional energy loss and hard gluon emission, which gained renewed interest after the suppression observed in the non-photonic electron R_{AA} (electrons from the decay of B and D mesons) could not be accounted for by radiative energy loss alone [78]. Heavy flavour quarks are expected to experience less suppression from radiative energy loss due to their large mass restricting the phase space for gluon emission known

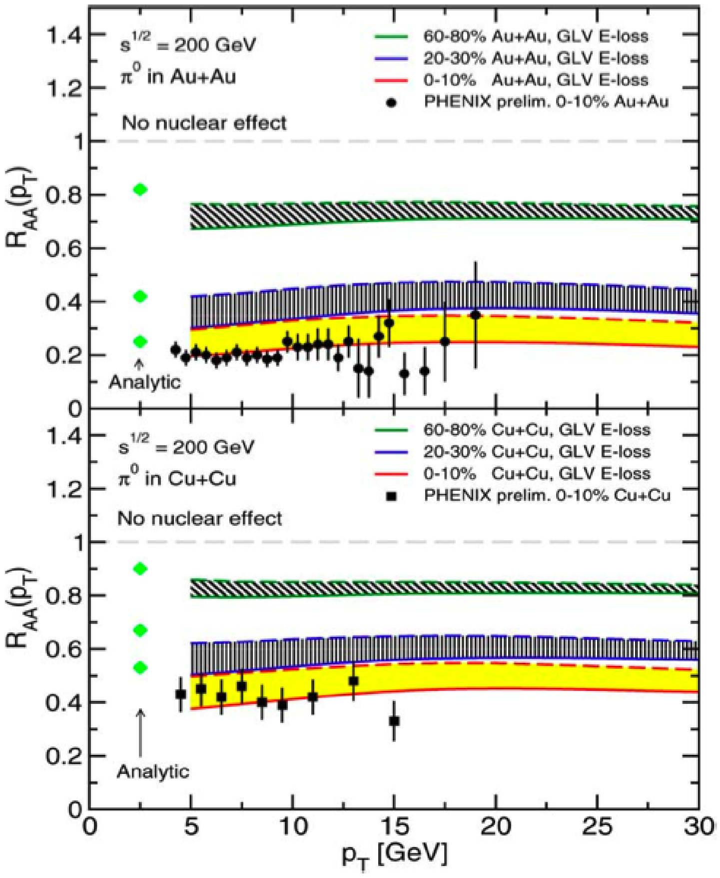

Figure 3.11: Comparison between GLV model and R_{AA} of π^0 spectra in $Au + Au$ and $Cu + Cu$ collisions at $\sqrt{s_{NN}} = 200$ GeV [77]. The R_{AA} of π^0 spectra follows closely the yellow band lower bound of $dN^g/dy = 1175$ in $Au + Au$, while in $Cu + Cu$ the data falls within the yellow band.

as the *dead cone* effect [79].

One such approach uses the Fokker Planck equation to dynamically evolve parton spectra and calculate the R_{AA} for neutral pions [80]. The pion R_{AA} is accurately described by the pure collisional energy loss framework and there is the suggestion that including the three body elastic channels may further increase E_c, the parton energy below which elastic energy loss dominates, above 30 GeV for collisions at $\sqrt{s_{NN}} = 200$ GeV. A comparison study that used both radiative and collisional mechanisms for high p_T suppression concluded that both frameworks can be used to describe the suppression [81]. The main observation is that the two models produce comparable results if comparable sets of model parameters are used. The only significant difference is that the energy of the gluons involved are different with radiative processes dominating when $\omega < \omega_c$ and collisional processes dominate when $\omega > \omega_c$.

There remains significant doubt as to which of the aforementioned energy loss processes is the dominant process in high p_T suppression. Each model can be tuned to describe experimental data therefore it is difficult to suggest which model is more significant. A comparison of four different approaches to high p_T suppression concluded that discrepancies in the transport coefficient, $\hat{q}$, surmount between each method when using the same basic assumptions and approximations [82]. In conclusion, there is no doubt that high p_T particles are suppressed in the presence of the medium created in heavy ion collisions at RHIC. What is not well understood is the energy loss mechanism.

It must be assumed that both radiative and collisional energy loss mechanisms contribute to the overall suppression observed. The important conclusion for this analysis is that both radiative and collisional energy loss mechanisms allow for the transfer of properties, quantum numbers or simply momentum, from and to the medium via partonic interactions that could be seen in the modification of jet hadron spectra. The full scale of these partonic interactions shall be addressed in the remainder of this chapter.

3.4.4 Modified fragmentation

There are two possible scenarios that could describe the high p_T suppression observed in central Au + Au collisions. The first scenario is where the high p_T parton losses energy while traversing the medium and then fragments, in vacuum, creating a lower energy jet that is otherwise unperturbed by the preceding interaction with the medium. The second scenario considers that the energy is not lost to the medium, but the fragmentation process begins within the medium, in addition to further fragmentation in vacuum. The second scenario describes modified fragmentation and this is will be discussed further in this section.

When an energetic parton interacts strongly with a deconfined medium, colour must be exchanged. The interaction alters the colour composition of the partonic shower, which ultimately must affect hadronisation. At the end of the partonic evolution the correct distribution of colour must exist in the pre-hadronic shower for colourless hadron states to form. Overall the interaction would lead to a variation in the distribution of the jet invariant mass due to the additional interaction with the medium. There are possible additional effects of interaction, other than colour exchange, that could be observable in jet spectra such as multiplicity, flavour, baryon number and the possibility of jet fragments hadronising, via recombination, with thermal quarks from the medium. The possible consequences of each affect shall be revisited briefly in turn at the end of this section.

An approach developed by Sapeta and Wiedemann studies modified jet multiplicity by applying an enhanced parton splitting component to a radiative high p_T suppression model to incorporate perturbation by a deconfined medium [83]. They acknowledge that the other previously mentioned affects could also contribute to jet modification and thus they expect that their predicted spectral modification is an underestimate. The model used by Sapeta and Wiedemann uses a modified leading logarithmic approximation (MLLA) [84], supplemented by local parton-hadron duality (LPHD) [85] to calculate the parton distribution, $D_{q,g}(\xi, \tau, \lambda)$ where $\xi = ln(1/x)$, $\tau = ln(Q/\Lambda)$ and $\lambda = ln(Q_0/\Lambda)$, within a jet, where $E_{jet} \sim Q$. In this description, Λ and Q_0 (which is $\approx M_{hadron}$) are both fit parameters that constrain the parton shower evolution to remain above a perturbatively calculable limit in Q^2.

The MLLA+LPHD approach has proved successful at recreating the opening angle dependence of unidentified inclusive charged jet spectra and the momentum distribution of identified inclusive charged jet spectra for in-vacuum fragmentation of jets in $p\bar{p}$ collisions at $\sqrt{s}$ = 1.8 TeV [86]. Unfortunately, as described in section 3.4.1, there is no unique method of describing medium modification of jet fragments. Therefore the assumptions used by Sapeta and Wiedemann do not constitute the only means to calculate medium modification. At the time of publication, the only observable evidence for jet modification is the factor $\sim$ 5 suppression of hadron spectra in central Au + Au collisions. The manipulation of the MLLA+LPHD model, in order to convey medium modification, is very simple and requires only an additional factor $(1 + f_{medium})$, that enhances all the parton splitting functions. The value of f_{medium} can be tuned to recreate the factor $\sim$ 5 suppression observed in RHIC hadron spectra.

The enhancement of parton splitting does lead to an enhancement in heavier hadrons, which can be seen in figure 3.12. A critical consideration is that the jet energies displayed in figure 3.12 are relevant to LHC energies. At RHIC, the jet energy spectrum is a factor $\sim$ 10 lower than those expected at the LHC, which will greatly restrict the accessible p_T range for jet hadrons [87]. Still, the enhancement of heavier hadrons is a consequence of a reshuffling of hadronic yield from high to low p_T, therefore the heavy hadron enhancement could also be seen at RHIC.

The additional mechanisms that could lead to jet modification, which were not included in [83], are considered here to provide a full picture of possible jet modification signatures. Coincidentally, most modification possibilities lead to the same observation, which should make the modification signal larger but severely limit any possibility of discovering the precise cause. Heavier hadrons are enhanced for increased multiplicity jets, but this would also be the case for flavour exchange and recombination with thermal quarks. Flavour exchange could increase heavy hadron yields, by Compton processes such as $q + g \to g + q$ as gluon jets exhibit a significant proton enhancement when compared to quark jets [88]. If the QGP is full of strange quarks, these conversion would lead to strangeness enhancement in addition to baryon enhancement in the jet. Recombination could increase baryon or strangeness yields using similar arguments as the additional (strange)quarks increase the production of (strange)baryons at higher p_T . If recombination does alter jet spectra,

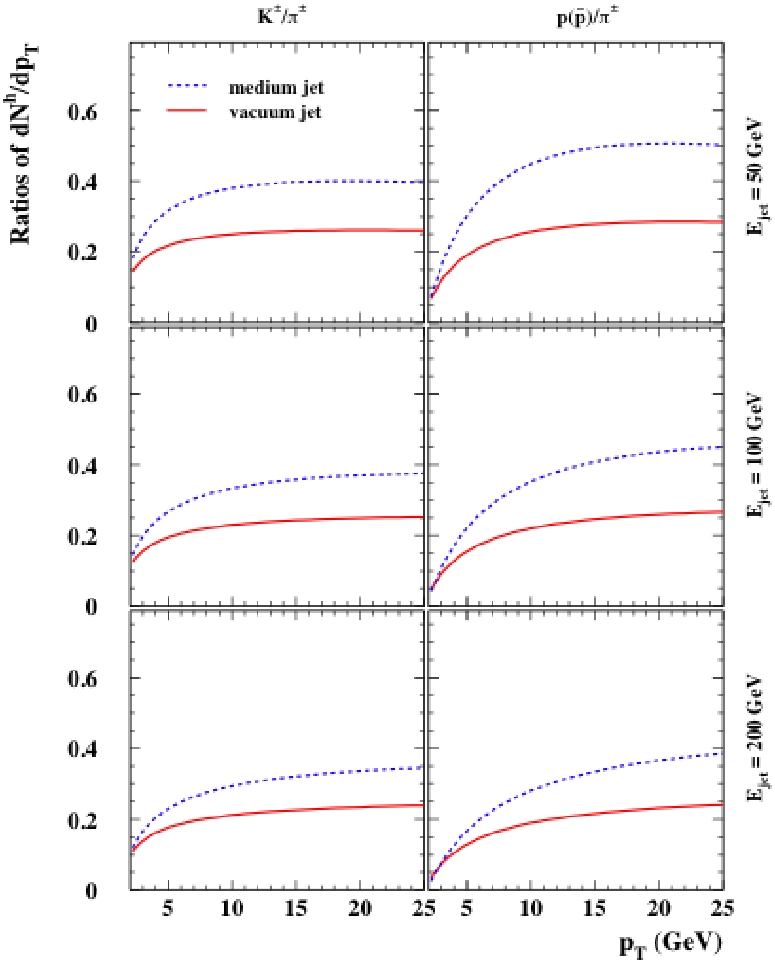

Figure 3.12: Results of the MLLA+LPHD formalism for $K^{\pm}/\pi^{\pm}$ and $p(\bar{p})/\pi^{\pm}$ ratios in jets with energies Ejet = 50, 100 and 200 GeV [83]. The enhancement in both ratios increases with decreasing jet energy and the onset of the enhancement occurs more sharply at lower jet energy

it is expected to occur in the p_T region 2-6 GeV/c, where recombination is predicted to dominate the inclusive spectra. The signature for flavour conversions in jets would likely be an increase in the yields of kaons and Λs at high p_T [89]. The enhancement could lead to a significant increase in the R_{AA} for kaons in comparison to pions at high p_T away from the recombination range (p_T >5 GeV/c).

The jet spectra analysis performed in this thesis will not try to replicate the predictions in figure 3.12 as the study was performed using jet energies and hadron momenta that cannot be studied at RHIC due to statistical limitations. The analysis will determine whether strangeness or baryon enhancement can be observed from the $Au + Au$ jet spectra, albeit at the lower end of the p_T spectrum where the enhancement is smaller. The results of this analysis may also assist in explaining why the coalescence model does not fit the experimental data above a p_T of 4.5 GeV/c. By separating the hard jet component of an event from the soft thermal component, it will be possible to determine whether the fragmentation function should be altered in $Au + Au$ to account for an increased p/π^+ ratio or whether there remains a significant contribution from the thermal hadrons in the inclusive spectra that is skewing the p/π^+ ratio.

3.5 γ-Jet Events

Photons do not experience the high p_T suppression seen with charged hadrons and therefore retain their initial energy. Direct photons are created in hard scattering collisions either by Compton scattering ($q+g \rightarrow q+\gamma$) or by annihilation ($q+\bar{q} \rightarrow g+\gamma$), where the second particle fragments into a jet. These events can be used to quantify jet suppression using the photon energy as an indicator of the initial jet energy. Furthermore, identifying dijets in heavy ion collisions using high p_T triggers is made more challenging due to the high p_T suppression of hadrons that ultimately leads to a bias towards jets that have experienced less attenuation. This is not the ideal situation when trying to analysis jet modification in the medium. γ-jet events are considered to be the ideal probe that can be used in study jets in heavy ion collisions as they do not suffer from a bias to jets with less attenuation.

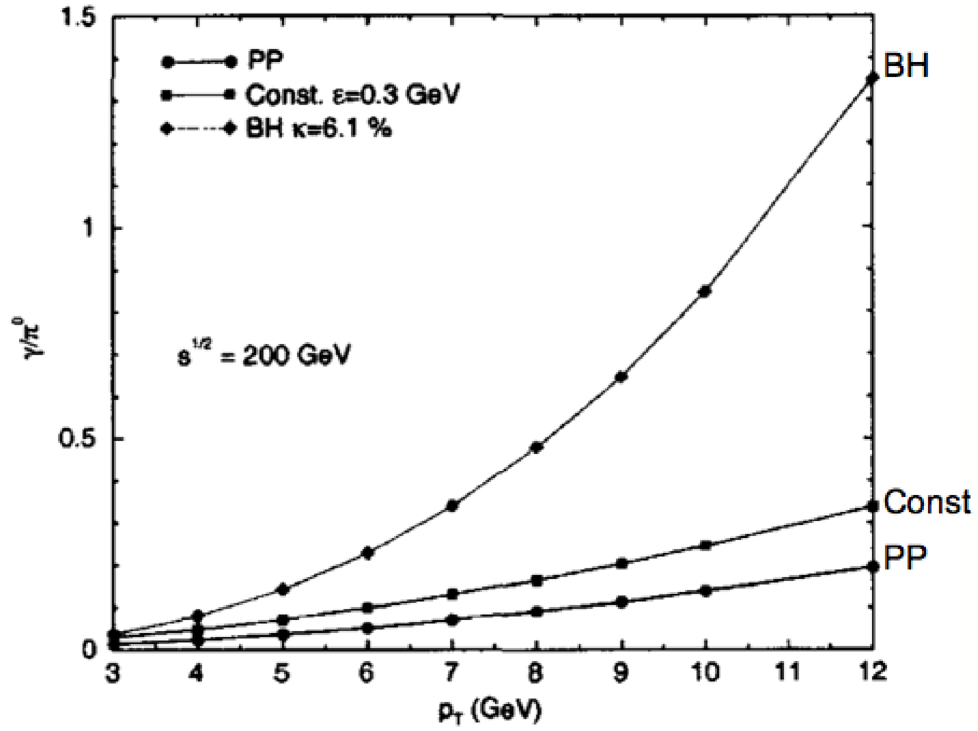

Figure 3.13: The γ/π^0 ratio as a function of p_T at $\sqrt{s_{NN}} = 200$ GeV. The three curves demonstrate the model dependence of the γ/π^0 ratio. The *PP* curve has been calculated for $p + p$ collisions, the *Const* curve and *BH* curves have been calculated using $Au + Au$ collisions. The γ/π^0 ratio is seen to climb steeply when an energy dependent suppression factor, *BH* is applied to the π^0 inclusive cross section [90].

The ratio of direct photons to π^0s has been calculated using perturbative QCD for $Au + Au$ collisions at $\sqrt{s_{NN}} = 200$ GeV [90]. The inclusive cross section for π^0 mesons was modified to include a parton distribution that accounted for nuclear shadowing and a fragmentation function that incorporated energy dependent energy loss to mimic high p_T suppression. Figure 3.13 shows the resulting γ/π^0 ratio for different systems, $p + p$, $Au + Au$ using a constant energy loss factor and $Au + Au$ using an energy dependent energy loss factor. Using an energy dependent suppression greatly increases the γ/π^0 ratio, which reaches unity at $p_T \sim 10$ GeV/c. The energy dependent suppression has been shown to quantitatively agree with π^0 data from PHENIX [91]. Therefore, there is expected to be a higher γ/π^0 ratio in $Au + Au$ collisions than $p + p$. Despite the increased γ/π^0 ratio, the neutral triggered data is still expected to be dominated by π^0 mesons as the electromagnetic calorimeter energy threshold used in this analysis was set at E_T greater than 6 GeV.

Chapter 4

THE STAR EXPERIMENT

4.1 The Relativistic Heavy Ion Collider

The Relativistic Heavy Ion Collider (RHIC) collider began operations in 2000 and remains the highest energy collider of heavy ions today. RHIC comprises two hexagonal concentric beam pipes with circumferences of 3834 m and can accelerate a range of ions from protons to gold [92]. To manipulate the beam, 1,740 radio frequency superconducting magnets are distributed around the curved corners of the collider. Multiple beam energies are accessible depending on ion species, with the current maximum beam energies being 100A GeV for gold collisions and 250 GeV for protons. Figure 4.1 shows that RHIC is an extension to the Alternate Gradient Synchrotron (AGS), which is now part of the RHIC injection system. The AGS accelerates ion beams up to a maximum of 10.8A GeV before injection into RHIC. Prior to the AGS, the ions are stripped of their electrons at specific points during the injection cycle as depicted in figure 4.1. Once a steady beam has been established, it can be maintained in the RHIC rings for several hours.

There are six beam-crossing points, located at four of the crossing points are the experiments, STAR [93], PHENIX [94], BRAHMS [95] and PHOBOS [96]. The experiments PHOBOS and BRAHMS ceased taking data in 2005 and 2006 respectively. Each experiment has its own unique features and strengths culminating in an extensive collective study of the nuclear matter created at RHIC. The two smaller experiments, PHOBOS and BRAHMS, benefitted from high sampling rates and a large rapidity reach respectively. PHENIX was designed to observe electromagnetic probes such as those from the dilepton decay of heavy particles. STAR is a high acceptance experiment designed to study the large multiplicity events created in heavy ion collisions. Although with some electromagnetic capability, STAR has been optimised to study charged hadrons and features full azimuthal coverage over a limited rapidity interval centered at mid-rapidity.

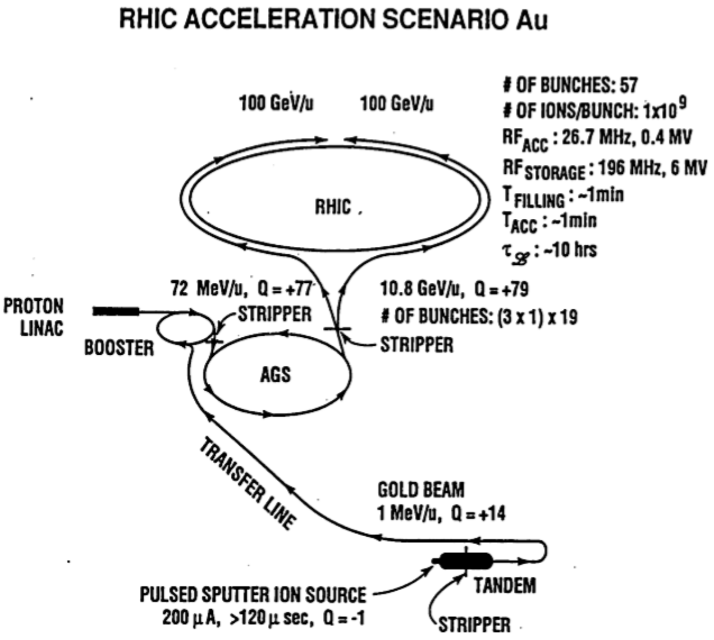

Figure 4.1: A schematic view of the RHIC accelerator complex [92].

4.2 STAR

STAR (Solenoidel Tracker At RHIC) is situated at the 6 o' clock position of the ring and is one of the larger experiments alongside PHENIX. STAR began taking data in 2000; shown in table 4.1 are the brief details of the different experiments and the number of events recorded for analysis. Improvements made to the RHIC facility and STAR sampling rate has allowed for an increase in the available statistics each year. With high statistic data sets, STAR can now be used to study rare processes such as jets and heavy flavour physics. In reference to the current analysis, data shall be taken from the 2007 $Au + Au$ run and from the 2008 $d + Au$ run. Further details of event statistics and selection criteria will be given in chapter 5.

STAR was primarily designed as a hadron detector utilising the full azimuthal coverage of a Time

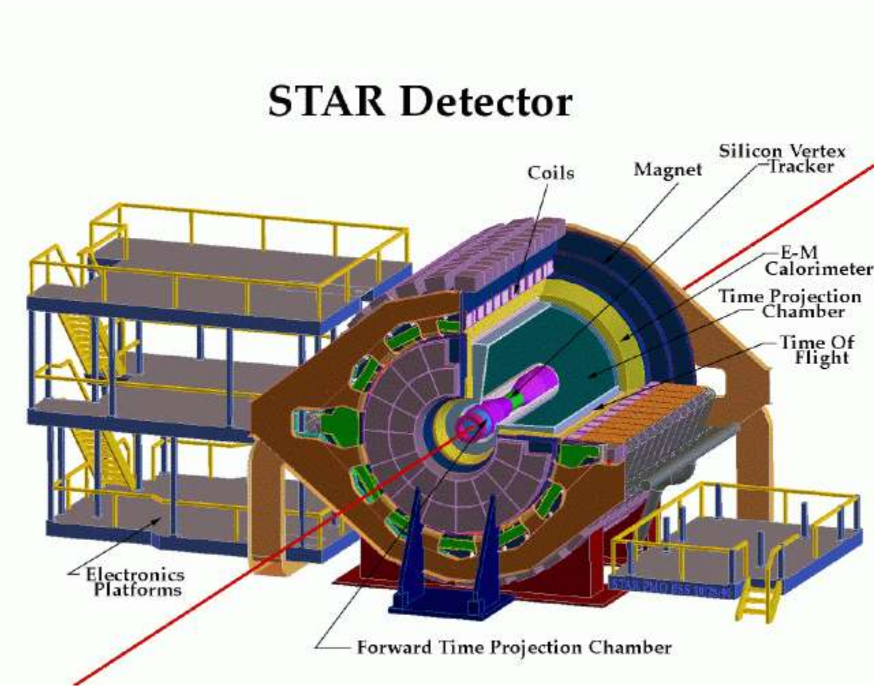

Figure 4.2: The composite detectors of the STAR experiment [93].

Projection Chamber (TPC) to track charged hadrons expelled by the collision as seen in the centre of figure 4.2. A Silicon Vertex Tracker, which sits between the TPC and the collision vertex, provides further track points and improved collision vertex resolution via three tracking layers at 5 cm, 10 cm and 15 cm radially from the nominal beam line. A solenoidal magnet encompasses the central rapidity detectors and is essential for charged particle identification in the TPC.

Over the past nine years of operations there have been upgrades to STAR including an ElectroMagnetic Calorimeter (EMC). Completed in 2005, The EMC consists of two components, a full barrel around the TPC and an end cap on the west side of STAR. A section of a time of flight detector has been incorporated into the STAR experiment and should be fully installed for the 2010 run. For the purposes of this thesis the TPC and the EMC will be described in detail along with the analytical methods utilised to identify jets and hadrons.

4.3 The Time Projection Chamber

The Time Projection Chamber (TPC) is the central element of an array of detectors that constitute STAR. It can reconstruct tracks from charged hadrons with momenta in excess of 100 MeV/c

Table 4.1: RHIC run data since operations began in 2000. The quoted number of events are from the 200 GeV heavy ion data sets. The increase in events does not linearly reflect the performance of STAR/RHIC as each run had different trigger settings using different detectors, each of which ran for different periods during each run.

Year	Experiment	Energy $\sqrt{s_{\mathrm{NN}}}$ GeV	Number of MinBias Events (Millions)
2000	Au + Au	130	1
2001/02	$Au+Au$ & $p+p$	200	1
2003	$d+Au$ & $p+p$	200	15
2004	$Au+Au$	200 & 62	40
2005	$Cu+Cu$	200 & 62	65
2006	$p+p$	200 & 62	99
2007	$Au+Au$	200	90
2008	$d+Au$ & $p+p$	200	46

from particle multiplicities of $\sim$ 3000 tracks per event in central Au + Au collisions. Particle identification is achieved by recording the momentum, charge and the ionisation energy loss ($\frac{dE}{dx}$) of charged particles as they pass through the chamber. The TPC coverage ranges from ± 1.8 units in pseudorapidity along with the aforementioned full azimuthal coverage.

The STAR TPC consists of two cylindrical drift chambers separated by a thin conductive central membrane situated at zero pseudorapidity seen clearly in figure 4.3. Each drift chamber is 2.1 m in length and 4 m in diameter. The TPC is situated within a uniform magnetic field, provided by the outer solenoidal magnet, with a nominal field strength of 0.5 T. The magnetic field bends the paths of charged particles allowing the track momentum to be calculated from the curvature and charge identification from the direction of curvature. Within the TPC itself, is an electric field which lies parallel to the beam axis. The uniform electric field is provided by the -28 kV central membrane and is controlled by the inner and outer field cages, the end caps are grounded at $\pm$ 2.1 m. The field cages, situated at 0.5 m and 2 m from the beam axis, consist of copper strip resistors that maintain a uniform field within the drift chamber. The chamber is filled with a P10 gas (90% Ar, 10% CH_4) maintained at 2 mbar above atmospheric pressure. The gas composition has been selected due to the high drift velocity (5.45 cm/μs) in a respectively low electric field corresponding to a drift time of $\approx$ 40 μs.

At either end of the TPC are the anode end caps each consisting of 12 wedge shaped sectors that are

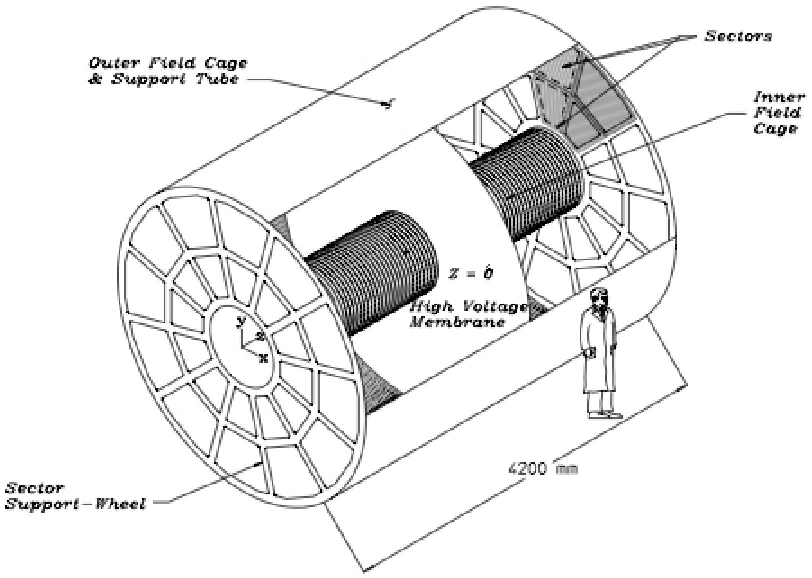

Figure 4.3: The STAR TPC [97]

in turn divided into 45 pad rows with a total 68,304 pads. The pad rows are not evenly distributed as each sector is split into an inner and outer section. Figure 4.4 shows how the inner and outer pad rows consist of 13 and 32 rows respectively. The inner pads are shorter in order to distinguish tracks from the high density inner region, close to the beam pipe, and to identify the large curvature of low momentum tracks. The larger outer pads help to improve the $\frac{dE}{dx}$ resolution.

Charged particles ionise the TPC gas molecules liberating electrons that drift to the ends of the TPC under the influence of the electric field. At the end of the drift region is a gating grid that can be triggered open if the event has been selected for recording. The accepted electrons pass through a shield grid, where the drift chamber potential is grounded, into a proportional region. Here the electron signal is amplified by accelerating the drift electrons using anode wires, held at a potential of 1265V, causing secondary ionisation. The pad rows lie beyond the anode wires where an image charge is induced by positive ions drifting away from the pads. The image charge is the TPC signal that can be recorded as part of the event data.

The TPC has a sampling rate of 9.4 MHz and 512 time bins per sample that in correspondence with the drift velocity creates a temporal analysis of the track path. By registering the charge arrival time at the pad, an accurate account of the z component (parallel to the beam) of position is obtained. The pad coordinates complete the spacial description of the track with the x coordinate taken along the pad row and the y coordinate taken perpendicular to the pad row. Considering the total number of pads and sampling rate of the TPC, a three dimensional array of $\sim$ 70 million pixels are available per event.

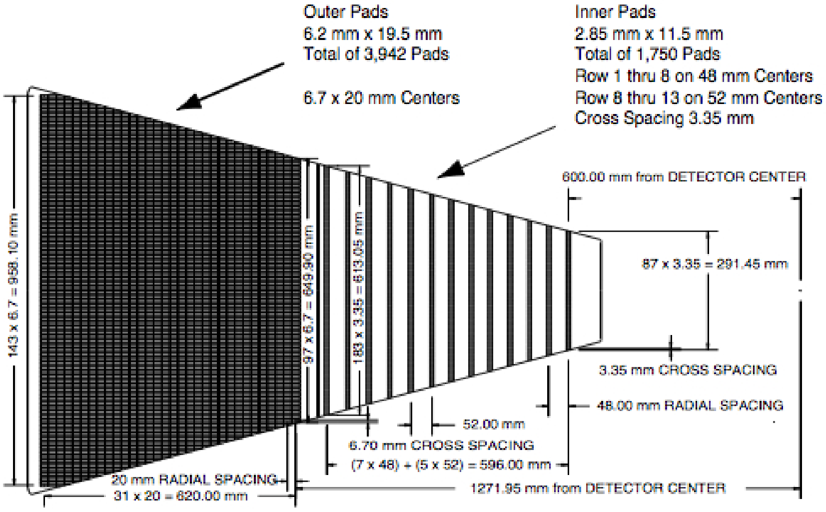

Figure 4.4: A sector from the anode pad plane showing the arrangement of the inner and outer pad rows[97]

4.3.1 Track reconstruction

The track of a charged particle passing through the TPC is reconstructed by separately matching ionisation clusters in the x, y and z space. The cluster finder searches for an image charge on adjacent pads, within a pad row of comparable drift times. Once a cluster is found, the energy from all the pads is summed to give the total ionisation signal for that cluster. Overlapping clusters that correspond to two separate tracks can be separated using a peak finding algorithm that looks for two peaks in the ionisation signal.

The coordinates of a cluster are determined by assuming the signal distribution across the pads in the cluster is Gaussian. 2-dimensional Gaussian fits are performed on the clusters to determine their centroids. Once the x and y centroids have been established, the z coordinate is computed, along with adjustments for experimental effects such as non-uniformity of the electric or magnetic field, to create spatial points. Beginning with the outermost spatial points, where the track density is lower, global tracks are reconstructed by linking together the points in sequence towards the centre of the detector.

When the inner TPC boundary is reached, the tracks are extrapolated to the beam axis in order to establish the primary vertex. Once the vertex position has been found it is then added as an additional spatial point for all the tracks. The reconstruction algorithm is rerun in an attempt to better fit the primary tracks, those that point back to the primary vertex. Tracks that do not point back to the primary vertex are retained as global tracks. A reconstructed central $Au + Au$ collision at $\sqrt{s_{NN}} = 200$ GeV is shown in figure 4.5. The image is produced as part of the offline tracking process discussed in this section.

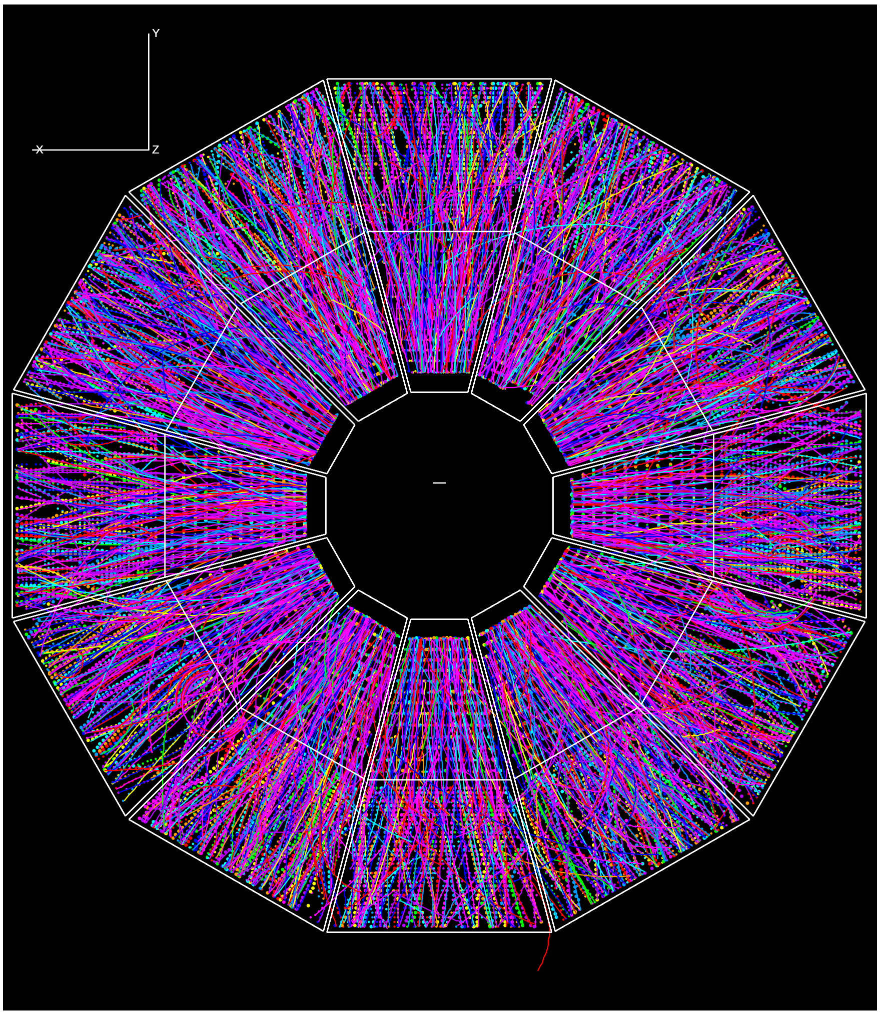

Figure 4.5: Reconstructed TPC tracks from a central $Au + Au$ collision at $\sqrt{s_{NN}} = 200$ GeV. The TPC is viewed parallel to the beam axis.

There are several reasons why some tracks would not point back to the primary vertex. Firstly these tracks could be the decay products of heavy or strange hadrons and would therefore point back to their decay vertex. There can exist multiple vertices reconstructed by TPC tracks within a given triggered event. This is mainly due to particle pile-up in the TPC where earlier or later collisions are also detected as part of the selected collision. Due to the different electron drift starting times, these additional events appear shifted in the z direction on either side of the central membrane. These pile-up vertices are usually less well defined due to a lower track multiplicity and asymmetric pseudorapidity distributions.

4.3.2 Centrality definitions

The data from reconstructed events can be categorised off-line into centrality classes from central (small impact parameter) to peripheral (large impact parameter) collisions. The event multiplicity is used to determine to which centrality class the event belongs. A reference multiplicity that only includes tracks within the pseudorapidity interval $|\eta| < 0.5$ is used to determine the boundaries of each centrality class. The reference multiplicity negates the need to consider tracking efficiencies as a function of primary vertex position as the edges of the TPC range should not be included. The reconstruction efficiency is high and approximately constant, $\sim 90\%$, in the selected range however it does depend on p_T. The reference multiplicity is then integrated into segments of ~ 10 % of the total distribution. The concept is that the highest segment relates to events with the smallest impact parameter (central collision) and each subsequent segment relates to a set of collisions with a larger impact parameter. These segments are shown in figure 4.6 where the most central collisions are shown in red and the most peripheral shown in blue.

Each centrality corresponds to a different range in N_{part} and N_{bin} earlier defined in section 2.1. Glauber model Monte Carlo calculations relate the initial collision parameter conditions, such as impact parameter, number of participants and number of binary collisions, to the reference multiplicity recorded in the data [24]. For this analysis, only a general idea of centrality is needed to separate peripheral collisions from central collisions. As the tracking efficiency is relatively independent of multiplicity, the uncorrected distribution gives the correct fraction of the cross-section. Therefore the integration method will suffice in separating central and peripheral collisions.

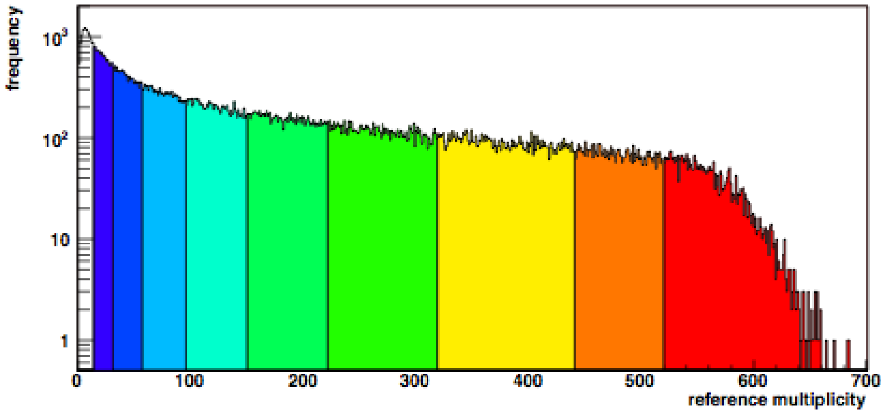

Figure 4.6: Reference multiplicity distribution for off-line centrality definition, in $Au + Au$ collisions at $\sqrt{s_{NN}} = 200$ GeV. The fill colour represents the centrality class. From red to blue: 0-5%, 5-10%, 10-20%, 20-30%, 30-40%, 40-50%, 50-60%, 60-70%, 70-80%.

4.4 The Barrel Electromagnetic Calorimeter

The Barrel Electromagnetic Calorimeter (BEMC), as can be seen in figure 4.7, is situated around the TPC and covers roughly ±1 unit of pseudorapidity and the full azimuthal angle. The BEMC detects the energy of electromagnetically interacting particles and is specifically designed to target photons and electrons from rare events as well as π^0 and η meson decays and charged hadrons with high p_T.

The BEMC was one of the first upgrades to the STAR experiment. The initial layout of STAR was designed to allow space for the construction of a BEMC that could be installed in stages. A flexible lead and plastic (Kuraray SCSN81) scintillator was chosen that could be installed relatively easily in the form of individual thin modules. This choice of scintillator is also cost effective considering the BEMC has to cover 60 m^2. Another constraint on design is that the PhotoMultiplier Tubes (PMTs) must be situated outside the magnet coils along with the front end electronics (FEEs) and the high voltage system. The added bonus is that the near zero magnetic field allows for a less complex and thus more cost effective PMT system. Yet the scintillator radiation still requires transportation to the PMTs. In order to combat this issue a combination of plastic wavelength shifting and clear optical fibers had been selected for the STAR design.

The BEMC consists of 120 modules, which individually cover 1 unit in pseudo-rapidity and 0.1

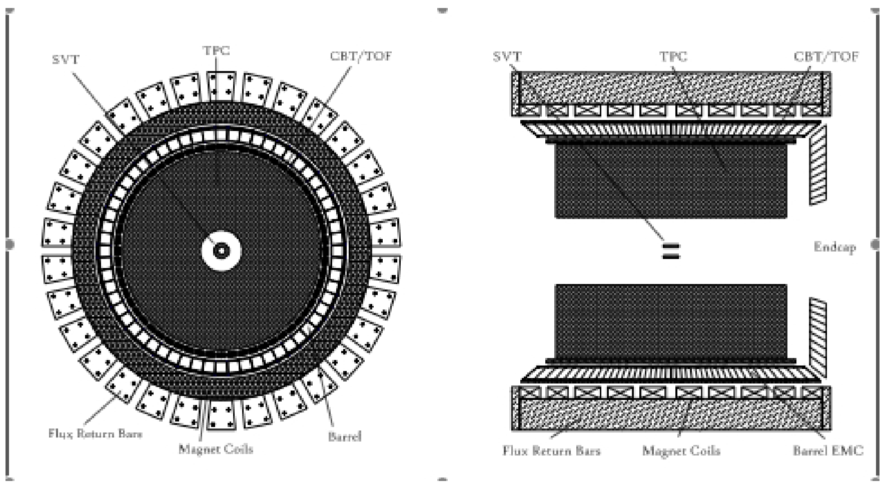

Figure 4.7: Cross-section of the STAR EMC [98]

radians in azimuth. An individual module comprises of 20 layers of 5mm thick lead, 19 layers of 5 mm thick scintillator and 2 layers of 6 mm thick scintillator. The core structure, known as the stack and shown in figure 4.8(b), is compressed by a combination of 30 straps that maintain an average internal pressure of 1 bar. The stability of the stack is maintained by the friction between individual layers thus the layers are prevented from sliding in any direction. The plastic scintillator has been machined to contain 40 optically isolated tiles on each layer. The tiles have a WaveLength Shifting (WLS) fiber embedded in a σ *groove* so that the signal from each tile can be readout individually. A signal is taken from overlaying tiles from each of the 21 scintillator layers that progress into the module and streamed to a single decoder box mounted outside the STAR magnet. The light from the decoder box is the signal from an individual tower and the signal is then merged onto a PMT.

Figure 4.8(a) shows an example of a single module that is segmented into 40 towers. Each tower has been positioned in a projective manner pointing to the centre of the interaction diamond. The towers themselves cover a range of 0.05 in both η (pseudorapidity) and ϕ (azimuth). The tower dimensions allows for the containment of shower energies up to 60 GeV, a total depth of $20X_0$ at η =0, and reasonable single particle occupancy.

The first stage of a tower, the pre-shower detector, registers the particle shower development after only 1 -1.5 radiation lengths (X_0) in the tower and is built from the 6mm scintillator layers. The radiation length varies with particle species as it refers to both the mean distance over which a high-energy electron loses all but $\frac{1}{e}$ of its energy by Bremsstrahlung, and $\frac{7}{9}$ of the mean free path

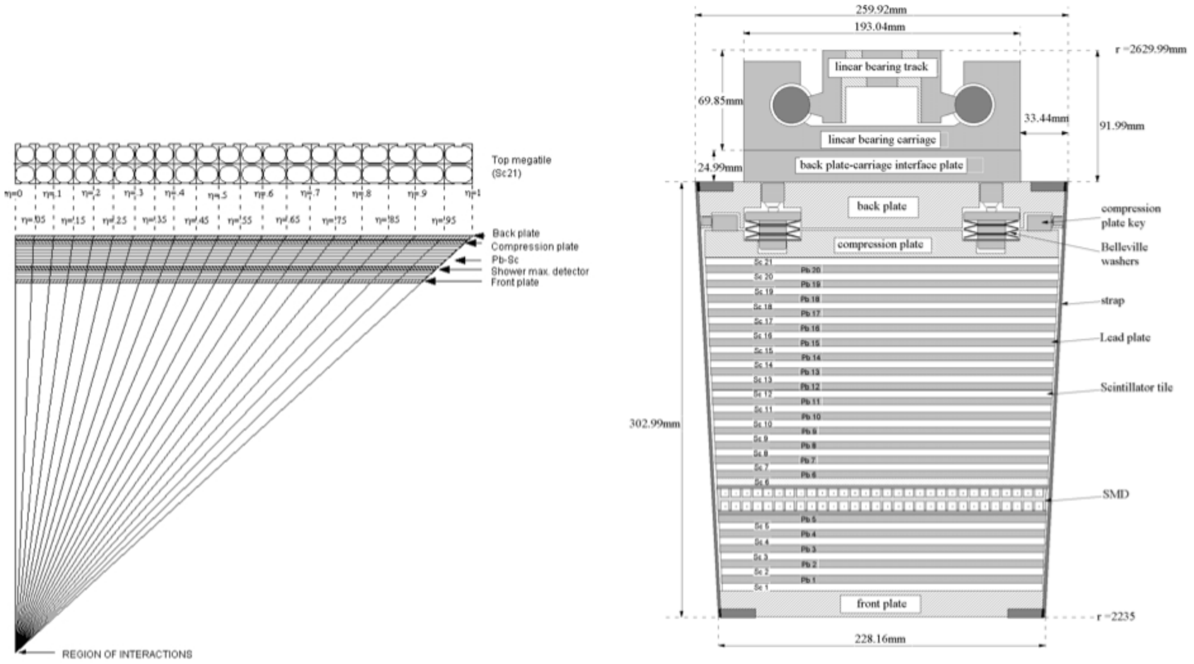

(a) (b)

Figure 4.8: Schematic diagrams illustrating the construction of a STAR BEMC module [98]. Image (a) shows the longitudinal view of a single STAR BEMC module showing the projective nature of the towers, while image (b) is the end view of a STAR BEMC module showing the mechanical assembly and rail mounting system

for pair production (e^+e^-) by a high-energy photon. The signal from the pre-shower detector is extracted by four WLS fibers where one pair is taken to the PMT to calculate the total energy signal and the second pair of fibers illuminates a single pixel of a multi anode PMT. There exists a total of 300, 16 pixel multi-anode PMTs with each individual pixel corresponding to the pre-shower signal of each tower. Hadrons and electrons behave very differently in this first stage where ≈63% of electrons (≈3% for hadrons) will shower before entering the pre-shower range and ≈84% (≈6% for hadrons) shower by the middle of the pre-shower range. This behaviour greatly improves electron/hadron discrimination in the BEMC.

Within the stacks of lead/scintillator is the Shower Maximum Detector (SMD). The SMD can be seen in figure 4.9 below a cut away image of preceding scintillator stacks revealing the electromagnetic shower development before reaching the SMD. The SMD is essentially two layers of gas wire pad chambers situated $\approx 5.6\ X_0$ within the tower stack at $\eta = 0$ and a range of depths along the module due to the projection of towers at different η values. The tower dimensions are not comparable to the significantly smaller Moliere radius of the scintillator stack. Therefore the SMD was incorporated into the design to produce high spatial resolution of the electromagnetic showers, which is vital for π^0/γ discrimination.

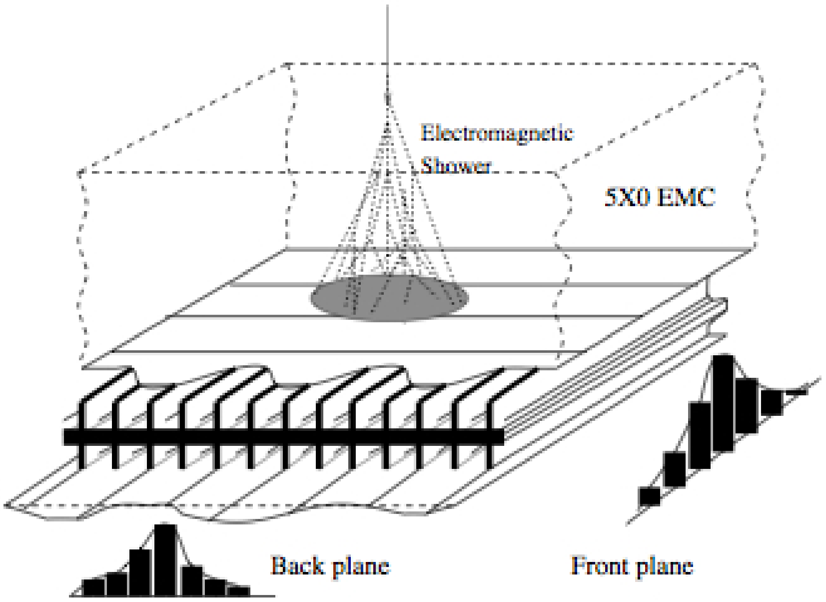

Figure 4.9: An illustration depicting the reconstructed image of the electromagnetic shower front [98]

A unique feature of the STAR SMD is the double layer design permitting two independent mutually orthogonal planes of proportional wires. This novel design improves the reliability, and functionality of the SMD in a high occupancy environment as well as improving hadron rejection and π^0/γ separation. Strips (cathodes) are etched in perpendicular (η and ϕ) directions on the two planes reconstructing a two dimensional image of the shower front that can be seen in figure 4.9 where the front and back planes are displayed as histograms. While referring to figure 4.10, the SMD double layer system can be explained in more detail. Between the planes, 5mm wide aluminium extrusion channels that run in the ϕ direction contain 50μm gold plated tungsten wires (anodes) that are 1 unit in η long. The detector strips (cathodes) are sensitive to the induced charge fluctuations from the charge amplification near the wire. The η direction strips span 30 channels corresponding to a length equal that the width of the module and 0.0064 in η, while the ϕ direction strips are 1.33cm wide and have lengths 0.1units in η.

The signal from the cathodes is very small, $\approx$7 femto coulombs per minimum ionising particle, therefore it is propagated to the FEEs at the ends of the EMC along a transmission line plane

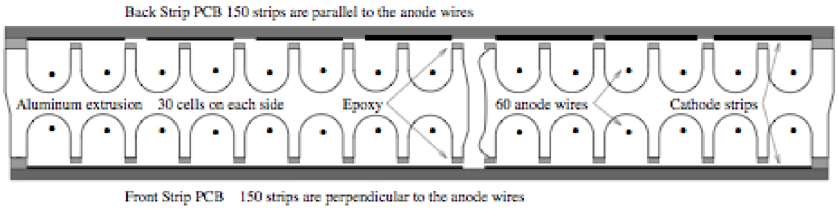

Figure 4.10: Cross section view of the aluminum protrusions and the anode wires and cathode strips of the STAR BEMC SMD [98]

located between the cathode plane and the outer enclosure of the detector to avoid any noise that could be provided by the STAR magnet. The signals from 36000 readout channels from each individual strip are then amplified to external digitilisers situated outside the STAR magnet.

4.5 Event Selection

Each event created in a heavy ion collision is unique as the final state is governed by a large number of sub-processes that occur throughout the evolution of the event. In heavy ion collisions, the number of possible final states is further increased by the impact parameter from central to peripheral collisions. Event sampling rates are limited by the performance of the detectors and not by the event frequency. At current RHIC luminosity, the collisions rate reaches $\sim$10 kHz, which is much larger than the data acquisition rate of 100 Hz. Therefore, fast detectors can be used to select specific events (for example central collisions) for data acquisition within the sampling rate of slower detectors. The process of selecting events is known as triggering and is useful for collecting rare events without the need for recording vast quantities of unwanted data.

The STAR trigger is a piplined system that has been designed to examine fast detector signals at the RHIC crossing rate ($\sim$ 10 MHz) [99]. The STAR trigger consists of four consecutive levels of selection that the event must pass before being sent to storage. The decision to store an event is made at level-3, which is the final level and a software trigger, where information from fast and slow detectors are available. The level-0 trigger is the first stage of the triggering process and issues a decision to progress to level-1 within 1 μs of the interaction taking place. The level-0 trigger issues a command to the slow detectors specified for that particular trigger to record data.

While the slow detectors produce their signal, the level-1 trigger is examining a subset of the fast detector signal to establish whether there is a clear signal, free of any background effect, that can be forwarded to level-2. At level-2, the entire trigger data taken from the fast detectors can be used to select events that pass more stringent trigger requirements.

Level-2 can be used to isolate collisions that carry rare events. Events containing jets may be selected by identifying their signature signals such as a high energy deposit in a single EMC tower. Level-1 operates within a decision time of $\sim$ 100 μs while level-2 has a time restraint of $\sim$ 5 ms. If the event is not aborted at level-1 or level-2, the data is passed to the Data Acquisition (DAQ) system where the level-3 trigger finally decides what data is stored.

4.5.1 Trigger detectors

There exists a number of fast detectors that provide the signal for the level-0 trigger. Level-0 trigger detectors do not suffer from dead time and are capable of detecting events at each beam crossing. The main trigger detectors are the Zero Degree Calorimeters (ZDCs), that are situated ±18.25 m along the beam pipe away from the central rapidity detectors, the Central Trigger Barrel (CTB) that surrounds the TPC and the EMC.

The ZDCs detect neutrons within a small solid angle near zero degrees from the beam line that have been liberated during a heavy ion collision. A coincidence, within a given time window, of neutrons in both ZDC detectors indicates that a collision has occurred. The timing of the signal taken by the ZDCs can be used to disregard events occurring away from the centre of the experiment ($z = 0$). The CTB is made up of a cylindrical array of 240 scintillation detectors. It detects the charged particles created in the mid rapidity region and is used to determine the charged particle multiplicity of the event. The CTB signal works in tandem with the ZDCs to estimate the centrality of the collision.

The EMC level-0 signal can take two forms that both use the transverse energy of the event. Either 300 tower sums are taken from patches 0.2 by 0.2 in η and ϕ or 300 high tower values from the highest energy tower in each patch are taken. This signal is processed to make a final level-0 trigger decision based on total E_T. The EMC was the trigger detector for the *Au* + *Au* data and was used to detect jet events in the *d* + *Au* data used in this analysis.

A level-2 BEMC trigger was used to collect the 2007 $\sqrt{s_{NN}}$ = 200 GeV *Au* + *Au* data used in this analysis. The trigger was designed to isolate hard scattering events where the initial scattering produced a high energy photon. The trigger requirements were that at least one tower must register E_T greater than 5.5 GeV. In addition, the level-2 trigger had another requirement that the E_T from a pair of adjacent towers must sum up to a value greater than 7.5 GeV. A similar trigger was selected to collect data from the 2008 $\sqrt{s_{NN}}$ = 200 GeV *d* + *Au* data. A high tower trigger, where an event is selected if a BEMC tower registers an E_T greater than 4.3 GeV, was chosen to provide a reference sample. The *d* + *Au* data set should therefore contain similar triggers to those expected in the *Au* + *Au* data set selected for the current analysis.

4.6 Particle Identification

The TPC is the primary detector for the majority of the particle identification performed in STAR. Charged particles can be identified by comparing the loss of energy per unit length ($\frac{dE}{dx}$) with the momentum of the particle. The momentum of a charged particle is calculated by fitting a circle through the points along the track in the $x-y$ plane. The radius of curvature and the angle the track makes with respect to the beam axis in the $r-z$ plane are then used to calculate the momentum. In high track density environments, momentum smearing may occur when track points are assigned to the wrong track.

The effects of momentum smearing can be minimised by increasing the magnetic field strength or using only tracks with a high number of pad hits. The momentum resolution of the TPC has been determined by measuring the momentum of simulated tracks that were embedded into real data. The results indicate that the resolution is momentum dependent and estimates that the resolution varies from 2-8% [97].

4.6.1 Energy loss

When charged particles ionise the gas in the TPC, they transfer energy to the liberated electrons. The $\frac{dE}{dx}$ of a cluster is measured by using the sum of the drift electrons to estimate the energy loss and dividing this value by the track path length along that particular pad row. Merged clusters, identified using a double peak finding algorithm, are not used to calculate energy loss as the energy deposited cannot be accurately assigned to the individual clusters. The energy loss along a selected track can vary from a few eV to hundreds of eV, therefore multiple hit clusters are used to calculate the most probable energy loss (Δ_p). A fit is performed to all clusters associated to a particular track and Δ_p is extracted. The calculation for Δ_p uses a truncated mean value that disregards the top 30% of cluster values. It can be inferred that the accuracy of the energy loss value relies heavily on the number of hit points used when using this fit method. For tracks crossing greater than 40 of the TPC pad rows, the resolution is estimated to be 5-10%. During this analysis, a cut on particles that used greater than 20 hits for energy loss calculations was imposed so as not to diminish the available statistics.

As mentioned earlier, the energy loss value obtained from the cluster fit is compared with the momentum of the track. The energy loss as a function of momentum follows the Bichsel function [101]. The Bichsel function uses Δ_p/x, where x is the segment length through a detector, to identify particles whereas alternative methods, such as the Bethe-Bloch formulation, use the mean energy loss [102]. Although the Bethe-Bloch formulation can be used to calculate Δ_p/x it does not consider the finite size and orientation of the detector pads unlike the Bichsel function [100].

The Δ_p/x dependence with segment length through an Argon detector can be seen in figure 4.11. The Bethe-Bloch function, shown in figure 4.11, has been scaled so that the minimum ionisation point has the same value as the Bichsel functions. The energy loss at high $\beta\gamma$ diverges away from the Bichsel function after the minimum ionisation point, implying that the energy dependence for the Bethe-Bloch differs from that for the Bichsel function. Due to the diverging nature of the results of the Bichsel and Bethe-Bloch formulae, it becomes more important at high momenta to use the more appropriate Bichsel formula.

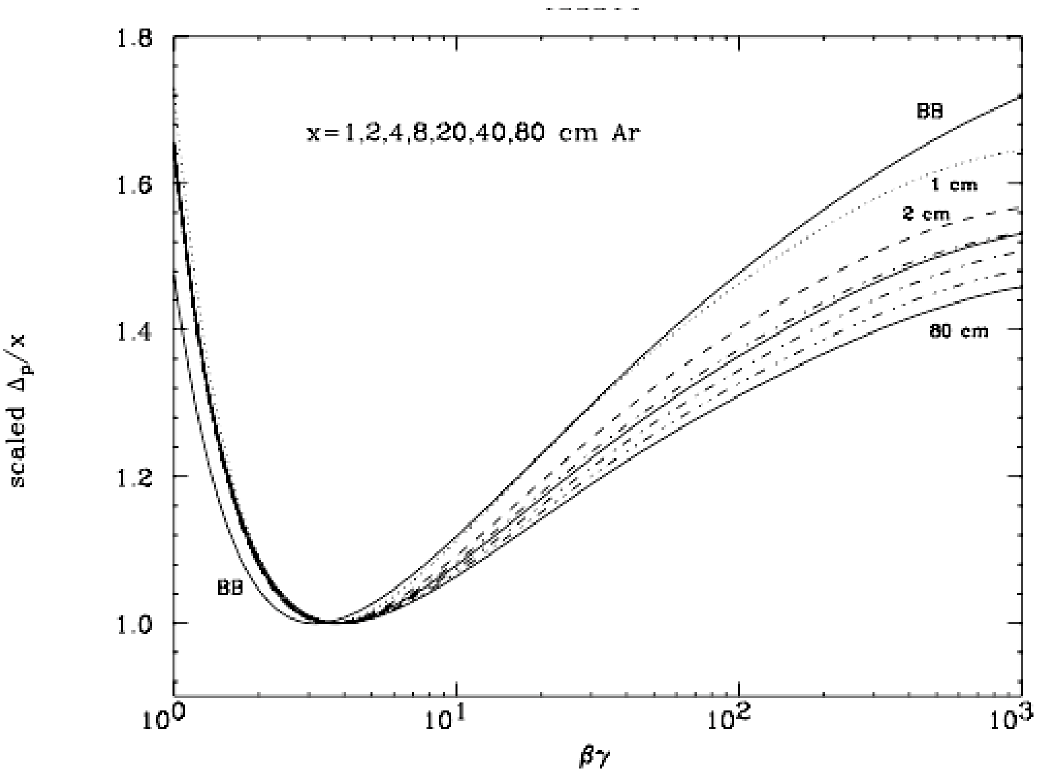

Figure 4.11: Scaled values of Δ_p/x for Argon segment lengths x as a function of particle momentum. The Bichsel functions (dashed lines) are shown to differ with segment length from the Bethe-Bloch function at higher $\beta\gamma$ [100].

The Bichsel function is based on Landau's equation for Δ_p shown in equation 4.1, where $\xi = xk/\beta^2$, k is the coefficient for collision cross-section, I is the logarithmic mean excitation energy of an absorber and $\delta(\beta)$ is the density effect [103]. Although this equation does not incorporate factors related to atomic structure, and therefore does not have the correct cross section, it does show that Δ_p varies as a function of x and β, which is the major adjustment from the Bethe-Bloch formula.

$$\Delta_p(x,\beta) = \xi \left[ln2mc^2\beta^2\gamma^2 - lnI + ln\frac{\xi}{I} + 0.2000 - \beta^2 - \delta(\beta) \right] \tag{4.1}$$

The STAR TPC was originally designed to discriminate between pions and protons up to a momentum of 1.2 GeV/c. Beyond this value, the energy loss, which for familiarity, Δ_p/x shall be denoted as $\frac{dE}{dx}$, becomes less mass dependent and requires a higher resolution detector to distinguish the particles. However, beyond 3-3.5 GeV/c, the particle species separate in $\frac{dE}{dx}$ again up to

∼10 GeV/c. The coloured bands displayed in figure 4.12 show the $\frac{dE}{dx}$ trends of pions, kaons, protons and electrons. In the top left panel, above $log_{10}(p) = 0.5$ (≈ 3.2 GeV/c), the proton and pion bands separate beyond the estimated 8% resolution of the TPC. Theoretically protons and pions should be distinguishable however the kaon and proton bands overlap. The overlapping bands does not allow for a simple $\frac{dE}{dx}$ cut that could isolate protons from kaons therefore a statistical approach will be required. The statistical approach consists of fitting the data with a function that consists of variable gaussian distributions, each one corresponding to a different particle. The Bichsel functions will be used to estimate the centroids of each histogram. A detailed description of the fitting method will be given in chapter 5.

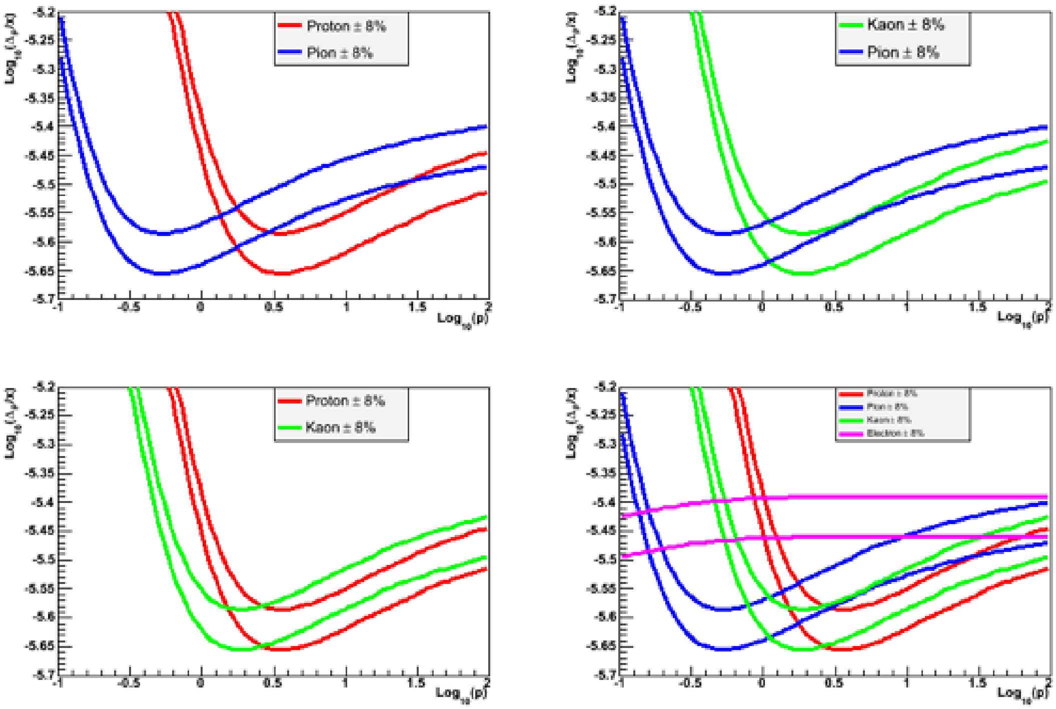

Figure 4.12: Bichsel functions for $\frac{dE}{dx}$ as a function of momentum for charged particles. The functions are shown as bands with an 8% resolution.

4.6.2 Neutral strange hadron reconstruction

Singly strange neutral hadrons (V_0) can be identified via their charged weak decay products. A secondary vertex, away from the primary vertex, is created when strange hadrons decay. This second vertex can be found by reconstructing tracks that point to an origin that is not the primary vertex. A set of geometric cuts can be performed to establish whether these secondary vertices are good candidates for V_0 decay vertices. These geometrical cuts are shown in figure 4.13 and they can be altered to either improve the purity of a sample or increase the statistics of strange hadron candidates.

In this analysis, Λ(uds) and $\bar{\Lambda}$ ($\bar{u}\bar{d}\bar{s}$) baryons were reconstructed. Their decay channels into charged hadrons can be seen in the below equations along with the branching ratios.

$$\Lambda \rightarrow p^{+}\pi^{-}(BR = 63.9 \pm 0.5\%) \tag{4.2}$$

$$\bar{\Lambda} \rightarrow p^{-}\pi^{+}(BR = 63.9 \pm 0.5\%) \tag{4.3}$$

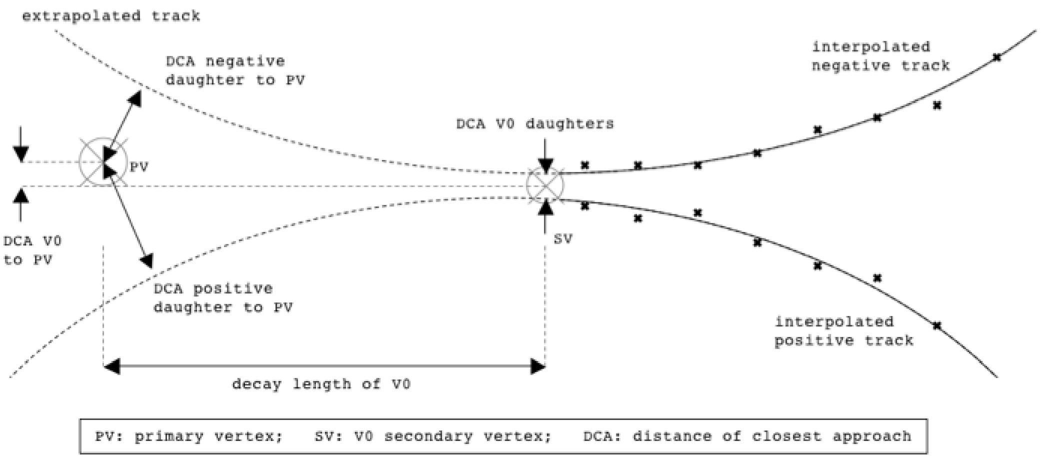

Figure 4.13: Strange hadron reconstruction using reconstructed TPC tracks. The geometrical cuts are also illustrated.

Once the V_0 candidates that have passed the geometric cuts have been collected they can be separated into Λ, $\bar{\Lambda}$ or K^0_{Short} candidates by assuming the identity of the charged daughters then reconstructing the invariant mass of the V_0 candidate. If a candidate can be reconstructed as both K^0_{Short} and Λ or $\bar{\Lambda}$ that candidate is rejected from the data. To limit the combinatoric background from random pairs of tracks, a tight invariant mass acceptance is applied. The tight mass range replaces a background subtraction as a background subtraction cannot remove individual tracks. The information from individual tracks is essential for two particle correlations. Although background corrections to the invariant mass distribution can be performed after the correlation the statistics in the selected $\Delta\phi$ bins may be too small to obtain a measurable mass peak especially in the intermediate/high p_T range.

Another useful outcome of identifying Λ and $\bar{\Lambda}$ is that their daughters provide a near pure sample of protons and anti-protons that can be used to calibrate the proton Bichsel function. This is made possible due to the proton carrying the majority of the momentum after the Λ has decayed. Unfortunately a pure source of pions is not obtainable in this manner from the decay products of K^0_{Short}, as each pion receives a similar share of the momentum. Thus a large sample of K^0_{Short} with a p_T greater than 6 GeV/c would be required, which was not feasible using the current statistics.

4.7 Two Particle Correlations

A jet finding tool that has proved effective on numerous occasions is two particle correlations [30, 104, 105, 106]. Two particle correlations reveal the angular distribution of particles relative to a fixed point in an event. For jet finding, the fixed point is the selected trigger particle that is believed to be the leading particle in the jet. Correlations are unable to identify jets on an event-by-event basis as the jet is indistinguishable from other particles in the event. Yet they are able to build a jet signal, summed over many events, that should be distinguishable from the underlying event.

The initial correlation procedure is very simple. Once a choice of trigger is made (usually the highest p_T particle in the event) the spatial coordinates of the remaining particles (associate particles) in the event are recorded relative to the position of the trigger. The parameters used throughout this analysis are the relative azimuthal distribution (track emission angle in $x-y$ plane perpendicular to the beam direction), $\Delta\phi$, and the relative pseudorapidity distribution, $\Delta\eta$. In figure 4.14, an image of a dijet has been imprinted onto a central $Au + Au$ event taken by STAR. The image shows that the TPC is saturated with tracks thus making jet identification difficult. However by performing a two particle correlation over many events the jet signal is extracted due to the consistent jet fragments that appear close to the trigger in each event. The majority of two particle correlations performed within STAR use TPC tracks to identify both the trigger and the associated particles. For this analysis the BEMC was used to detect the triggers (using a charged particle veto so that

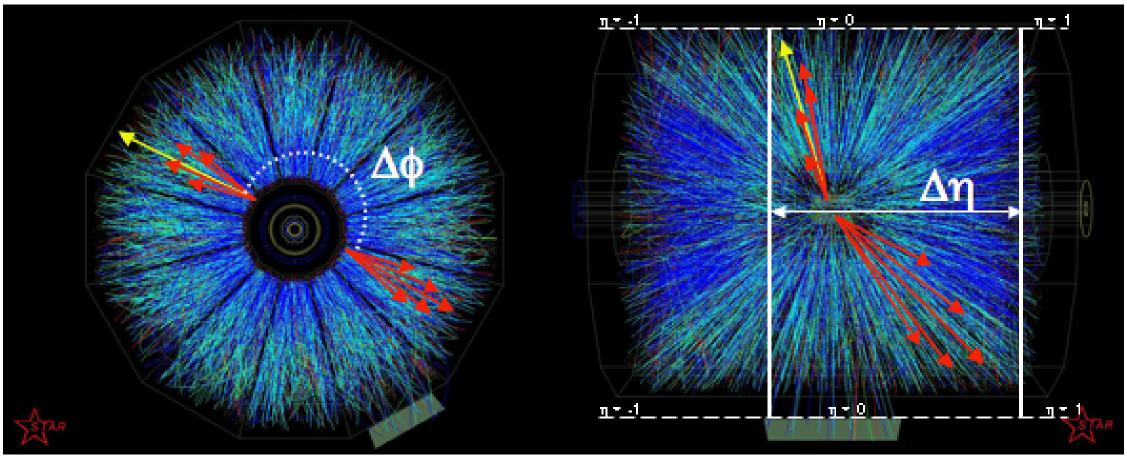

Figure 4.14: Schematic representation of a dijet occurring in a central $Au + Au$ event. The left panel views the event parallel to the beam axis while the right panel is perpendicular to the beam. The yellow arrow represents the trigger particle from where the spatial coordinates of all other particles are taken. The red arrows indicate the position of the jet fragments. The length of the arrow indicates the momentum of the particle.

the trigger was either a π^0 or γ) and the TPC was used to detect the associated particles.

4.7.1 Correlation signal

The signal produced from two particle correlations can be split into three distinct regions: the near-side jet, the away-side jet and the underlying event background. The relative contributions from the three regions can be adjusted by altering the p_T thresholds for the trigger and associated tracks. The background is created by selecting pairs that are not part of a dijet signal. These pairs could be a non jet trigger with any associated particle or a jet trigger with a non jet associated particle. The incidence of non jet triggers can be reduced by selecting a high p_T threshold for trigger candidates. Likewise the incidence of non jet associated particles can be reduced by raising the associated particle p_T threshold. Yet the thresholds must remain low enough to target the physics that motivated the correlation study. Raising the trigger thresholds restrict the number of events that are selected and high associated thresholds diminish the jet signal that can be extracted.

A schematic view of a two particle correlation performed in the azimuthal plan is shown in figure 4.15. The near side peak (red) is created by pairs where the associated particle belongs to the same jet as the trigger, while the away side peak (green) is created by pairs where the associated

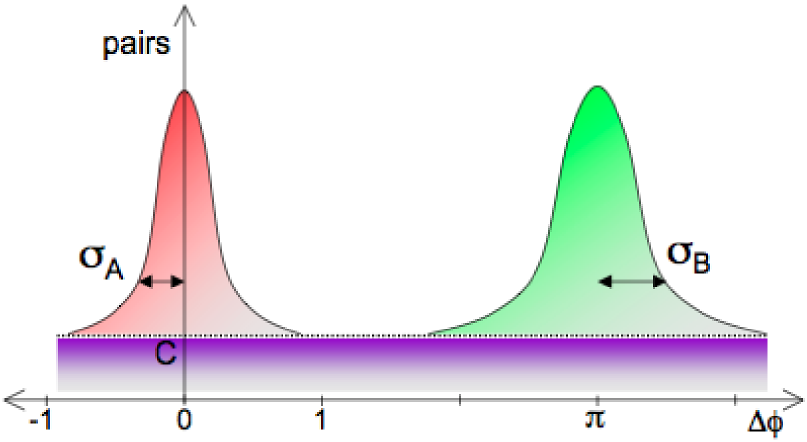

Figure 4.15: Schematic representation of a two-particle azimuthal correlation. The horizontal axis represent the angular separation of trigger and associated tracks. The widths of the near side and away side peaks are labelled σ_A and σ_B respectively. The level of the background is given by C [107].

particle belongs to the second jet. Although the jet signal is created by dijets the two peaks can be very different. The width of the away side peak, σ_B is generally measured to be larger than the width of the near side peak, σ_B. This is the result of a trigger bias toward the near side jet as it always contains the trigger particle. The jet containing the trigger particle will be the harder jet with fewer fragments carrying the jet energy in a narrower cone. The away side jet must have a softer profile as it does not contain the trigger, therefore there are more particles carrying the jet energy in a wider cone. Furthermore, partons within the colliding bodies would have had finite transverse momentum before the collisions leading to dijets that are not exactly back-to-back in $\Delta\phi$. By aligning with the trigger, the away side peak is smeared about $\Delta\phi = \pi$ widening the peak. In heavy ion collisions the near side peak is further biased as it must experience less attenuation in the medium than the away side peak to contain the trigger. The attenuation of the away side jet can widen the peak and reduce to the away side yield where fewer particles meet the p_T threshold.

4.7.2 Analytical benefits of using an EMC trigger

The trigger selection is the first important stage of the analysis as the choice can have an impact on the selected events, the available statistics and corrections to the jet signal such as background subtraction. The 2007 $Au + Au$ at $\sqrt{s_{NN}} = 200$ GeV run was the first heavy ions experiment at STAR that benefitted from the fully installed EMC. Furthermore, as mentioned in section 4.5.1, a high momentum EMC triggered data set was taken from the 2007 run in order to identify γ-jet events. The data set will hereby be referred to as the *st-gamma* data set.

There are some unfortunate consequences of using tracks from the TPC for both trigger and associate particles. The STAR TPC is split into 12 segments at either end. Between each segment is a gap where no hits can be recorded. Referring to figure 4.16(a) the gaps result in a periodic depletion of tracks in the azimuthal plane. The depletion is present in both the trigger distribution and the associated distribution for track-track correlations. When the correlation is performed, the trigger distribution is convoluted across the associated distribution resulting in a $\Delta\phi$ distribution much like the one in figure 4.16(b).

In order to correct for the pad row spacing, the correlation must be scaled using a mixed event background that replicates the periodic track depletion [107]. By applying a correction to the correlation, the individual track information is lost and only the collective correlation remains. The current analysis requires the correlated tracks to retain their information for identification purposes therefore correcting the correlation in this manner is not an option. The EMC does have sector gaps, but does not have an efficiency that has a strong ϕ dependence. Therefore correlations that use an EMC trigger with TPC tracks do not produce a periodic undulation.

A second detector effect, created by performing track-track correlations, is a loss of signal close to the trigger vertex on the near side jet. Figure 4.17 is a two dimensional correlation that shows a reconstructed near side jet where the peak is situated at $(\Delta\phi, \Delta\eta) = 0$. A deficit is observed in the number of pairs found at the centre of the jet. This deficit is caused by the limited two track resolution of the TPC causing tracks to merge. Lower momentum associated tracks are curved more severely by the STAR magnet than the higher momentum trigger track. The tracks of particles produced very close to the trigger track can curve so that they cross the path of the trigger. When the two paths lie within the TPC two track resolution their respective pad row hits are merged into one signal. The signal is attributed to one of the tracks, which in the case of correlations is always the trigger track, leading to a gap in the path of the second track. If the

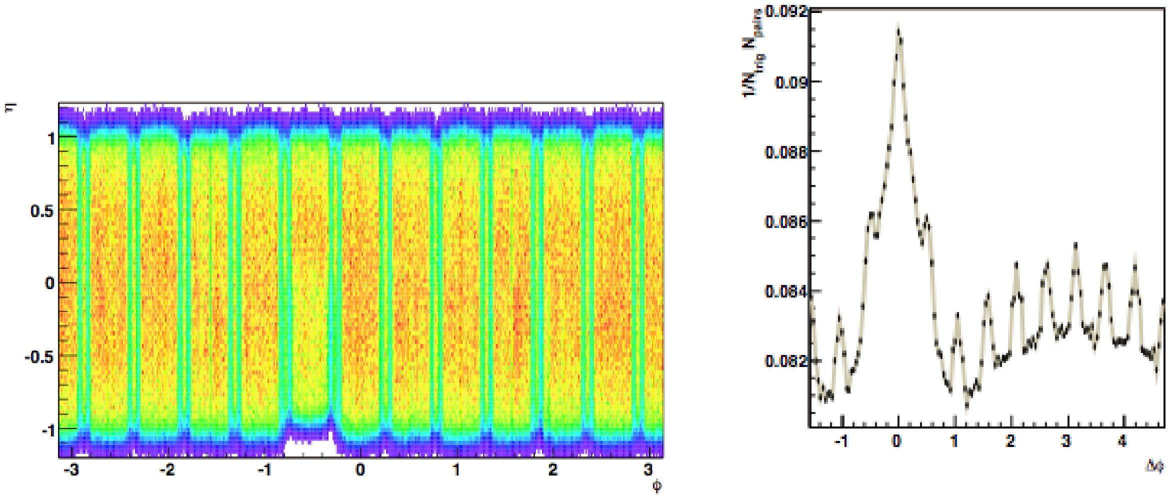

(a)

(b)

Figure 4.16: In (a) the $\phi\eta$ distribution of primary tracks taken from central $Au + Au$ data is shown. Colour indicates track density, increasing from blue to red. In (b) the $\Delta\phi$ projection of an uncorrected track-track correlation showing the TPC acceptance effect.

second track does not have enough hits to be reconstructed, or pass a good track selection, it is lost from the data. This problem is most evident when tracks have similar p_T and similar emission angle.

Significant effort has been made to produce an algorithm that corrects the track merging effect in two dimensional correlations [107]. Once again, a correction to the correlation results in the loss of individual track information therefore any algorithm developed for correcting track merging would not be suitable for this analysis. Using an neutral EMC trigger that does not produce a track in the TPC prevents track merging being identified near the trigger negating the need for a correction.

4.7.3 γ-jet event selection using EMC triggers

A γ-jet event is produced by the hard scattering of a gluon and a quark (Compton scattering), where $qg \to q\gamma$, or by quark anti-quark annihilation, where $q\bar{q} \to g\gamma$. In both cases the scattered non-photon component fragments to produce a jet. Section 4.4 described how the shower maximum detector might be used to distinguish between single photons, such as those produced in a γ-jet event, and dual photons from the $\pi^0 \to \gamma\gamma$ decay channel.

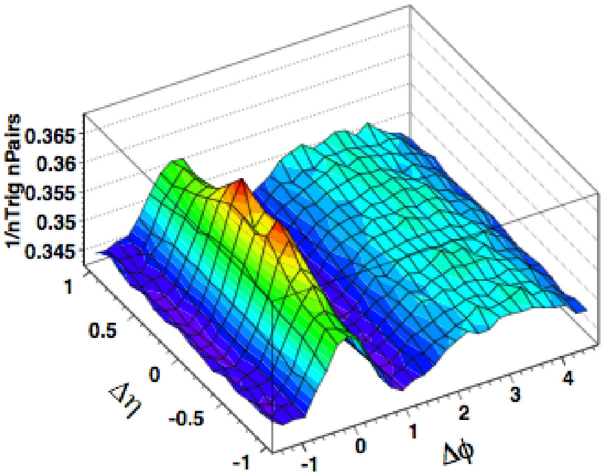

Figure 4.17: $\Delta\eta - \Delta\phi$ charged track correlation from central $Au + Au$ with a trigger p_T between 3-6 GeV/c and associated p_T between 1-2.5 GeV/c. The effect of track merging on two particle track-track correlations is observed as a deficit in the number of tracks close to $(\Delta\phi, \Delta\eta) = 0$.

The motivation for selecting γ-jet events is that photons do not interact as they escape the collision system and in section 2.1 it was revealed that direct photons are not suppressed by the medium created in heavy ion collision. In the transverse plane, the collective momentum of the jet must correspond to that of the direct photon. Therefore a γ-jet event would provide a reference momentum for jet attenuation measurements. Although the detecting of γ-jet events for jet attenuation studies is an exciting prospect, it is not the primary reason why they have been chosen as the trigger for this analysis.

A known issue with two particle correlations is that it introduces a jet surface emission bias when the trigger is a hadron [108]. The discussion in section 3.4.1, led to the conclusion that high p_T suppression is proportional to some order of the projectile's path length through the medium. Therefore, by selecting a high p_T trigger hadron, the trigger is bias toward hadrons that have shorter path lengths and are emitted closer to the surface. A study at high trigger and associated p_T did show that the suppression observed on the away side jet decreases as a function of associated p_T up to and above 6 GeV/c [31]. At high associated p_T, a large proportion of the selected events contain tangential jets where neither jet as a significantly long path through the medium. If it is implied that a shorter path length results in less modification, selecting hadron triggers could diminish the possibility of observing modifications to the jet spectra. By using γ-jet events, the than 20 issue is avoided as the photon trigger can be produced anywhere in the collision. The jets collected on the away side should exhibit a full range of path lengths, maximising the possibility of observing modification.

The associated p_T range for this analysis is between 2-6 GeV/c, which corresponds to the region where baryon enhancement is seen in central $Au + Au$. This is a respectively high choice for associated p_T as previous two particle jet studies have used predominantly low associated p_T below 2 GeV/c. By choosing a respectively large associated p_T, a degree of surface emission bias on the away side is inevitable. The away side surface emission can be minimised by increasing the trigger p_T threshold. A higher momentum trigger will increase the total energy of the jet resulting in an increased mean path length that allows an away side signal to be observed.

Chapter 5

EVENT SELECTION AND PARTICLE IDENTIFICATION

5.1 Introduction

Before continuing with the precise details of the particle identification technique a summary of both the physics goals and how best to achieve those goals will be presented. This analysis aims to identify how the hadron jet spectra are modified in the presence of a deconfined medium. In order to reconstruct the hadron jet spectra, there are certain considerations that must be addressed. The first task is to identify jets in heavy ion collisions that have not been fully quenched by their interaction with the medium. Once the jets are identified, the jet hadron spectra can then be extracted from the energy loss distribution of tracks associated with the jets. Finally the hadron spectra from jets in central $Au + Au$ collisions are compared to the spectra of jets that have suffered no medium interactions in order to explore the extent to which jets in central $Au + Au$ collisions have been modified.

Table 5.1 summarises the data sets used in this analysis. The analysis, which will be described in this chapter and the following chapter, was implemented for the 2007 $Au + Au$ data set for both central (reference multiplicity of 0-10%) and peripheral (reference multiplicity of 40-80%) collisions and the 2008 $d + Au$ data set. Both data sets had the same collision energy of 200 GeV per nucleon pair in the centre of mass. The data from the $Au + Au$ collisions were collected using the level two *st-gamma* trigger that used the STAR electromagnetic calorimeter to select events where an energy sum greater than 7.5 GeV was recorded between two adjacent towers with

Table 5.1: Data summary table for the four colliding systems used in this analysis: central *Au+Au*, peripheral *Au* + *Au*, d + Au and simulated $p + p$.

Data	Experiment	Trigger	Number of Events
2007 *st-gamma*	$Au + Au$ 0-10%	neutral particle $E_T > 6$ GeV	131,232
2007 *st-gamma*	$Au + Au$ 40-80%	neutral particle $E_T > 6$ GeV	54,640
2008 Minimum Bias	$d + Au$	neutral particle $E_T > 6$ GeV	163,516
2006 Pythia 6.4	$p + p$	π^0 $p_T > 6$ GeV	1,000,000

one tower recording greater than 5.5 GeV. The data from $d + Au$ collisions was collected using a minimum bias trigger.

The *st-gamma* data set originally consisted of just over one million events before any selection cuts were initiated. A cut on the primary vertex position, z, to be within 25 cm of the centre of the TPC detector reduced the number of events by roughly 40 %. The remaining reduction in events occurred after the reference multiplicity cuts, shown in section 5.3.1, and the trigger selection, which is detailed in the following section. The $d + Au$ minimum bias data set consisted of 46 million events. The vast reduction in statistics used for the current analysis was mainly due to the trigger cut selection.

5.2 Identified Neutral Triggers

The trigger parameters are the initial constraints that are implemented when extracting useful data from any given data set. The *st-gamma* data provide events that contain γ-jet candidates but does not retain any information of the actual trigger, such as position on the electromagnetic calorimeter. Ultimately the desired trigger particle will determine what information is needed from the electromagnetic calorimeter in order to identify the trigger. For this analysis, direct photons are the desired trigger. To identify direct photons, reconstructed particle showers (points) on the shower maximum detector are required. The point also contains the tower energy readout, or readouts in the case of a particle showering into multiple towers, which is required to identify the highest energy particle in the event.

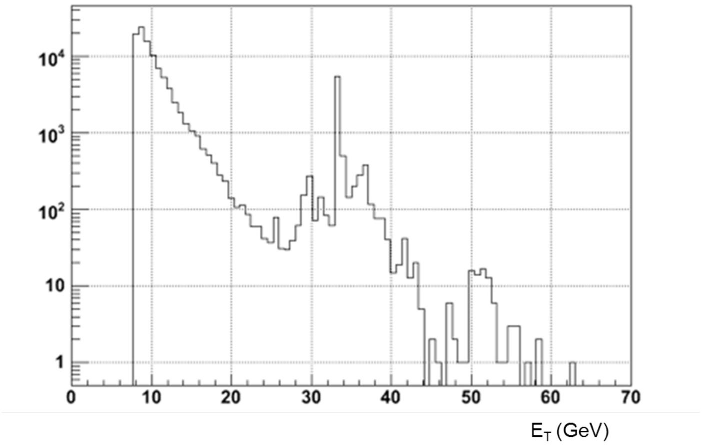

Figure 5.1: Tower E_T distribution taken from electromagnetic calorimeter triggers. A power law distribution is expected however large fluctuations are observed, above 20 GeV, that can be attributed to faults in individual towers

Once the events that pass the trigger energy threshold have been collected, a few quality control steps are necessary to verify that true neutral triggers have been detected. Firstly, at any given time during the actual experiment, there may have been portions of the electromagnetic calorimeter that were not functioning properly, which could be shower maximum detector strips, anode wires, towers or in extreme cases entire modules. It is important to identify any issues before a final data set is collected that will be used to perform the analysis.

Figure 5.1 is a typical tower energy distribution taken from the *st-gamma* data. The large fluctuations above 20 GeV can be removed by isolating towers that were not functioning properly at the time of data acquisition. There are several methods of identifying noisy towers, some are more effective than others. The method used for this analysis was to fit an exponential curve to each individual tower's energy spectra across the entire *st-gamma* data set. The χ^2 from the fit was then plotted for each tower. The χ^2 distribution should be flat for all but non functioning towers. Any tower where the χ^2 did not lie within errors to the fit of the χ^2 distribution was further investigated before removal by considering the number of hits and mean E_T. The final decision was made on a tower by tower basis determined by the author's own judgment.

From figure 5.2 there are clear differences between the spectra for functioning towers and non-functioning towers. With reference to the statistics legend in figures 5.2(a) and 5.2(b), it can be seen that the number of hits and the mean E_T vary significantly between a functioning tower an a

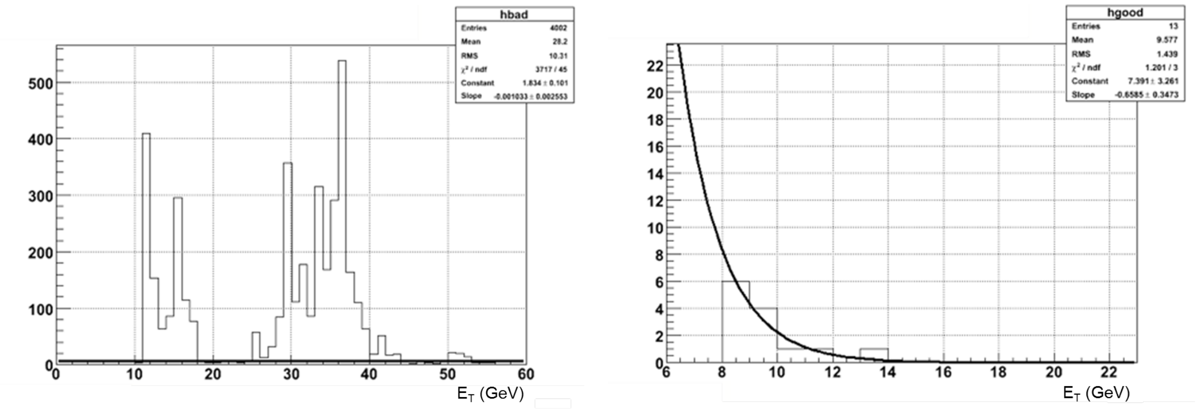

(a) An example bad tower.

(b) An example good tower

Figure 5.2: Identifying bad towers to eliminate false triggers. Bad towers usually have elevated hit numbers as well as higher χ^2 and mean terms.

non-functioning tower.

The final step to identifying that a neutral trigger has been detected is to perform a charged track veto on the candidate towers. From the track information, generated from TPC data, a position on the electromagnetic calorimeter can be calculated. From this position the corresponding tower can be identified and the track associated with an electromagnetic calorimeter tower. By excluding towers that have an associated TPC track, triggers that originated from charged particles can be eliminated from the trigger sample. However, simply eliminating towers with associated charged tracks can be too restrictive an approach especially in central $Au + Au$ events where the multiplicity is of the order of the number of calorimeter towers.

The aim of the charged track veto is to eliminate towers where most of the energy deposited was due to one or more charged particles. The charged track veto was therefore set at one third the total tower energy. For example a 6 GeV tower would be rejected if a track with p_T greater than 2 GeV/c was associated with that tower. Having performed the charged track veto, only a small proportion of events were lost. It was found whilst performing the $\frac{dE}{dx}$ analysis, which is covered in section 5.3, the vast majority of rejected towers were from high momentum electrons, most probably produced from the decay of D and B mesons.

5.2.1 Associated track selection

In the same way that trigger candidates must pass selection criteria, associated TPC tracks must also. The selection process is again physics goal determined but without over restricting the selection as to diminish available statistics beyond a useable quantity. The selected tracks are used in this analysis for three main purposes: to identify the jet or background signals, to identify the two particle correlation spectra and to veto charged triggers from the trigger selection process.

The p_T threshold for associated tracks was set at a minimum of 2 GeV/c and a maximum of 6 GeV/c. The tracks with p_T between 2-3 GeV/c have been included for the charged track veto and will not be used in the correlation as these tracks could not be identified using the $\frac{dE}{dx}$ method as the energy loss is too similar for each particle species. The resolution of the $\frac{dE}{dx}$ value assigned to each track is sensitive to the number of pad rows the track crosses in the TPC. Therefore setting a high threshold on the number of pad rows crossed by each track would be the most effective option to improve resolution.

Having disregarded the top 30% by energy of TPC cluster hits, due to the long ΔE tail at high ΔE of the hit energy distribution, the maximum number of available hits is limited to 30. Figure 5.3 shows how the distribution of hits used for $\frac{dE}{dx}$ is skewed towards the higher end of the scale. This is primarily caused by introducing a *good track* cut that only selects tracks that have registered greater than 20 hits in the TPC. There are some tracks that have used as few as 5 hits to calculate the track $\frac{dE}{dx}$. The reason for using so few tracks is because the $\frac{dE}{dx}$ algorithm only uses isolated charge clusters disregarding any hits that have merged clusters from one or more tracks.

During the initial investigations using $\frac{dE}{dx}$ to identify particles, no constraint was imposed on the number of hits used to calculate the track $\frac{dE}{dx}$ as the majority of tracks had high numbers of hits. However, as the identification method was developed it was discovered that by disregarding the less accurate tracks, which used fewer hits, the widths of the Gaussian distributions used to fit the $\frac{dE}{dx}$ data decreased and thus the resolution improved. The *good track* cut was then altered to include a threshold for the acceptable number of hits used for calculating $\frac{dE}{dx}$. The limit was eventually set at 20 hits as this did not hamper the statistics to the extent that fits were not able to be performed

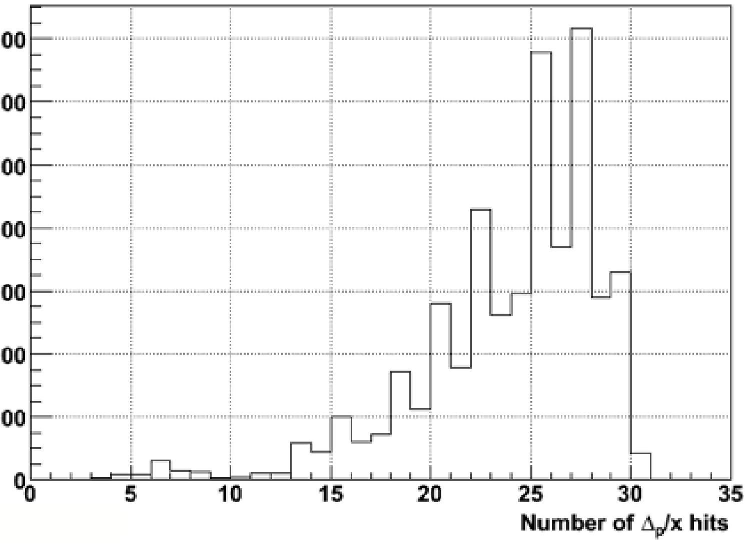

Figure 5.3: Number of TPC cluster hits used to calculate $\frac{dE}{dx}$. Only tracks that used greater than 20 cluster hits to calculate $\frac{dE}{dx}$ were selected to improve $\frac{dE}{dx}$ resolution without severely reducing statistics

but did show a significant improvement in resolution.

The geometrical constraints on the tracks limited the track selection to the mid-pseudorapidity range where the modulus of the pseudorapidity is less than 1. This selection was made as tracks beyond this pseudorapidity are unlikely to be attributed to jets triggered on the barrel electromagnetic calorimeter thus reducing the background created from trigger non associated particle pairs.

As table 5.1 indicates, the $d + Au$ data set and $Au + Au$ data sets should be statistically similar. Figure 5.4 shows how the number of tracks in the $d + Au$ data set is more than three times the number in central $Au + Au$ at p_T below 3.5 GeV/c yet is almost an order of magnitude higher above 5 GeV/c. The major factor contributing to this difference is the suppression of high p_T particles in central $Au + Au$.

5.3 Energy Loss Particle Identification for Jets

In section 4.6.1 the ability to identify particles with the TPC was discussed using particle energy loss data. The remainder of this chapter will outline the steps that were taken to develop the particle identification method used in this analysis.

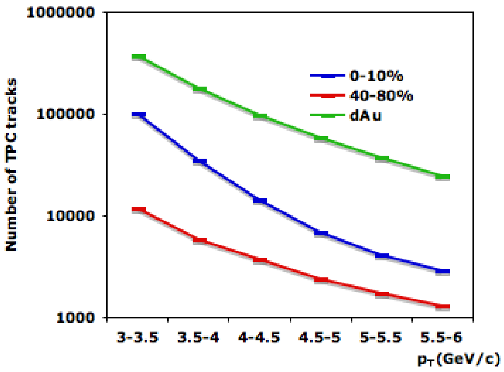

Figure 5.4: Number of tracks in each p_T bin for central and peripheral Au + Au collisions and d + Au collisions at $\sqrt{s_{NN}}$ = 200 GeV. The increased number of tracks in the d + Au data cannot be completely attributed to a larger number of events collected and high p_T suppression. A further trigger bias can also be considered as there is no π^0 suppression.

In the previous chapter the two particle correlation method was discussed as the chosen tool for jet finding. The correlation will identify three regions in $\Delta\phi$ that correspond to the trigger jet, the away side jet and the background where no jet signal is observed. Once these regions have been identified, the $\frac{dE}{dx}$ distributions can be obtained for each region separately. Treating each region separately does slightly complicate extracting accurate particle yields. The first issue is that two particle correlations do not produce a pure jet sample but create a jet signal on top of a background built up from the underlying event. This background will have to be subtracted in order to produce accurate jet spectra. The correlation does not preserve individual track information therefore the subtraction must be performed after the $\frac{dE}{dx}$ data has been analysed. In order to overcome this issue, the $\frac{dE}{dx}$ data for the background part of the correlation can be used to achieve accurate hadron ratios for the background within the jet regions assuming that the background has a uniform hadron composition across all $\Delta\phi$.

The second obstacle is identifying charged kaons. In previous particle identification studies at STAR, the kaons were constrained using K^0_S spectra [109]. In order to obtain the K^0_S yields within each p_T range, a separate correlation would need to be performed between the gamma trigger and K^0_S candidates in order to establish the jet profile for K^0_S that could then be split into the three regions in $\Delta\phi$. Strange hadrons have been used in two particle correlations where the strange hadron has been used as the trigger [110]. There has also been a study to ascertain the Λ/K^0_S ratio in jets at low p_T[111]. Yet inclusive strange hadron spectra are usually limited to the intermediate

p_T region below p_T = 5 GeV/c [112]. In this analysis it was found that there were insufficient statistics within the p_T region 3-6 GeV/c to produced two particle correlations with K_S^0. Therefore the charged kaons will need to be identified as part of the fit to the $\frac{dE}{dx}$ data.

5.3.1 Calibrating the energy loss data

Before the $\frac{dE}{dx}$ data could be calibrated for the 2007 $Au + Au$ run, the data had to be separated into central events and peripheral events. The centrality definitions for this analysis were taken from the 2004 $Au + Au$ minimum bias data [107]. The exact reference multiplicity, the number of tracks with pseudo-rapidity $|\eta|$ less than 0.5, that corresponds to the different centrality percentiles differs with each trigger, as each trigger may have a bias towards a particular centrality. For example, the *st-gamma* dataset, which is designed to trigger on jets, is likely to be bias toward central events where the number of binary collisions is higher. The bias towards central events can be seen in figure 5.5 where, unlike in the minimum bias data seen in figure 4.6, the reference multiplicity distribution is skewed towards the more central events. In fact, the accepted central/peripheral event ratio is ≈ 2.5, which may result in the analysis of peripheral events being limited to lower p_T than central events due to statistics. There is the possibility of increasing the reference multiplicity range for peripheral events however this is likely to dilute any hadron ratio differences between central and peripheral as the peripheral events selection will contain higher multiplicity events.

A fit to the $\frac{dE}{dx}$ data is performed using the Bichsel predictions as the mean values of an eight Gaussian fit (proton, kaon, electron and pion both negative and positive). The preliminary fit function consists of seventeen parameters of which six are fixed. The fixed parameters are the separations between the electron mean $\frac{dE}{dx}$ and those corresponding to the mean of each other particle as set by the Bichsel predictions. The remaining eleven parameters are the electron and positron peak positions, the peaks' width, σ, the π^+ and π^- yields, the p/π^+ and $\bar{p}/\pi^-$ ratios, the e^+/π^+ and e^-/π^- ratios, and the K^+/π^+ and K^-/π^- ratios. This fit will serve as the benchmark to gauge future alterations to the fit function.

The use of the electron $\frac{dE}{dx}$ peak position to calibrate the $\frac{dE}{dx}$ data has been used before in STAR

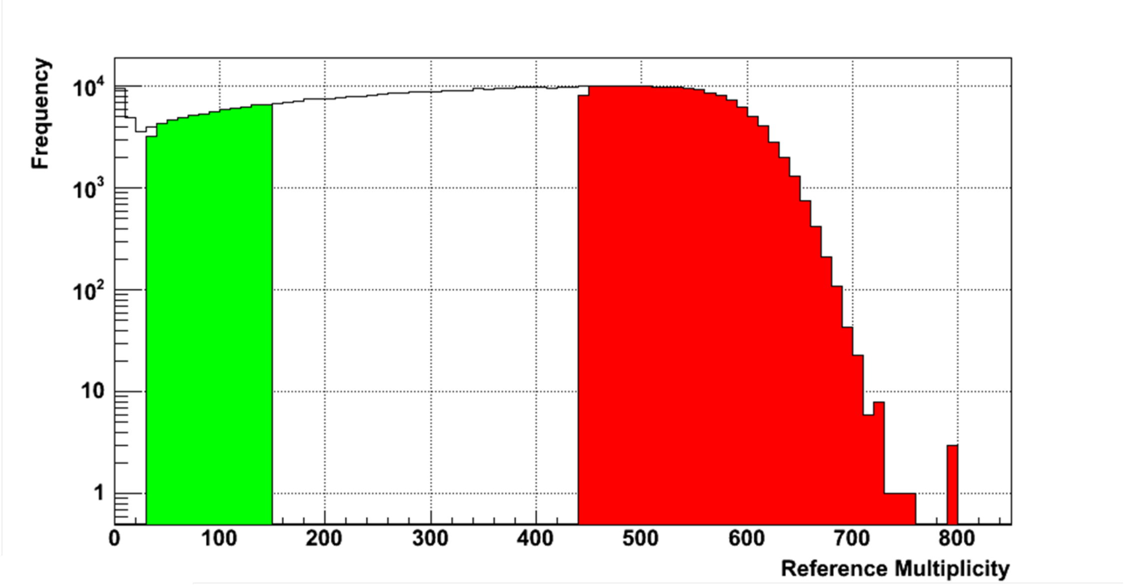

Figure 5.5: Reference multiplicity distribution for *st-gamma* data. The green region corresponds to the 40-80% centrality definition from 2004 $Au + Au$ minimum bias data, while the red region corresponds to 0-10%.

[109]. A sample of charged triggers, earlier eliminated from the data by the neutral trigger selection, was added to the data. The motivation behind this strategy is that it should allow an electron peak to emerge to the right of the pion peak that can be used to calibrate the other particle peak positions.

It is important not to lose sight of the physics when adjusting the fit function as too much freedom may result in a better fit but not portray the true particle contributions. A few simple physics checks can be performed after each fit cycle. Firstly, there should not be an excess of anti-matter over matter, thus $p/\bar{p} \geq 1$, $K^+/K^- \geq 1$. As charged pions are either $u\bar{d}$ (π^+) or $d\bar{u}$ (π^-) there may be a slight preference for negative pion production as the colliding nuclei contain fewer protons (uud) than neutrons (udd). Therefore it is expect that the π^+/π^- ratio is consistent or less than unity.

5.3.2 Calibrating the energy loss data from peripheral $Au + Au$ collisions

Although the peripheral data contain fewer statistics than the central collisions, due to the smaller system size, the data are fit friendly. This is to say that the shape of the $\frac{dE}{dx}$ distribution represents

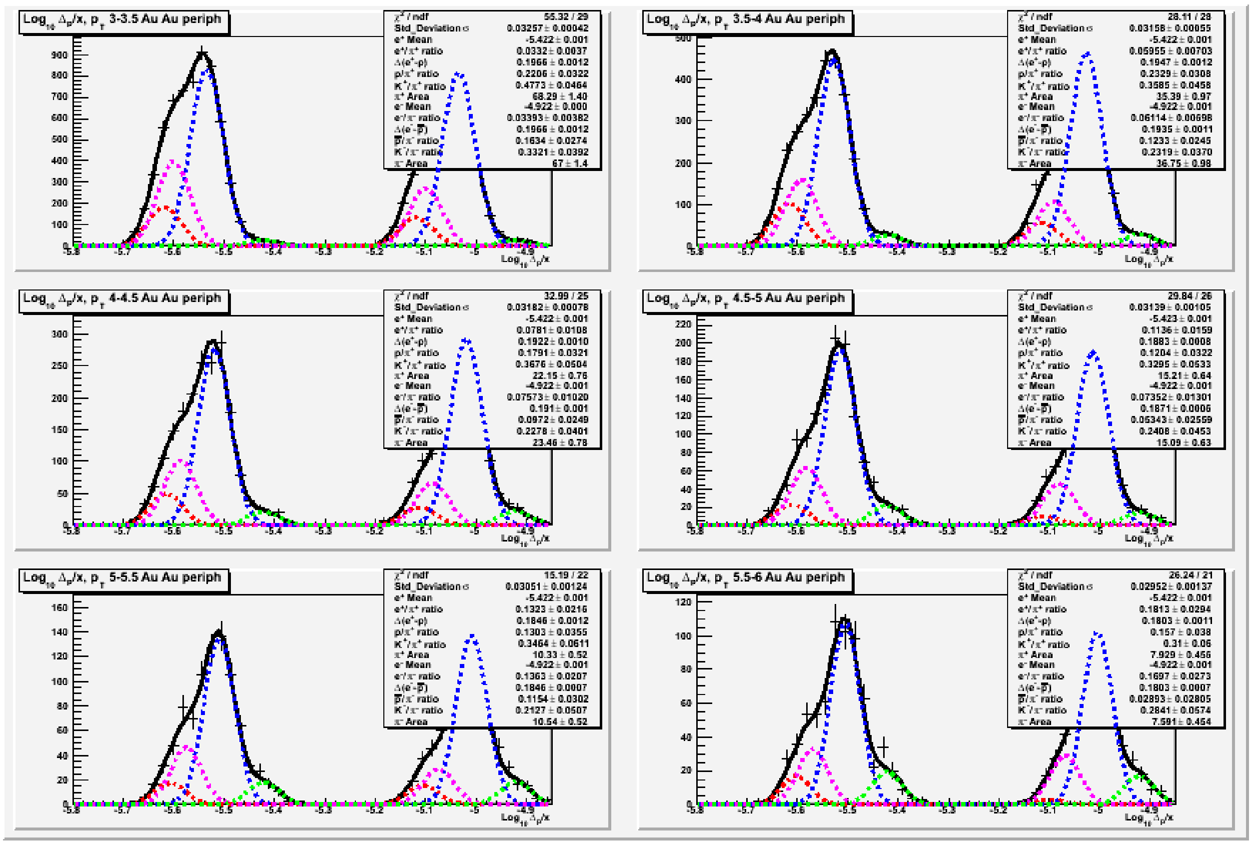

Figure 5.6: Fit, consisting of eight Gaussians, to $\frac{dE}{dx}$ data from peripheral $Au + Au$ collisions, using calibrated particle $\frac{dE}{dx}$ peak positions determined by the Bichsel prediction. The proton peaks are in red, the pion peaks in blue, the kaon peaks in pink and the electron peaks in green.

more closely a peak (pions) with two shoulders (protons/kaons and electrons), which allows the fit function to describe accurately the data using Gaussians. At higher p_T intervals the jet contribution accounts for a greater proportion of the particle spectra therefore the number of tracks becomes more dependent on the number of selected events instead of the centrality of the collision. Figure 5.4 illustrates how the number of tracks depends on p_T for the two different system sizes. It is clear to see that the difference in statistics between central and peripheral collisions diminishes as p_T increases.

Figure 5.6 shows the fit to peripheral $Au + Au$ $\frac{dE}{dx}$ data using the Bichsel function predictions for the different particles. The $\frac{dE}{dx}$ data has been split in to p_T bins of 0.5 GeV/c in the range 3-6 GeV/c. The mean momentum of the tracks in each p_T bin was used to acquire the corresponding Bichsel prediction for each hadron species. The positive and negative tracks have been arbitrarily separated by displacing the negative tracks by 0.5 to the right of the positive tracks.

Table 5.2: Fit to energy loss data statistics table from peripheral $Au + Au$ collisions.

p_T Range	χ^2	p/π^+	$\bar{p}/\pi^-$	K^+/π^+	K^-/π^-	π^+/π^-
3-3.5	1.91	0.22 ± 0.03	0.16 ± 0.03	0.48 ± 0.05	0.33 ± 0.04	1.02 ± 0.02
3.5-4	1.00	0.23 ± 0.03	0.12 ± 0.02	0.36 ± 0.05	0.23 ± 0.04	0.96 ± 0.03
4-4.5	1.32	0.18 ± 0.03	0.10 ± 0.02	0.37 ± 0.05	0.23 ± 0.04	0.94 ± 0.03
4.5-5	1.15	0.12 ± 0.03	0.05 ± 0.02	0.33 ± 0.05	0.24 ± 0.05	1.01 ± 0.04
5-5.5	0.69	0.13 ± 0.04	0.12 ± 0.03	0.35 ± 0.06	0.21 ± 0.05	0.98 ± 0.05
5.5-6	1.25	0.17 ± 0.04	0.03 ± 0.02	0.31 ± 0.06	0.28 ± 0.06	1.04 ± 0.06

The fit has proved successful and all eight particles have been found to contribute to the total $\frac{dE}{dx}$ distribution as would be expected. Furthermore the simple physics checks suggested in section 5.3.1 have been achieved by the fit as shown in table 5.2. The conclusion is that the Bichsel predictions do accurately describe the peripheral $Au + Au$ data, based purely on the results shown in figure 5.6, as the electron peak has not displaced, within errors, from the original position set by the Bichsel prediction in all p_T bins.

5.3.3 Calibrating the energy loss data from central $Au + Au$ collisions

The fits in figure 5.7 use the electron calibration method, described in the previous section, and do tend to fit the data very well. All of the physics tests are matched save for an exception in p_T bin 4-4.5 GeV/c where the $p/\bar{p}$ ratio is less than unity.

The electron calibrated $\frac{dE}{dx}$ curve is shown in figure 5.8 and is consistent with a momentum independent shift from the Bichsel prediction. As the right hand side of the $\frac{dE}{dx}$ distribution in figure 5.7 appears to be accurately described by the current pion and electron positions, it is concluded that the pion peak is correctly calibrated using the electron calibration method.

A pure sample of charged pions would be accessible from the decay of $K_S^0 \rightarrow \pi^+\pi^-$. Yet with the current statistics, it is not possible to produce meaningful K_S^0 invariant mass peaks up to a p_T of 12 GeV/c, which would be required to obtain a sample of charged pions with a p_T of 6 GeV/c. In the final version of the fit function, the pion peak position will be allowed the flexibility of a 1σ deviation from the Bichsel $e - \pi$ separation to account for any possible shift from the predicted

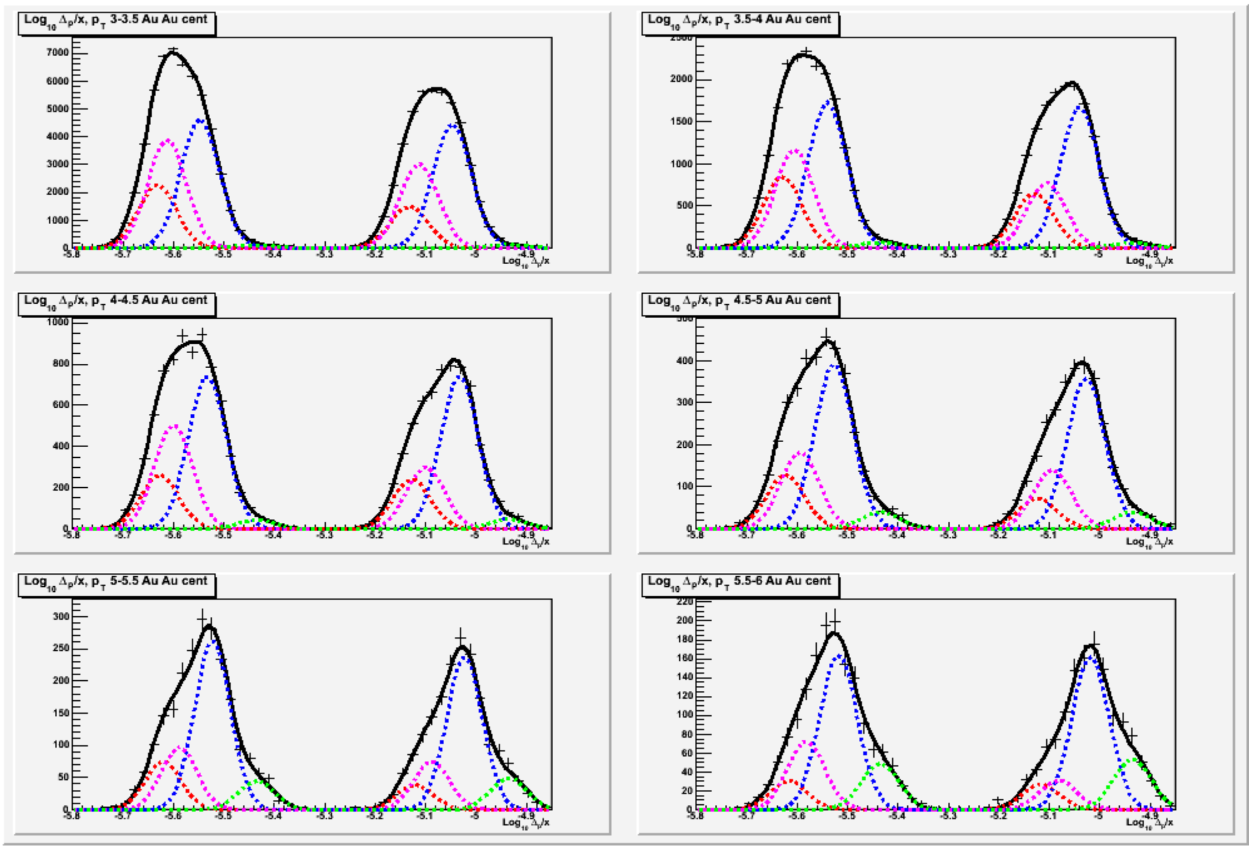

Figure 5.7: Fit to $\frac{dE}{dx}$ data from central Au + Au collisions, using the calibrated electron $\frac{dE}{dx}$ curve and the Bichsel function spacings.

$e - \pi$ separation.

The kaon peak is dominating the left hand side where the proton peak is expected to dominate due to baryon enhancement. In order to calibrate the proton peak, the Λ daughter proton candidates were fit using a function that has a fixed pion peak position, where the peak position is taken from figure 5.7, a free peak width and a free proton peak position that is initially set at the Bichsel predicted value.

The results of the fit are shown in figure 5.9. The left hand panel of figure 5.10 compares the $p - \pi$ peak separation according to the Bichsel function with the separation resulting from the Λ daughter fit. The right hand panel that shows by what value in $\frac{dE}{dx}$ has the pion to proton separation deviated from the prediction provided by the Bichsel function. The deviation can be described using a momentum independent constant, which simplifies describing the proton $\frac{dE}{dx}$ peak position. This result indicates that the $p - \pi$ peak separation in central Au + Au is smaller than that expected from the Bichsel prediction, which is in contrast to what was found in peripheral Au + Au.

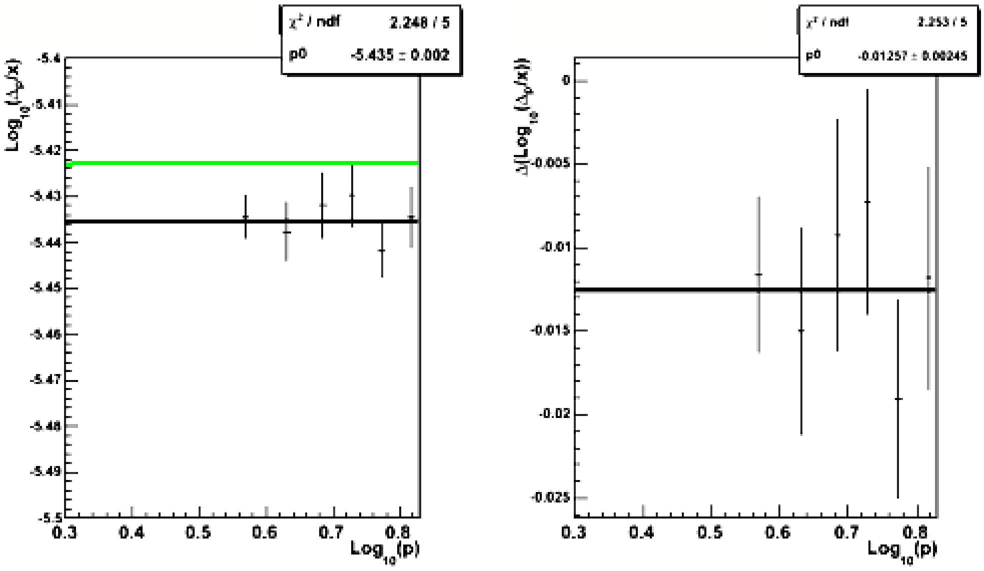

Figure 5.8: Fit to calibrated electron $\frac{dE}{dx}$ data from central $Au + Au$ collisions. The left figure shows how the calibrated electron $\frac{dE}{dx}$ curve (black) compares to the Bichsel curve (green). The right figure is the difference between the calibrated electron points and the Bichsel prediction.

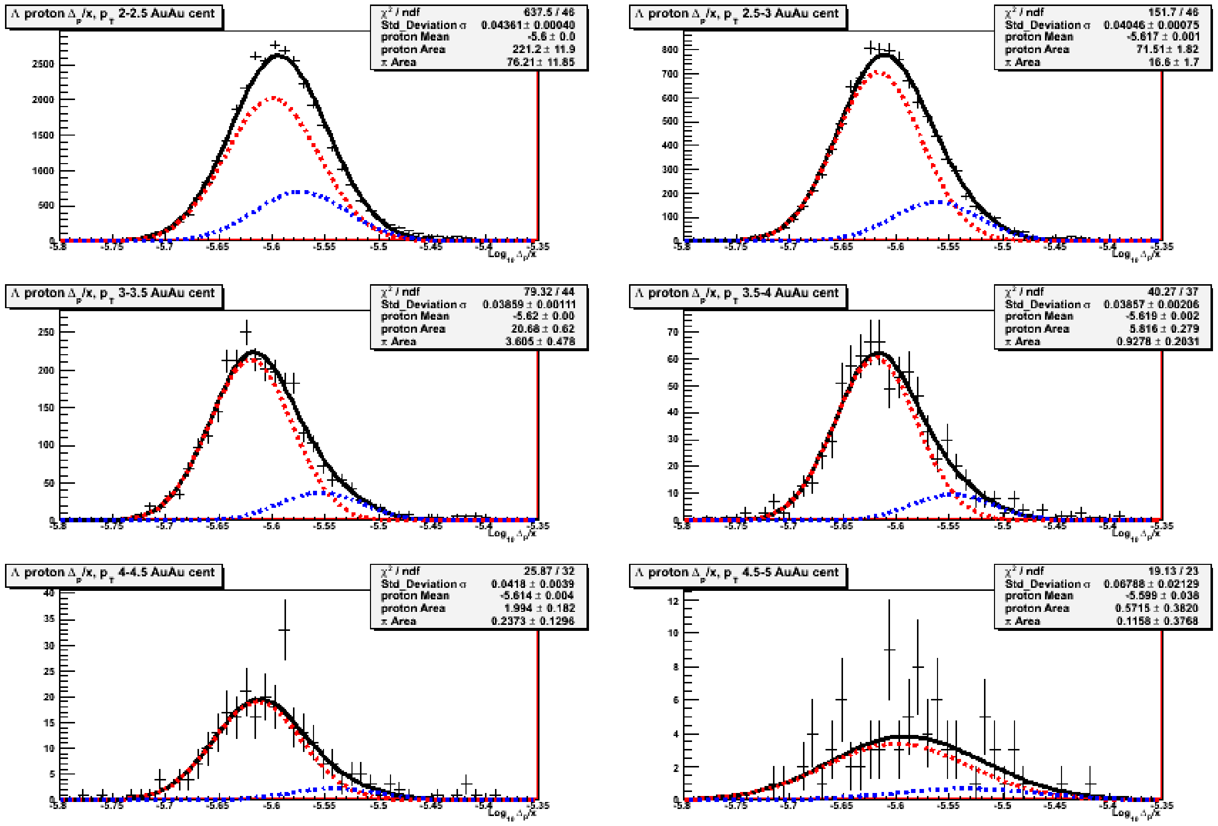

Figure 5.9: Fit to Λ proton daughters $\frac{dE}{dx}$ data from central $Au + Au$ collisions. Two Gaussian fit consisted of six parameters of which five were free parameters. The mean of each Gaussian was set according to the Bichsel prediction calibrated by the electron deviation. Only the pion mean was fixed to these values while the proton mean as a free parameter.

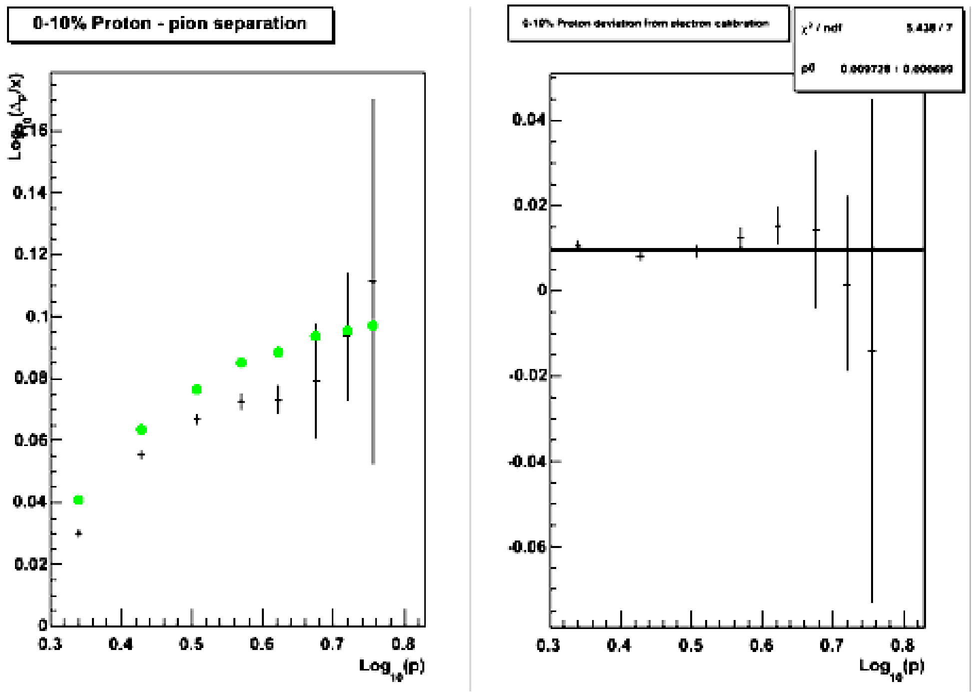

Figure 5.10: Results of a fit to the $\frac{dE}{dx}$ data of Λ daughter proton candidates where the proton peak position was a free parameter and the pion peak position was fixed according to the electron calibration. The left panel compares the Bichsel predicted pion to proton separation in $\frac{dE}{dx}$ (green points) to the separation produced as a result of the fit. The right figure is the deviation from the Bichsel separation exhibited by the proton peak position.

5.3.4 Kaon Contribution Constraints

Previous studies have used the yield of K_s^0 mesons to limit the kaon contribution [109]. An alternative method was developed during and after the work presented in this thesis that used the deviation of the proton, pion and electron from the Bichsel positions to calculate the most likely kaon position [113]. The method used in this analysis estimated that the kaon deviation from the Bichsel prediction would be between that of the electron deviation and the proton deviation, including the error associated with each deviation. Therefore, the kaon peak position was set as the average deviation with the upper limit set as the proton deviation and the lower limit set as the electron deviation. The electron and proton peak positions are bound by a 1σ deviation in the final fit function. Larger deviations, 2σ, or 3σ, allowed too much freedom in the fit and could not produce realistic results that accounted for all four particle species.

The fit performed in figure 5.11 has managed to fit the $\frac{dE}{dx}$ data quite well using calibrated proton and electron peak positions. The individual deviations from the Bichsel predictions are shown

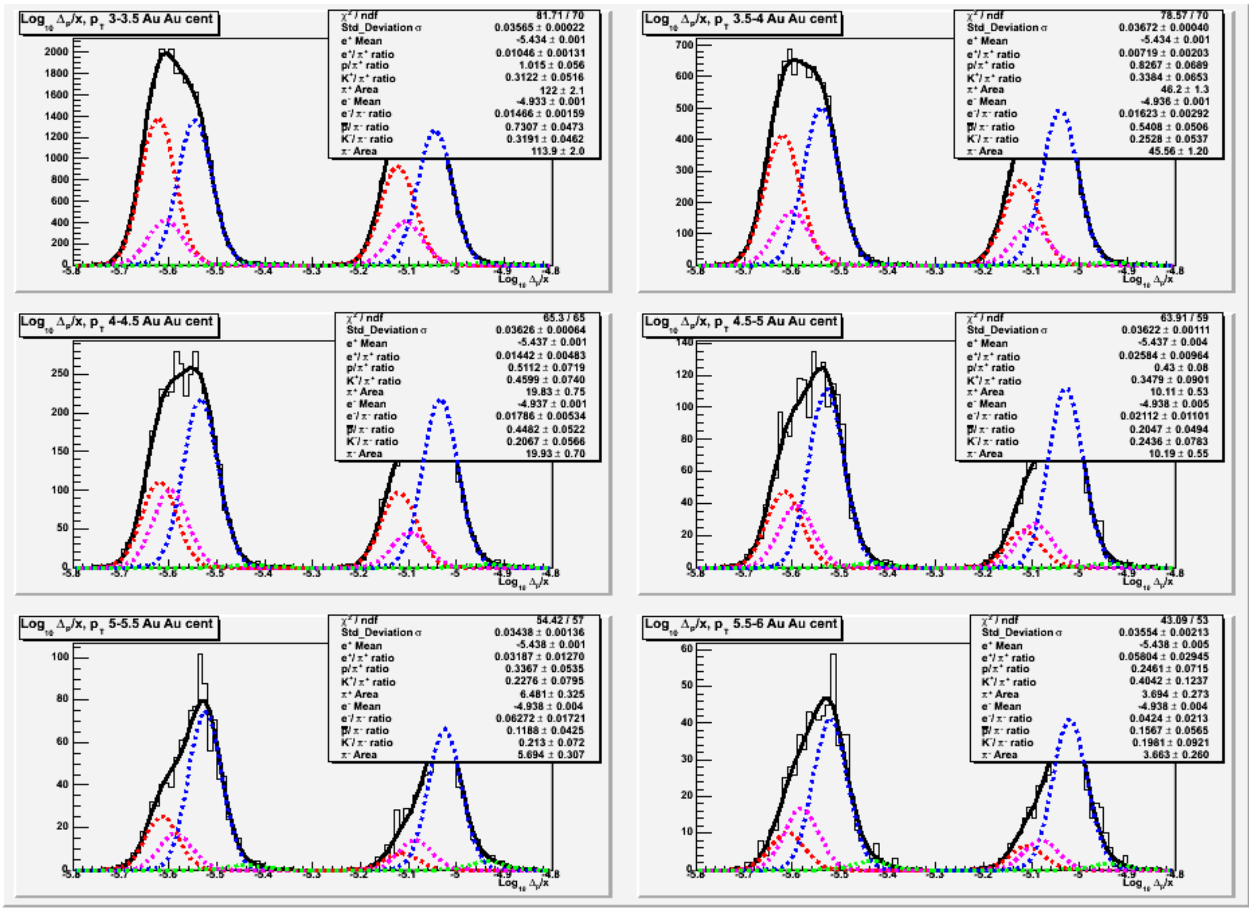

Figure 5.11: Fit, consisting of eight Gaussians, to $\frac{dE}{dx}$ data from central $Au + Au$ collisions, using calibrated proton and electron $\frac{dE}{dx}$ peak deviations from the Bichsel prediction and a constrained kaon peak position.

in figure 5.12 where the electron deviation is shown in 5.12(a), the pion deviation is 5.12(b), the proton deviation is 5.12(c) and the kaon deviation is 5.12(d). It is also plausible that a flat line could also describe the proton and pion data, therefore a p_T independent shift will be used to set the peak positions. The peak positions will be allowed to vary within a deviation of 1σ when the fit is performed on the correlated data, where the correlation is separated into near side jet, away side jet and background in $\Delta\phi$.

5.3.5 Calibrating the $d + Au$ $\frac{dE}{dx}$ data

The $d + Au$ $\frac{dE}{dx}$ data was calibrated using the same method as the peripheral $Au + Au$ data. As was found with the peripheral $Au + Au$ data, the Bichsel predictions accurately predicted the peak positions for all the particle species. The fit shown in figure 5.13 supports the conclusion that,

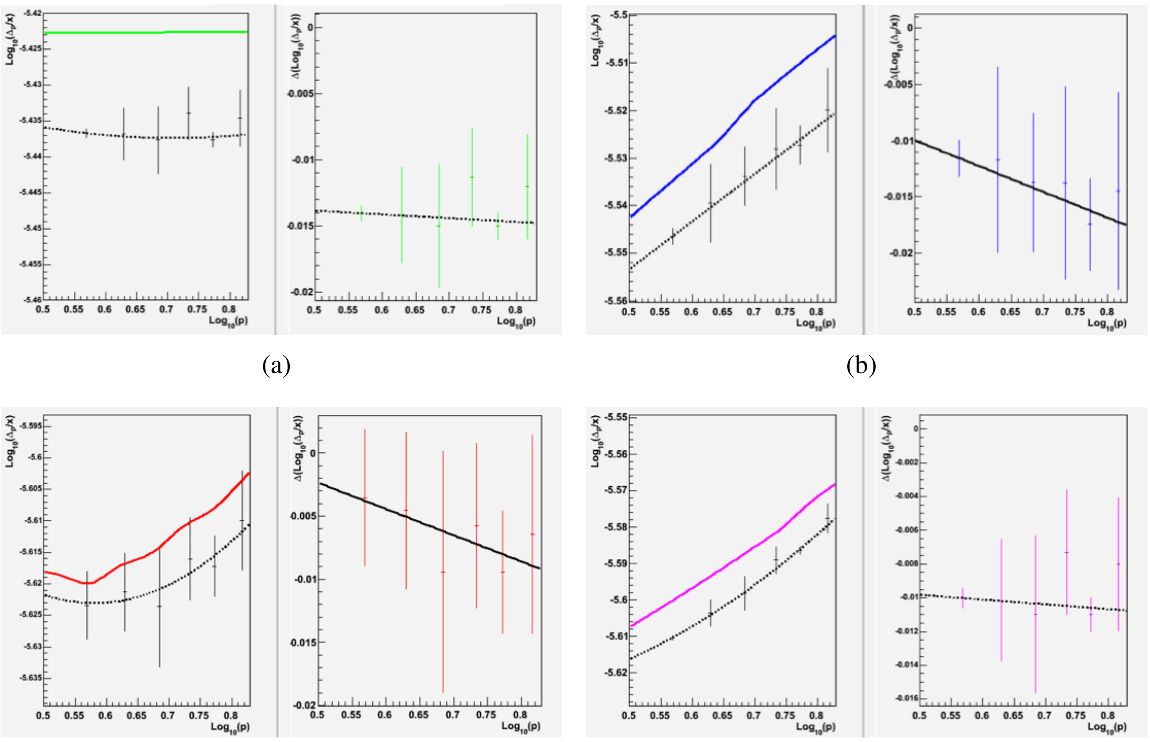

(a) (b)

(c) (d)

Figure 5.12: Peak position of particle species after implementing the electron deviation from the Bichsel prediction, the proton deviation, and constraining the kaon peak position between the electron and proton deviations. In green are the $e^{\pm}$ deviations, blue the $\pi^{\pm}$ deviations, red the $p^{\pm}$ deviations and pink the $K^{\pm}$ deviations.

as was found with the peripheral $Au + Au$ data, all particle species are aligned with the Bichsel predictions.

5.3.6 Inclusive charged hadron ratios

The central and peripheral $Au + Au$ inclusive hadron ratios of $p/\bar{p}$, K^+/K^- and π^+/π^- have been calculated in figure 5.14 for p_T 3-6 GeV/c independent of the two particle correlation. The two figures show the ratios for central and peripheral collisions from top to bottom respectively. The pion trend is the most precise due to greater statistics and less overlapping of the pion $\frac{dE}{dx}$ range with the ranges of other hadrons. The π^+/π^- ratio is consistent with unity, which provides a consistency check for the pion yields extracted from the $\frac{dE}{dx}$ fit. The K^+/K^- ratio, with the exception with the first bin of the central data, is greater or consistent with unity. In all p_t bins, $p/\bar{p}$ ratio is also greater or consistent with unity however there is far larger uncertainty. The

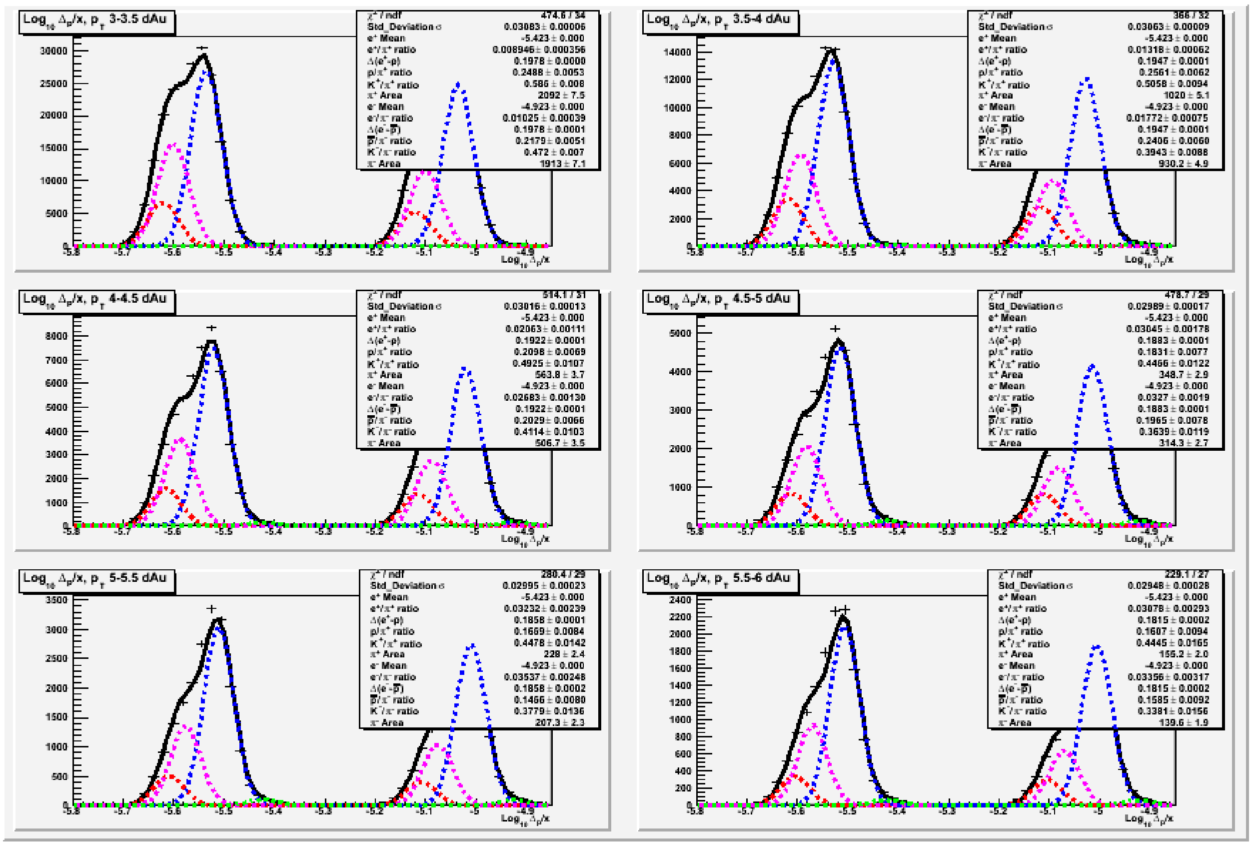

Figure 5.13: Fit, consisting of eight Gaussians, to $\frac{dE}{dx}$ data from $d + Au$ collisions, using the Bichsel predictions to fix the peak positions of all particle species.

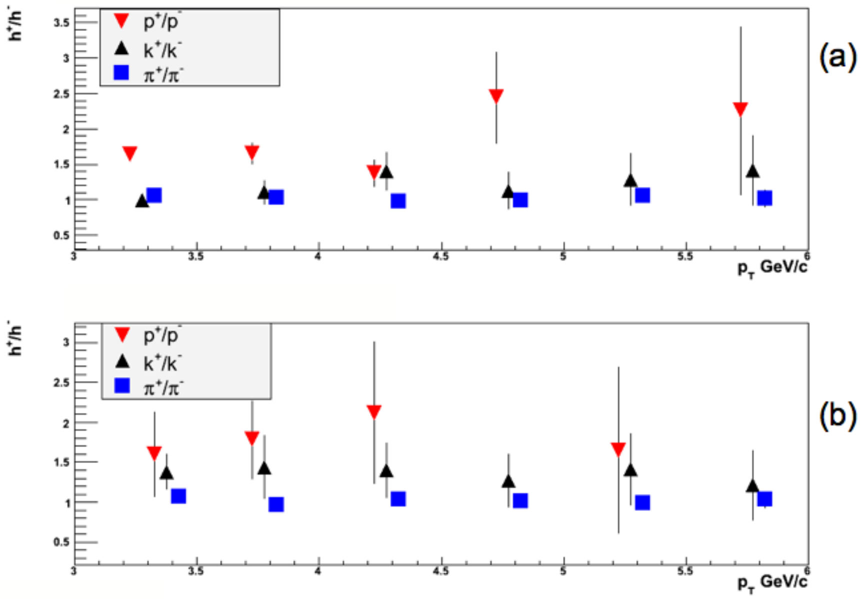

Figure 5.14: Inclusive h^+/h^- hadron ratios $Au + Au$. Figure (a) shows the hadron ratios from central $Au + Au$ collisions while figure (b) shows the hadron ratios from peripheral $Au + Au$ collisions. Missing data points are caused due to the marker value not being on the graph scale even though the error bars would be present.

missing points, 5th bin in central collisions and 4th and 6th bins in peripheral collisions, are all above the scale of the plot with large errors consistent with unity. These points are missing due to poor statistics hampering the quality of the fit. For this reason, positive and negative particles will be combined in the correlation analysis.

As with the $Au + Au$ data, the hadron ratios of $p/\bar{p}$, K^+/K^- and π^+/π^- have been calculated for $d+ Au$ events and are shown in figure 5.15. The errors are smaller than those seen in the $Au + Au$ data as the $d + Au$ data set is statistically stronger than the central or peripheral data sets, shown in figure 5.4, and contain $\frac{dE}{dx}$ distributions dominated by pions that are easier to fit. The inclusive ratios for all three hadrons appear to be p_T independent. However there is a suggestion that the $p/\bar{p}$ ratio is larger above 5 GeV/c yet the large errors are consistent with the other data points.

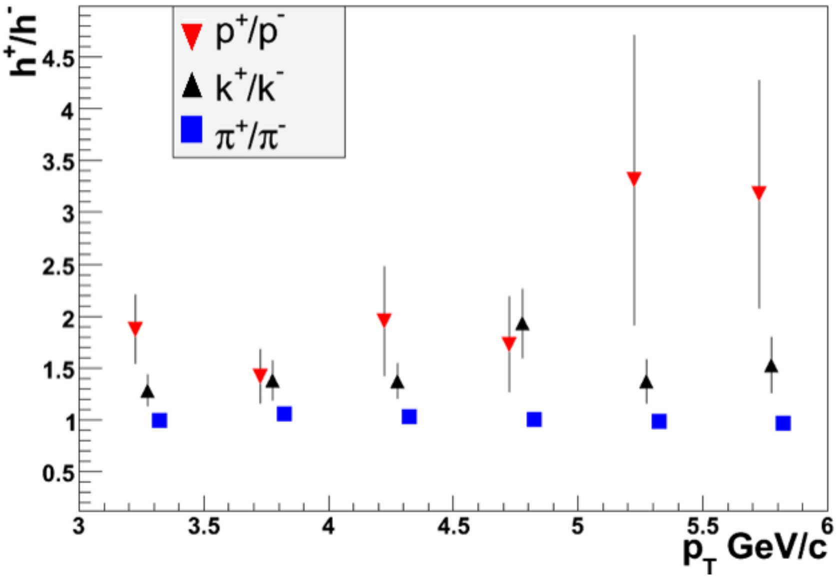

Figure 5.15: Inclusive h^+/h^- hadron ratios $d + Au$. The inclusive ratios are calculated for p_T from 3 to 6 GeV/c.

Chapter 6

ANALYSIS

This chapter is set out in four parts. The first part consists of a description of the background subtraction method followed by the two particle correlations for unidentified neutral triggers with unidentified charged tracks from all three data sets. The second part includes the analysis of the identified charged tracks, using the $\frac{dE}{dx}$ analysis method, for three regions (near side jet, away side jet and background) in azimuth. The ratio of hadron species with respect to charged pions was calculated and compared for the three regions.

The third part of this chapter looks at identified neutral trigger events in central $Au + Au$. The correlations were made using only events that satisfy the single photon trigger criteria using the barrel electromagnetic calorimeter shower maximum detector data. The single photon trigger should minimise the $\pi^0 \rightarrow \gamma\gamma$ contamination of the γ-jet event selection. The hadron ratios from identified neutral trigger central events will then be compared with the hadron ratios from peripheral $Au + Au$ and $d + Au$ unidentified neutral trigger events.

The final part of this chapter compares the hadron ratio results from all data sets with hadron ratios taken from Monte Carlo generated $p + p$ events. The $p + p$ events selected used π^0 triggers with a p_T greater than 6 GeV/c within the mid-rapidity range of the STAR barrel electromagnetic calorimeter.

6.1 Extracting particle jet yields from energy loss data using two particle correlations

In section 4.7.1, the correlation signal was described as consisting of a dijet signal and a background produced from correlations that include particles created in the underlying event, which are not associated with the dijet. In the previous chapter, the method of identifying the species of the charged particles in the event was described.

By combining the two methods, the particle yields can be determined for both jets and background as a function of p_T. The yield due to the uncorrelated background will need to be subtracted in order to obtain the jet yield. This will allow a comparison of the p_T spectra of $p^{\pm}$, $\pi^{\pm}$ and $K^{\pm}$ from jets and the underlying event, as well as particle ratios as a function of p_T.

6.1.1 Background subtraction

In order to determine the p_T spectrum of $p^{\pm}$, $\pi^{\pm}$ and $K^{\pm}$ correlated with jets, the yields, as a function of p_T, need to be extracted. To establish the background p_T spectrum, a pure background source must be collected and the $\frac{dE}{dx}$ data analysed.

Fortunately this is not a difficult task due to the nature of the data in the correlation. Both the trigger p_T ($>$ 6 GeV/c) and the associated track p_T (3-6 GeV/c) are relatively high for jet studies performed at STAR using two particle correlations. The correlations performed in this analysis produced tall narrow jet peaks that can easily be distinguished from the background that lies between the jet peaks in $\Delta\phi$.

To identify the background regions, a fit was performed to the two particle correlations that contained a background and jet contribution. The fit function was then separated into three separate functions where the jet contributions were separated from the background contribution.

A simple algorithm was implemented that returned the values where the jet and background functions crossed. These cross over points were classified as the jet-background boundaries. The

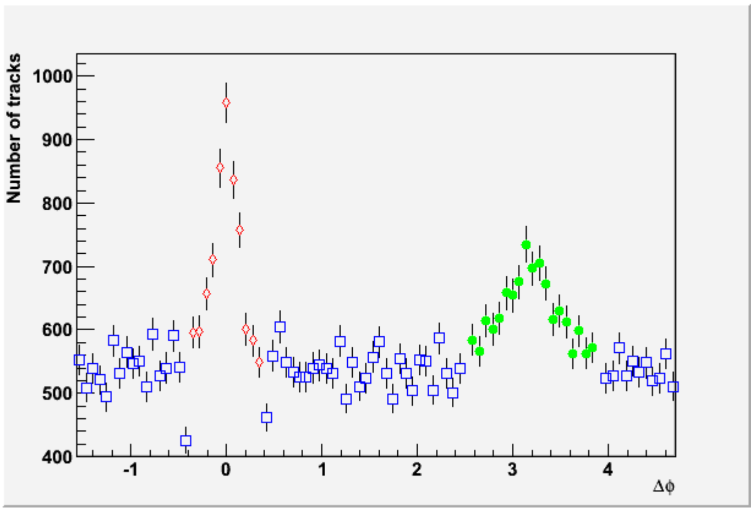

Figure 6.1: Two particle $\Delta\phi$ correlation with triggered EMC towers with $E_T > 6$ GeV and associated charged tracks with $3.0 < p_T < 3.5$ GeV/c using central $Au + Au$ data at $\sqrt{s_{NN}} = 200$ GeV .

boundaries essentially determined the jet width in $\Delta\phi$.

In figure 6.1, an example correlation is shown that has been performed using central $Au + Au$ data at $\sqrt{s_{NN}} = 200$ GeV with a BEMC tower trigger threshold of $E_T > 6$ GeV and an associated track p_T between 3.0 and 3.5 GeV/c. The distribution has been separated into the dijet signal (red and green) and the background (blue). What was discovered during this analysis is that, for the *st-gamma* data set at the very least, the anisotropic flow, v_2, contribution to the background is negligible. A flow contribution to the background only exists if both the trigger and associated particles are not from jets. With a jet trigger E_T threshold of 6 GeV, the majority of trigger particles appear to be from true jet events. Therefore the background consists mainly of tracks uncorrelated with the trigger (either a leading π^0 or direct photon). The background can therefore be treated as uniform in $\Delta\phi$, which allows for a more simple approach to the background subtraction.

By identifying the background regions away from the jet peaks, the background subtraction method also assumes that the background population is uniform in $\Delta\phi$. Once the spectra of the background regions has been established, using the $\frac{dE}{dx}$ data in the designated $\Delta\phi$ background regions, the track density (number of tracks per radian) can be used to assign the quantity of each particle that resides in the background below the jet peak. The two particle correlations have been separated into different regions as shown schematically in figure 6.2. The objective of the subtraction is to

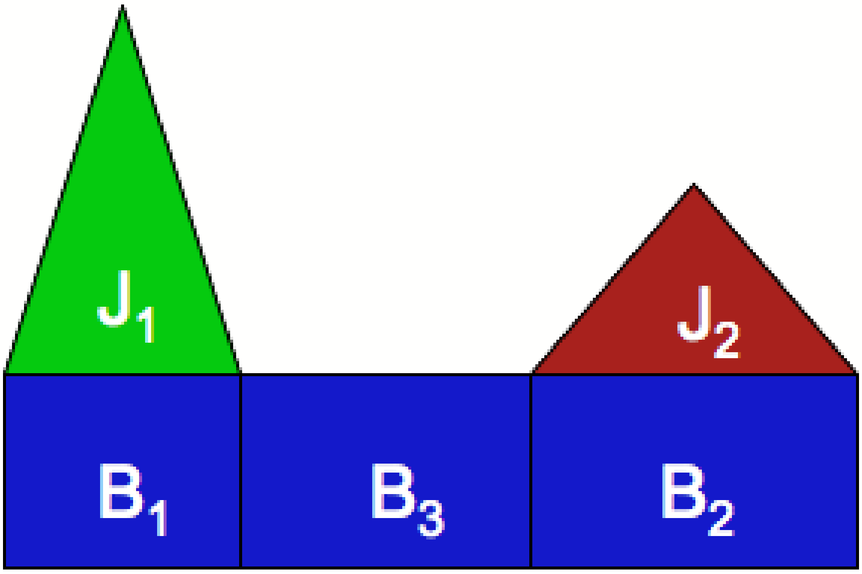

Figure 6.2: Allocation of regions in $\Delta\phi$ that are required to calculate the background, by hadron, to be subtracted from the jet signal.

remove B_1 and B_2 from y_1 and y_2 respectively where y denotes the yield from a jet region of $\Delta\phi$. Equation 6.1 revels how the subtraction can be performed for each individual hadron where h is the hadron, n is the jet region and td is the track density.

$$J_n^h = y_n^h - \{\Delta\phi_n B_3^{td}(\frac{B_3^h}{B_3^{all}})\} \tag{6.1}$$

The above equation shall be used to extract the jet spectra for pions, kaons and protons from the two particle correlations in the three systems, central and peripheral Au + Au and d + Au. The ratios $K^{\pm}/\pi^{\pm}$ and $p^{\pm}/\pi^{\pm}$ shall be calculated and compared for each system.

6.2 Unidentified $\Delta\phi$ Correlations

The correlations for peripheral Au + Au collisions are shown in figure 6.3 along with the integrated jet yields in figure 6.4. The jet yields were extracted using a mixed event background subtraction method using two dimensional particle correlations in azimuth and pseudorapidity as mentioned in section 4.7.2 and described in [107]. The resulting corrected two dimensional correlation was then projected onto the azimuthal axis where the near and away side peaks were then integrated

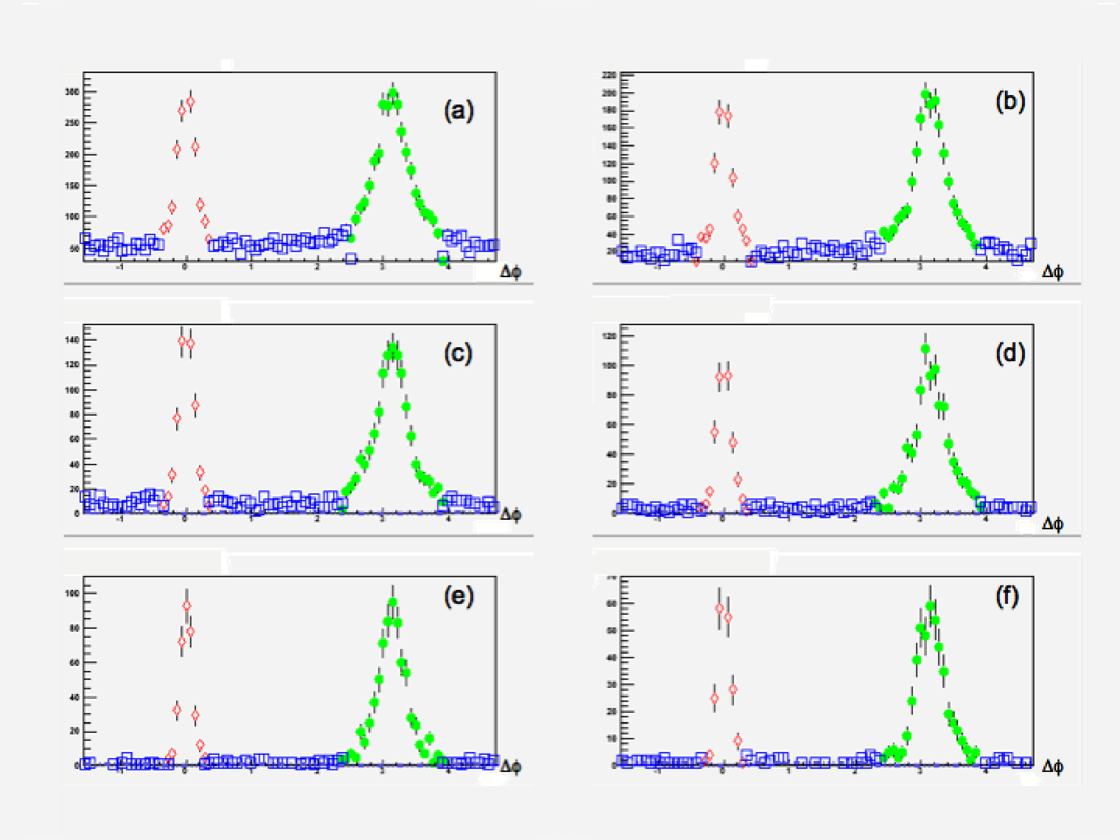

Figure 6.3: Unidentified neutral trigger correlations with unidentified charged tracks from peripheral $Au + Au$ events. From (a) to (f) the associated p_T is increasing in 0.5 GeV/c intervals from 3-3.5 GeV/c to 5.5-6 GeV/c. The red, green and blue markers indicate the near side jet, away side jet and background regions in azimuth respectively.

to ascertain the yields. This is a different subtraction method to the one that will be described in section 6.1.1 as it is only being used to determine the unidentified hadron yields.

The correlations show clear dijet signals in every p_T bin. The near side peak (situated at $\Delta\phi = 0$) is narrower than the away side peak (situated at $\Delta\phi = \pi$). This is caused due to the trigger bias that the near side peak always contains the trigger particle, which preferentially selects the jet with less attenuation in the medium and/or a harder fragmentation.The near side peak narrows as the associated p_T increases which indicates that the highest momentum associate particles are found closer to the jet axis. Incidentally, had all the neutral triggers been γ triggers there would not be any near side correlation. The near side correlation is therefore due to jets with a leading π^0.

The correlations for central $Au + Au$ are shown in figure 6.5. The away side jet is clearly suppressed, due to high p_T attenuation in the medium, when compared to the away side jet from

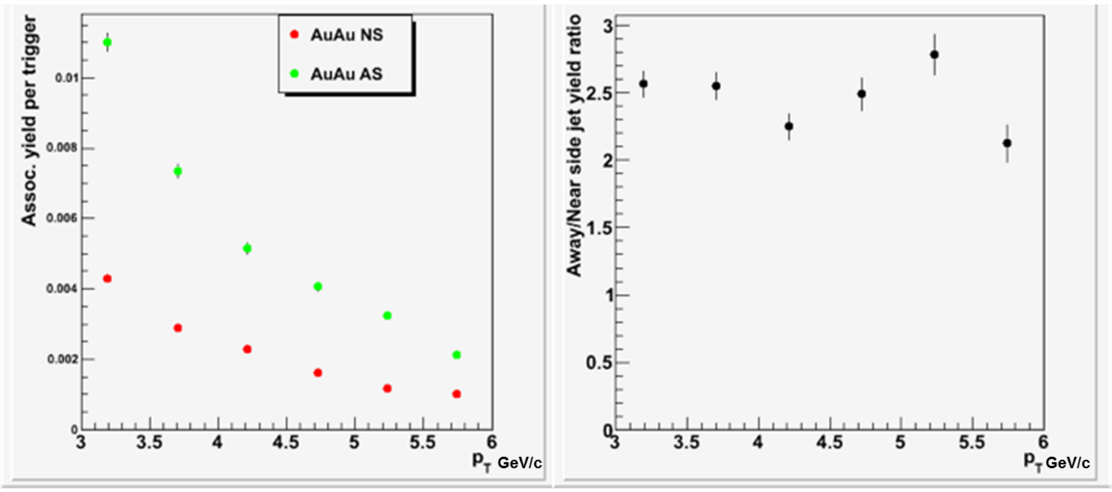

Figure 6.4: The left figure shows near side(NS) and away side (AS) yields in peripheral Au + Au collisions for associated tracks with $3 < p_T < 6$ GeV/c. The right figure shows the ratio of the away side yield to the near side yield. The ratio is approximately constant across the p_T range.

peripheral events. The contribution from the uncorrelated background is also far higher than in peripheral events as expected due to the higher event multiplicity. For example, in the p_T bin 3-3.5 GeV/c, the level of the background is a quarter of the height of the near side peak in peripheral collisions while the same comparison in central collisions reveals that the background is slightly greater than the height of the near side peak.

The background was then subtracted in the same way as described for peripheral Au + Au to determine the jet yields. Figure 6.6 reveals the jet yields per triggered event for the near side and away side and also their ratio. The extent of the away side suppression in central Au + Au is clearly noticeable when comparing the the away side to near side jet yield ratios from central collisions to peripheral collisions where the peripheral ratio is roughly twice as large.

The d +Au correlations (not shown), were found to be very similar to those from peripheral Au + Au. In d +Au, the away side to near side jet yield ratio was slightly higher than in peripheral Au+Au indicating that there is a small amount of attenuation in the peripheral events .

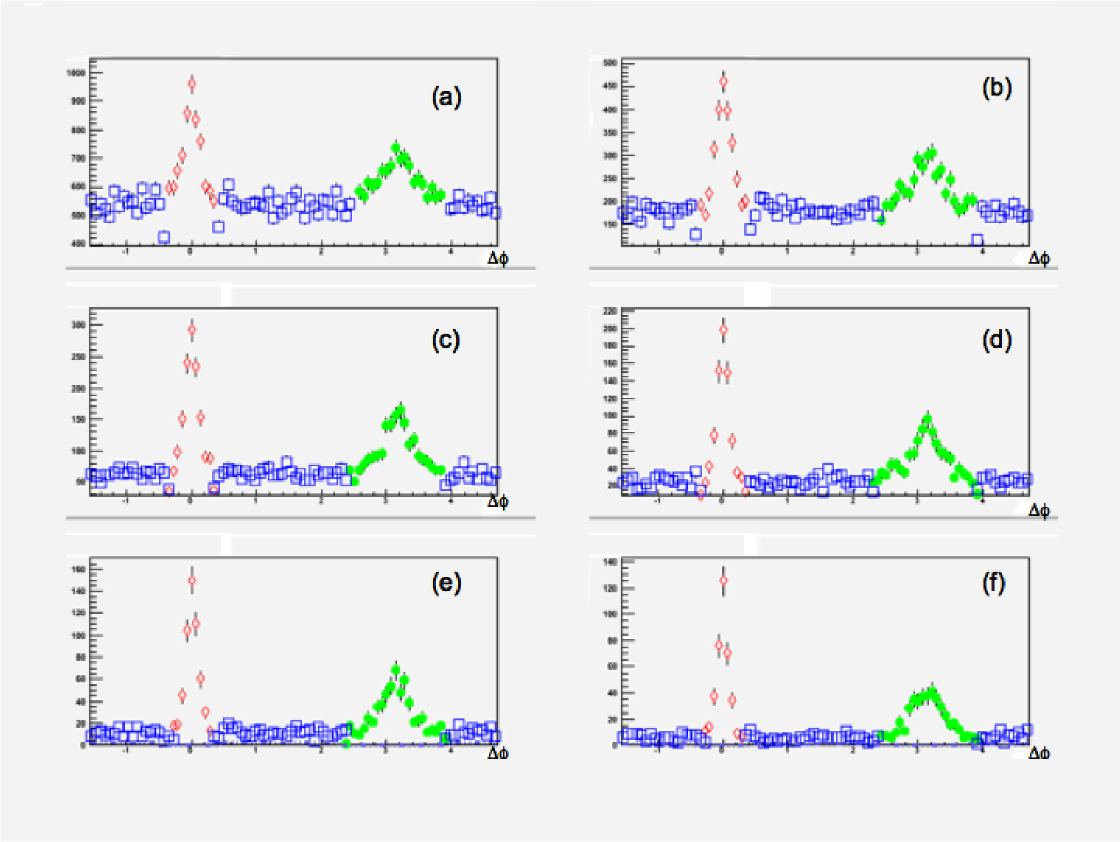

Figure 6.5: Unidentified neutral trigger correlations with unidentified charged tracks from central *Au* + *Au* events. From (a) to (f) the associated p_T is increasing in 0.5 GeV/c intervals from 3-3.5 GeV/c to 5.5-6 GeV/c. The red, green and blue markers indicate the near side jet, away side jet and background regions in azimuth respectively.

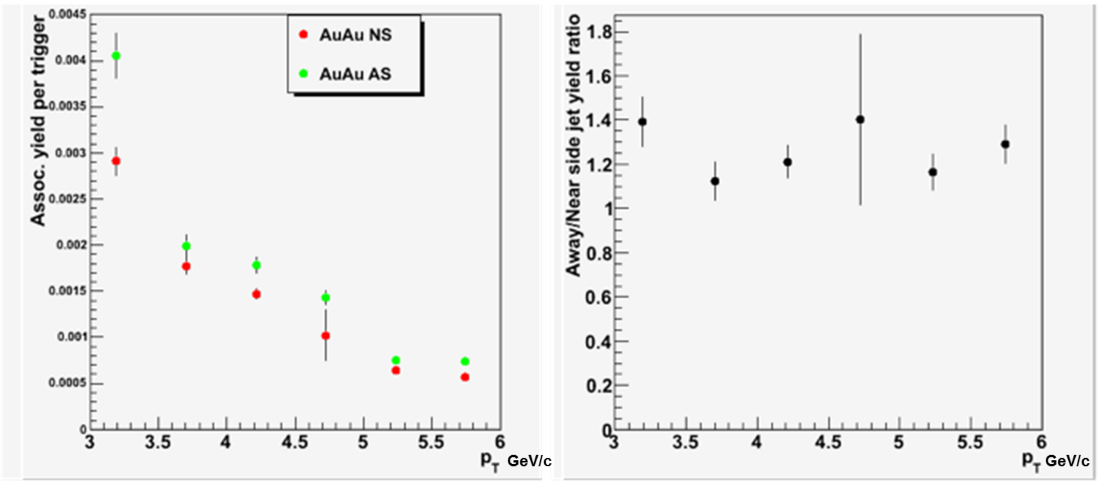

Figure 6.6: The left figure shows near side (NS) and away side (AS) yields in central *Au* + *Au* collisions for associated tracks with $3 < p_T < 6$ GeV/c. The right figure shows the ratio of the away side yield to the near side yield. The ratio is approximately constant across the p_T range.

6.3 Identified Hadron Ratios From Unidentified Neutral Energy Triggered $\Delta\phi$ Correlations

The $\frac{dE}{dx}$ data from the correlations in the previous section were analysed using the calibrated Bichsel functions for charged pions, kaons, electrons and protons. Positive and negative hadrons were combined to maximise the statistics that had been reduced having separated the data into three regions.

6.3.1 Charged hadron ratios $Au + Au$

The hadron ratios with respect to pions, $h^{\pm}/\pi^{\pm}$ have been calculated for each of the three regions of $\Delta\phi$, encompassing the near side jet, away side jet and uncorrelated background, for both central and peripheral collisions. The $p^{\pm}/\pi^{\pm}$ ratios from central collisions in figure 6.7(a), which have not had the uncorrelated background subtracted, clearly show that there is a proton $\Delta\phi$ dependency with the highest ratio in the background regions and the lowest ratio in the near side region.

The uncorrected $p^{\pm}/\pi^{\pm}$ ratio in peripheral collisions, shown in figure 6.7(b), is much lower than in central collisions. This indicates that there is a baryon enhancement in central $Au + Au$ collisions as was found in the inclusive p/π ratio from the 2004 $Au + Au$ data [39]. As the contribution from the uncorrelated background is smaller in peripheral $Au + Au$ than central $Au + Au$ as well as diminishing with p_T, there are large errors associated with the fit to the background $\Delta\phi$ region.

Figure 6.8 reveals how the uncorrected $K^{\pm}/\pi^{\pm}$ ratio is approximately p_T independent unlike the $p^{\pm}/\pi^{\pm}$ ratio. There is perhaps a slight dependence on $\Delta\phi$ region, which can be seen in both central and peripheral events, where the $K^{\pm}/\pi^{\pm}$ ratio is greater in the away side jet than the near side jet. The away side $K^{\pm}/\pi^{\pm}$ ratio not only is greater than the near side ratio in central collisions, but is also comparable to the background ratio.

In order to remove the background contribution from the jet $\Delta\phi$ regions, the average track density must be calculated so that the number of pions, kaons and protons are determined and subtracted

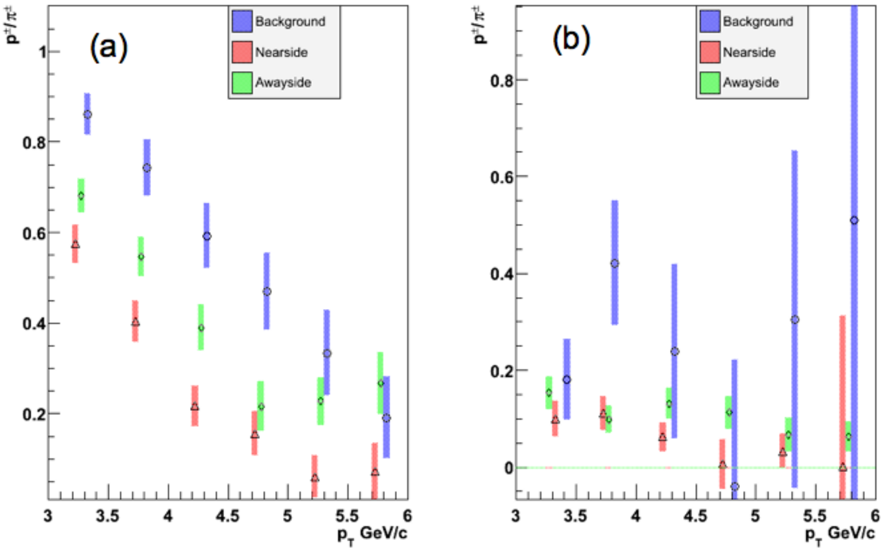

Figure 6.7: Uncorrected $p^{\pm}/\pi^{\pm}$ ratio $Au+Au$. Figure (a) shows the $p^{\pm}/\pi^{\pm}$ ratio from central $Au+Au$ for associated charged tracks with p_T from 3 to 6 GeV/c. Figure (b) shows the $p^{\pm}/\pi^{\pm}$ ratio from peripheral $Au+Au$.

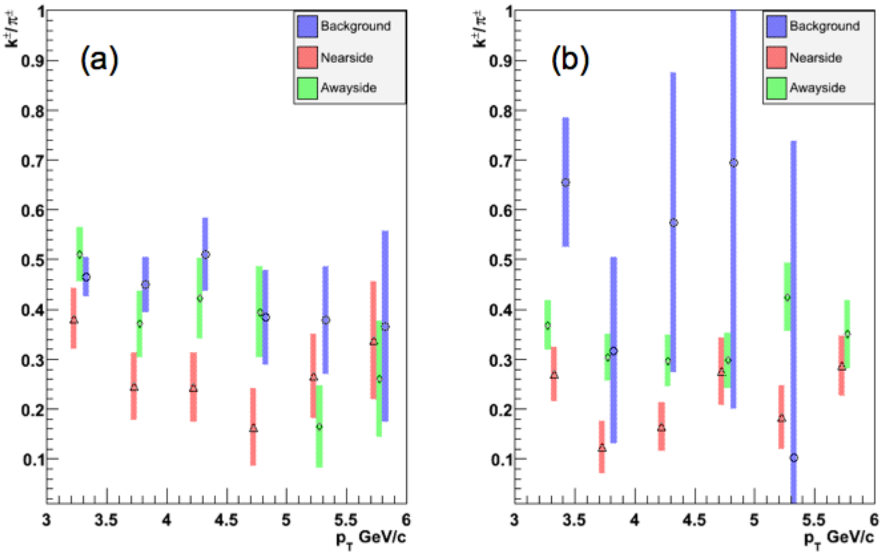

Figure 6.8: Uncorrected $K^{\pm}/\pi^{\pm}$ ratio $Au+Au$. Figure (a) shows the $K^{\pm}/\pi^{\pm}$ ratio from central $Au+Au$ for associated charged tracks with p_T from 3 to 6 GeV/c. Figure (b) shows the $K^{\pm}/\pi^{\pm}$ ratio from peripheral $Au+Au$.

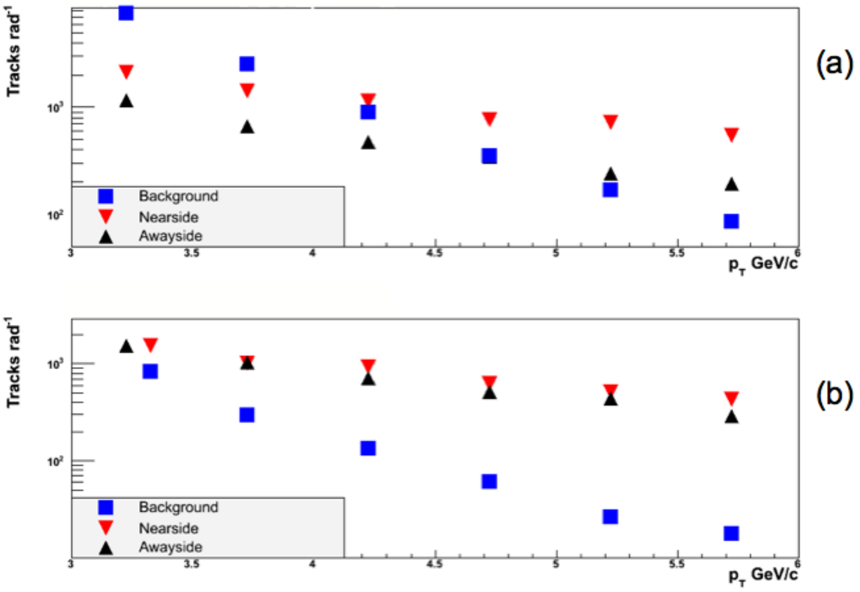

Figure 6.9: $Au + Au$ track density after subtracting track density associated with the background. The corrected track densities for central $Au + Au$ are in figure (a) for associated charged tracks with p_T from 3 to 6 GeV/c. The corrected track densities for peripheral $Au + Au$ are in figure (b).

separately. The track density can then be recalculated for the two jet regions to compare the density trends of each region. Figure 6.9 is the result of the track density correction in $Au + Au$. The background has the highest track density in central events up to a p_T of 4 GeV/c. The density of the background region is increased due to the trigger efficiency. No dijet correlation signal is present when events are selected where the trigger is a thermal particle from the underlying event.

The track density decreases in the background with a steeper slope indicating a softer production mechanism than the jet regions. The track densities of the near and away side jet regions are consistent in peripheral collisions (figure 6.9(b)) while in central collisions (figure 6.9(b)), the away side track density has been suppressed by the greater attenuation experienced in the medium by the away side jet.

6.3.2 Jet hadron yields $Au + Au$

The hadron yields for pions, protons and kaons were calculated for the three $\Delta\phi$ regions in each p_T bin for central and peripheral collisions. Figures 6.10, 6.11 and 6.12 display how the jet regions compare to the background region before background subtraction. The background region yields

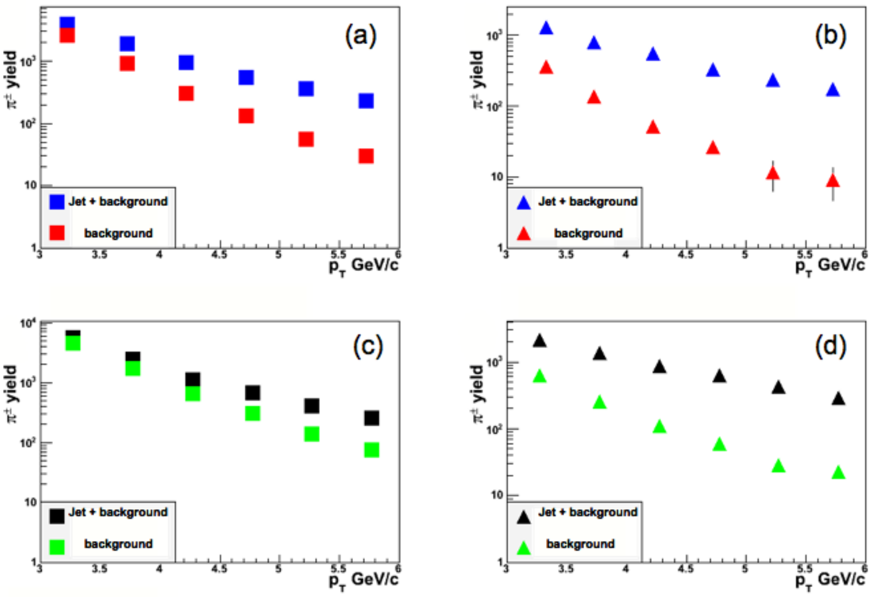

Figure 6.10: Charged pion yields in the Δϕ jet regions from central $Au + Au$ collisions. Figures (a) and (c) show the central $Au + Au$ charged pion yields for the near side and away side jets respectively. Figures (b) and (d) show the peripheral $Au + Au$ charged pion yields for the near side and away side jets respectively.

have been scaled to cover the same Δϕ as the jets. In each figure, the four panels *a*, *b*, *c*, and *d* represent central near side, peripheral near side, central away side and peripheral away side jets respectively.

The pion figure (figure 6.10), shows clearly that the background yield slope is steeper than the jet yield slope from 3-6 GeV/c. This indicates that the jet yield comprises of a hard p_T spectra. The background yield is of the same order as the jet yield in central collisions while in peripheral collisions it falls to an order of magnitude smaller after the 4-4.5 GeV/c bin.

The proton yields from figure 6.11 and the kaon yields from figure 6.12 should be examined as a pair. This is due to the yields being closely linked as a fluctuation in the fit function for either of the two hadrons is very likely to cause a fluctuation in the other particle's yield.

The proton data contain fewer statistics than the pion data and illustrate the difficulty of subtracting the large background. In central collisions, the background yield is very similar to the jet yields and is in fact the same within errors in all p_T bins of the central $Au + Au$ data set. Only the final two points of the away side data have a corrected proton yield that is not consistent with zero.

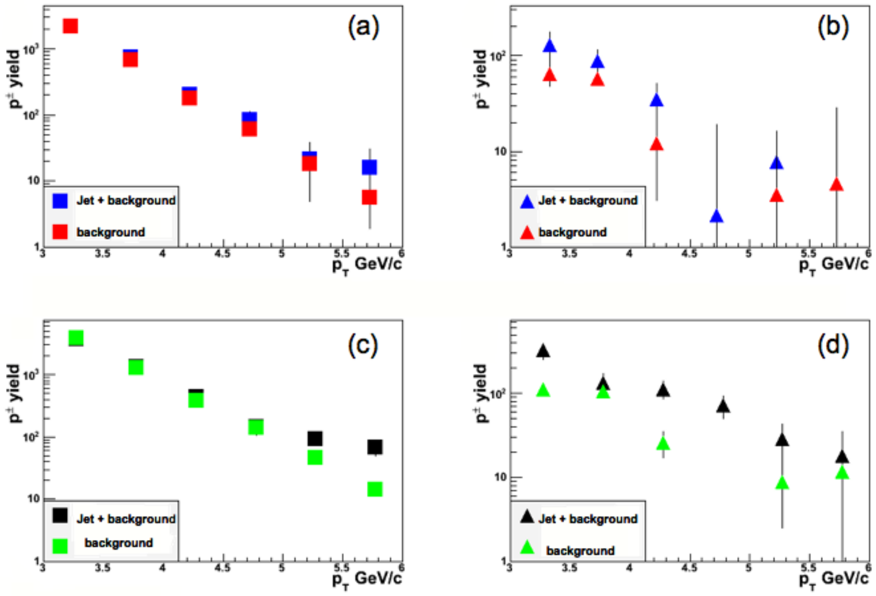

Figure 6.11: Combined $p + \bar{p}$ yields in the $\Delta\phi$ jet regions from central Au + Au collisions. Figures (a) and (c) show the central Au + Au $p + \bar{p}$ yields for the near side and away side jets respectively. Figures (b) and (d) show the peripheral Au + Au $p + \bar{p}$ yields for the near side and away side jets respectively.

The kaon yields show the greatest increase above the background in the final two p_T bins of the near side yields. There is also a slight dip in the 5-5.5 GeV/c bin of the away side kaon yield suggesting that the away side proton yield in this bin may be artificially high caused by a poor fit.

The peripheral proton yields are slightly unstable on the near side yields as the fit has struggled to accurately account for what is clearly a small jet contribution to the overall $\frac{dE}{dx}$ data. The away side peripheral proton yield appears more consistent, which is probably caused by a more accurately described kaon yield that accounts for a larger proportion of the $\frac{dE}{dx}$ data than in the near side region.

The main observation from these yield plots is that the background correction plays a critical part in determining the true jet hadron composition as the background yields are significant. The corrected yields will follow a review of the d + Au uncorrected hadron ratios.

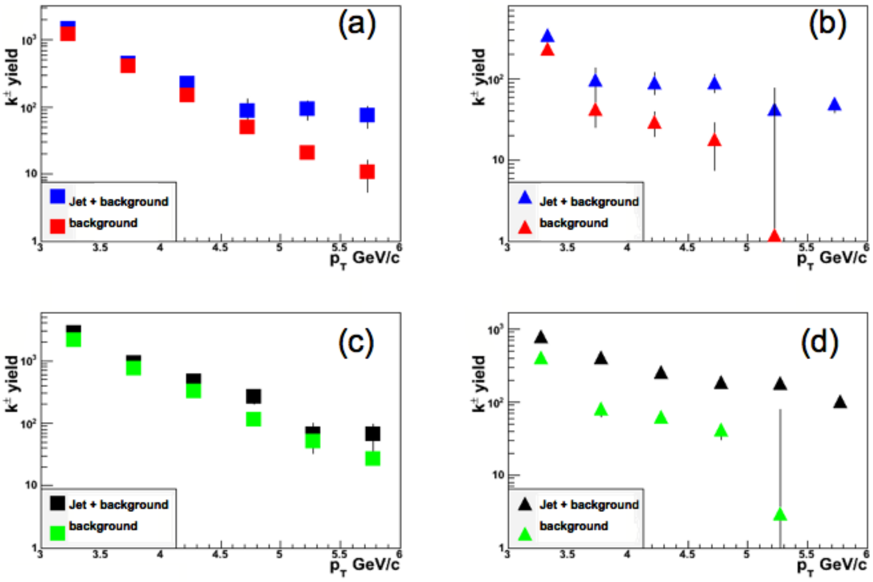

Figure 6.12: Charged kaon yields in the $\Delta\phi$ jet regions from central $Au + Au$ collisions. Figures (a) and (c) show the central $Au + Au$ charged kaon yields for the near side and away side jets respectively. Figures (b) and (d) show the peripheral $Au + Au$ charged kaon yields for the near side and away side jets respectively.

6.3.3 Charged hadron ratios $d + Au$

The hadron ratio calculations determined from the $d + Au$ data set have very small errors that make distinguishing the differences between near and away side jets far easier. The $p^{\pm}/\pi^{\pm}$ ratio without the background subtraction, seen here in figure 6.13, has been found to be p_T independent with the away side $p^{\pm}/\pi^{\pm}$ ratio constantly greater than the near side ratio.

Figure 6.14 shows that the $K^{\pm}/\pi^{\pm}$ ratio, without the background subtraction, is similar to that seen in peripheral $Au + Au$ where in both jet regions the ratio appears to be independent of p_T and the away side ratio is greater than that calculated for the near side.

Hard scattered particles in $d + Au$ are not expected to experience any significant attenuation in the aftermath of the collision. This expectation is illustrated in figure 6.15 where the track density of the away side jet is greater than that of the near side across the entire p_T range.

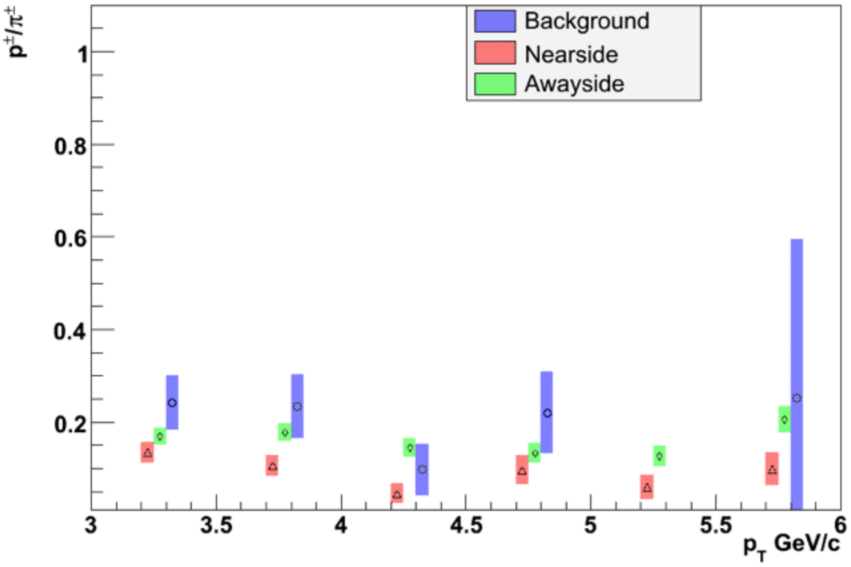

Figure 6.13: Uncorrected $p^{\pm}/\pi^{\pm}$ ratio $d + Au$. The $p^{\pm}/\pi^{\pm}$ ratio is calculated for associated charged tracks with p_T between 3-6 GeV/c.

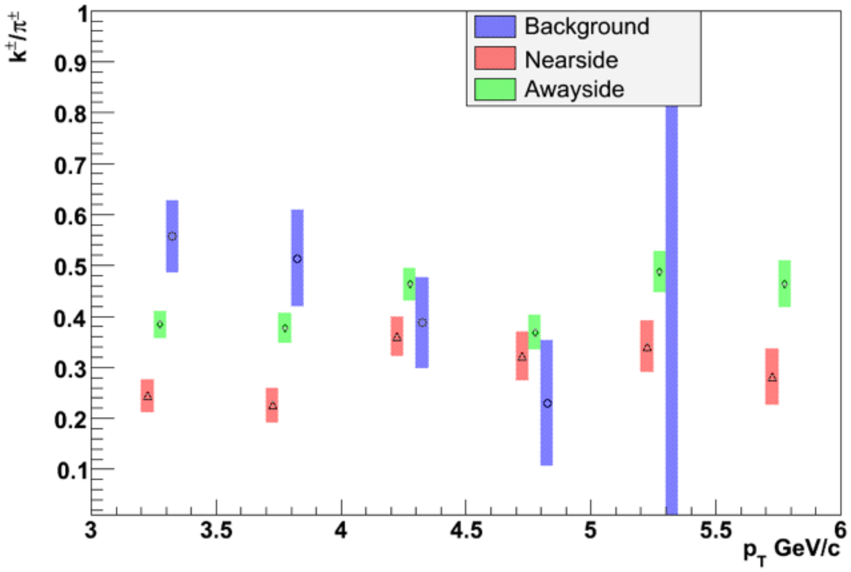

Figure 6.14: Uncorrected $K^{\pm}/\pi^{\pm}$ ratio $d + Au$. The $K^{\pm}/\pi^{\pm}$ ratio is calculated for associated charged tracks with p_T between 3-6 GeV/c.

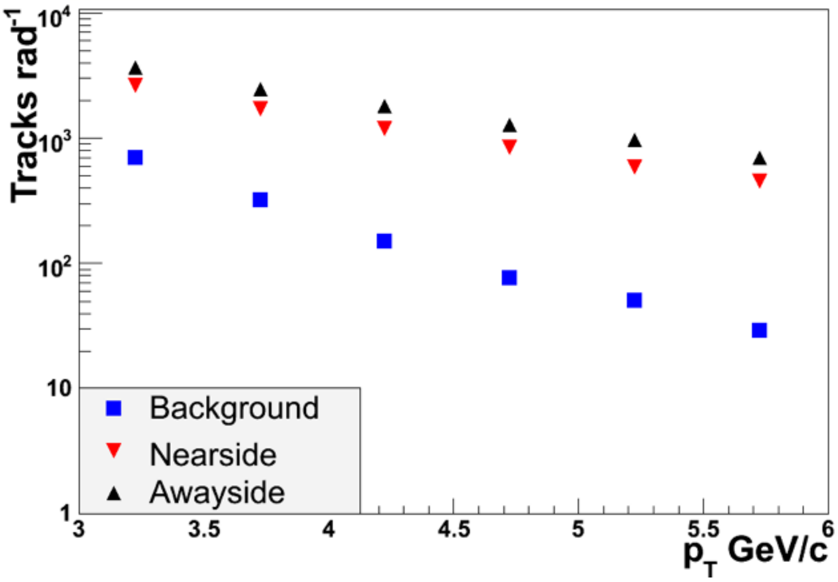

Figure 6.15: Background corrected track density $d + Au$ calculated for associated charged tracks with p_T between 3-6 GeV/c.

6.3.4 Jet hadron yields $d + Au$

The hadron yields for pions, protons and kaons were calculated for the three $\Delta\phi$ regions in each p_T bin (same as for $Au + Au$) in $d + Au$ collisions. Figures 6.16, 6.17 and 6.18 display how the jet regions compare to the background region before background subtraction. The background yield has been scaled to cover the same $\Delta\phi$ as the jets.

In figure 6.16, the background pion yields are an order of magnitude smaller than the jet pion yields in both near and away side jets. There is a large error associated with the fifth p_T bin that has been caused by a poor fit, which failed to fit the electron and proton contributions. This bin is not shown in figure 6.17 as zero is not on a logarithmic scale.

There link between the proton yields from figure 6.17 and the kaon yields from figure 6.18 does not appear to be as strong as that seen in central $Au + Au$ events. Still the slight fluctuations seen in the kaon yields appear to match those seen in the proton yields.

It was shown in central $Au + Au$ events that the background hadron composition was baryon rich. The background in $d + Au$ events is lower due to to a higher jet to background ratio but there is also no coalescence effect from the hadronisation of a QGP phase. The background in $d + Au$ events is

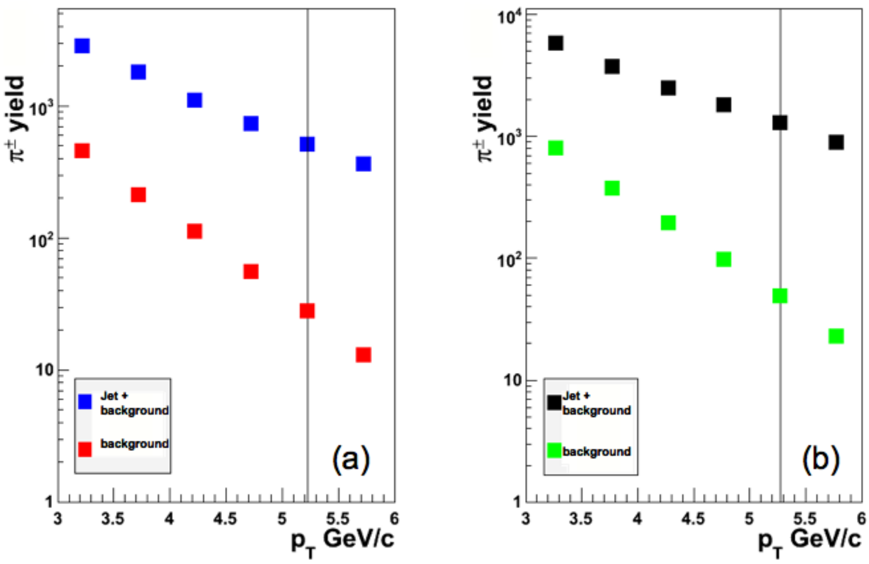

Figure 6.16: Charged pion yields in the $\Delta\phi$ jet regions from central d + Au collisions. Figure (a) shows the charged pion yields for the near side jet and figure (b) shows the charged pion yields for the away side jet.

also lower than in peripheral Au + Au. There is no expected baryon enhancement in peripheral Au + Au events, although this is inconclusive when considering the $p^{\pm}/\pi^{\pm}$ ratio of the background in figure 6.7(b), therefore the higher background can be attributed to a higher event track density.

The away side proton and kaon yields both follow an exponential curve, allowing for fluctuations, except for the final proton bin, which is clearly elevated without a partnering dip in the final kaon bin. This appears to be further evidence for identified leading baryons in the away side jet.

The yield plots for d + Au go in tandem with the observations made in figure 6.15. Namely that the away side jet is more densely packed with particles than the near side jet and produces a larger jet cone. As the leading particle in the near side is always a neutral hadron or photon, this leads to a charged leading particle bias on the away side as the away side jet has no leading particle constraints. Furthermore, as the away side jet must have a leading particle lower in p_T than the near side jet, there is an increased probability that the away side leading particle has a larger mass than that of the near side.

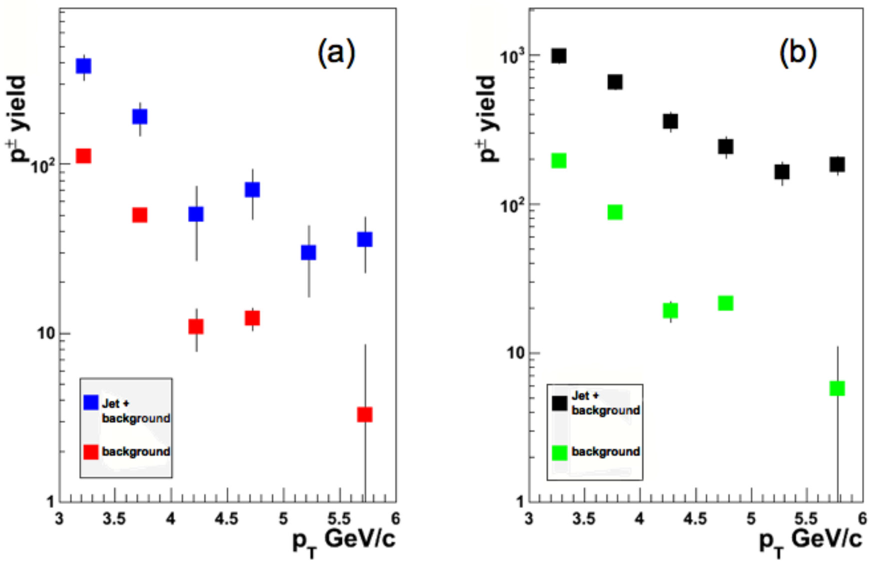

Figure 6.17: $p+\bar{p}$ in the $\Delta\phi$ jet regions from central d + Au collisions. Figure (a) shows the $p+\bar{p}$ yields for the near side jet and figure (b) shows the $p+\bar{p}$ yields for the away side jet.

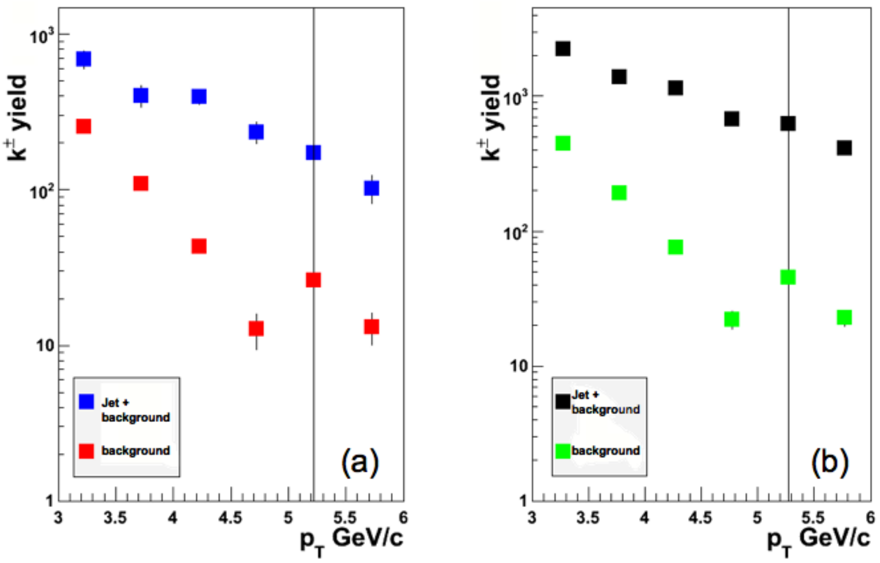

Figure 6.18: Charged kaon yields in the $\Delta\phi$ jet regions from central d + Au collisions. Figure (a) shows the charged kaon yields for the near side jet and figure (b) shows the charged kaon yields for the away side jet.

6.3.5 Corrected jet hadron yields *Au* + *Au* and *d* + *Au*

Before continuing with the results of the corrected jet hadron yields, it is important to state that the background subtraction method was not implemented for peripheral *Au* + *Au* or *d* + *Au*. While the background subtraction is essential in central *Au* + *Au* due to baryon enhancement, the background subtraction for peripheral *Au* + *Au* and *d* + *Au* collisions did not appear to contribute any significant modification to the hadron ratios.

This can be explained by considering that there were smaller background yields with larger errors extracted from the peripheral collisions than the central collisions. Furthermore, the peripheral *Au* + *Au* hadron ratios in the near and away side jet regions are consistent to those in the background region considering the large errors on the background ratios. Similarly for *d* + *Au*, the background hadron ratios were also very close to those in the jet regions. There was also the one p_T bin that could not be used to correct the jet hadron yields as the background fit had failed to produce a meaningful result.

The hadron ratios in central *Au* + *Au* were background corrected and then compared to the uncorrected hadron ratios of peripheral *Au* + *Au* and *d* + *Au*. Figure 6.19 compares the $p^{\pm}/\pi^{\pm}$ ratios for the three system sizes. The near side $p^{\pm}/\pi^{\pm}$ ratio is now consistent across all system sizes meaning that the corrected central ratio is independent of p_T. The away side $p^{\pm}/\pi^{\pm}$ ratio comparison is less conclusive due to the large uncertainty on the central *Au* + *Au* ratio. Notably, the first bin for central events on the near side is artificially low due to a poor fit to the $\frac{dE}{dx}$ data. Also, the proton and kaon peaks are at their minimum separation, in this p_T bin, therefore making it difficult to accurately extract the proton yield. The away side corrected ratio in this first bin is not shown as the corrected value is less than -0.1.

The interesting result is in the final two bins of the away side jet ratio. It can be argued that the increased $p^{\pm}/\pi^{\pm}$ ratio in central collisions is due to the under estimation of the kaon yields thus is artificial. This is probably the case for the $5.0 < p_T < 5.5$ GeV/c bin and may also be true for the $5.5 < p_T < 6.0$ GeV/c bin. Yet the same argument cannot be used for the *d* + *Au* events where there is also an increase in the $K^{\pm}/\pi^{\pm}$ ratio in these two p_T bins, which is evident in figure 6.20.

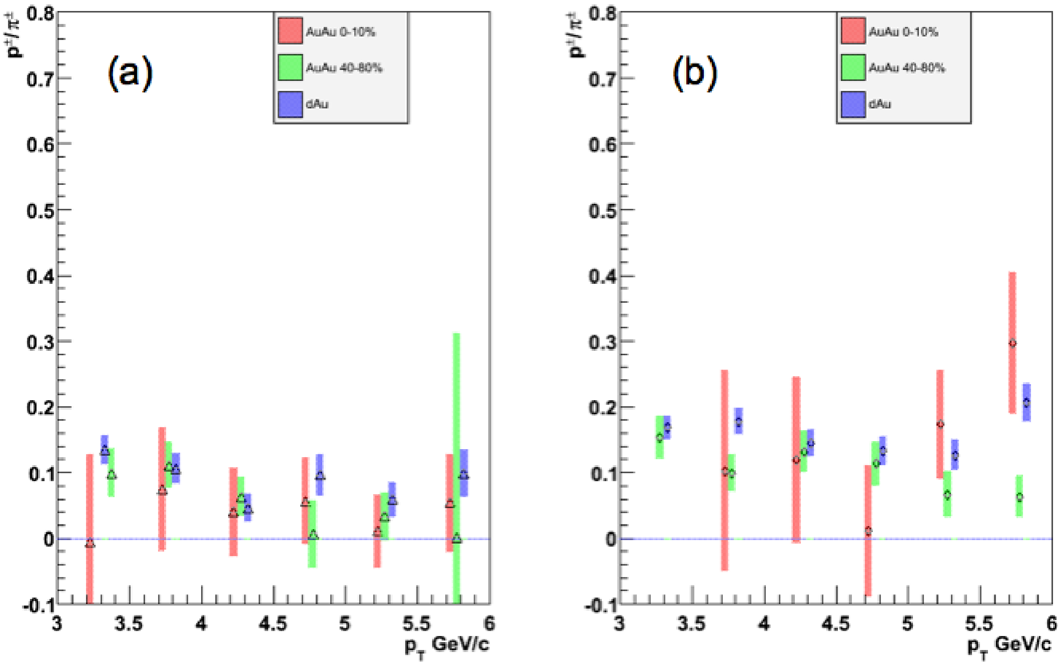

Figure 6.19: Background corrected $p^{\pm}/\pi^{\pm}$ ratio $Au+Au$ and $d+Au$. In figure (a), the corrected central $Au+Au$ near side $p^{\pm}/\pi^{\pm}$ ratio is compared to the near side uncorrected $p^{\pm}/\pi^{\pm}$ ratios from peripheral $Au+Au$ and $d+Au$. In figure (b), the corrected central $Au+Au$ away side $p^{\pm}/\pi^{\pm}$ ratio is compared to the away side uncorrected $p^{\pm}/\pi^{\pm}$ ratios from peripheral $Au+Au$ and $d+Au$.

What is further evidence that this increase in the $p^{\pm}/\pi^{\pm}$ ratio is not artificial is that it is not seen in the peripheral $Au+Au$ data. In fact, when comparing the p^{+}/p^{-} ratios in figure 5.14 and 5.15, there is not the increase in the p^{+}/p^{-} ratio in peripheral $Au+Au$ as was seen in $d+Au$ events, which was the first motivation to suggest that leading baryons are being detected. Therefore it cannot be ruled out that the increase in the away side jet $p^{\pm}/\pi^{\pm}$ ratio in central $Au+Au$ and $d+Au$ events are caused by different mechanisms.

Figure 6.20 compares the $K^{\pm}/\pi^{\pm}$ ratios for the three system sizes. All three systems exhibit similar ratios across the entire p_T range. There are more fluctuations in the $K^{\pm}/\pi^{\pm}$ ratio than the $p^{\pm}/\pi^{\pm}$ ratio. These fluctuations are probably caused because the kaon contribution is the most difficult to accurately determine as the kaon $\frac{dE}{dx}$ data overlaps with both the pion and proton data. The three near side p_T bins where the central $Au+Au$ $K^{\pm}/\pi^{\pm}$ ratio is lowest, correspond to the highest three $p^{\pm}/\pi^{\pm}$ ratio p_T bins of the central $Au+Au$ data. What can be established from figure 6.20 is that the $K^{\pm}/\pi^{\pm}$ ratio is higher on the away side than the near side jet. There is not conclusive evidence that the $K^{\pm}/\pi^{\pm}$ ratio changes with p_T in central events, suggesting that the $K^{\pm}/\pi^{\pm}$ ratio is p_T

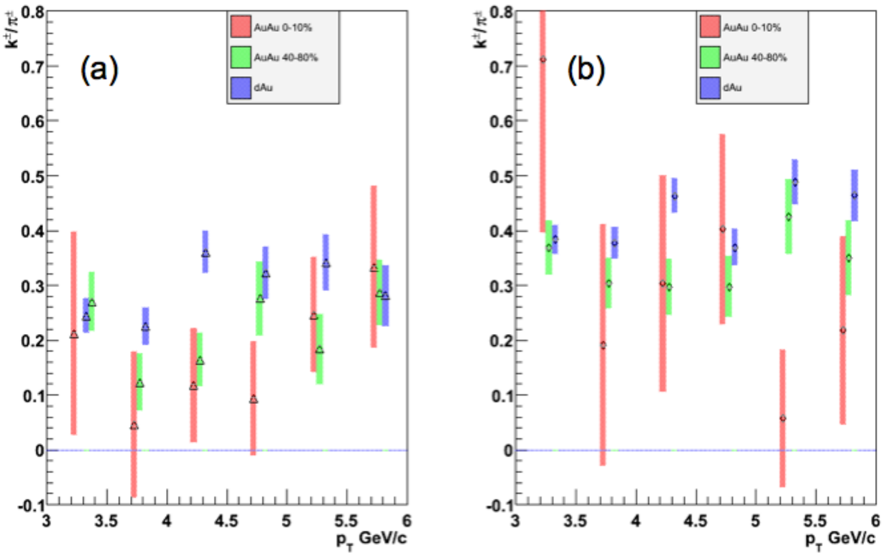

Figure 6.20: Background corrected $K^{\pm}/\pi^{\pm}$ ratio $Au + Au$ and $d + Au$. In figure (a), the corrected central $Au + Au$ near side $K^{\pm}/\pi^{\pm}$ ratio is compared to the near side uncorrected $K^{\pm}/\pi^{\pm}$ ratios from peripheral $Au + Au$ and $d + Au$. In figure (b), the corrected central $Au + Au$ away side $K^{\pm}/\pi^{\pm}$ ratio is compared to the away side uncorrected $K^{\pm}/\pi^{\pm}$ ratios from peripheral $Au + Au$ and $d + Au$.

independent.

6.3.6 Simulated $p + p$ hadron ratios.

To verify the results of section 6.3.5, the hadron ratios were compared to those created from Monte Carlo generated $p + p$ at $\sqrt{s} = 200$ GeV. The simulation package used was the Pythia 6.4 high energy event generator. This software package uses the *Lund String Model*, described in section 3.2.1, to facilitate fragmentation after a hard scattering event. The simulated results were filtered to obtain results that fell within the STAR experiment dimensions. One million $p + p$ events were selected that had a π^0 as the highest p_T particle with at least a p_T greater than 6 GeV/c. Once the events were selected, a two particle correlation was performed using the same p_T bins used for the experimental data. The hadron ratios were then calculated for the near and away side jets. As the simulated $p + p$ is a low multiplicity event and to be consistent with the treatment of the $d + Au$ data, no background correction was performed. The Pythia hadron ratios have been compared with the experimental hadron ratios in figures 6.21 and 6.22, which are the $p^{\pm}/\pi^{\pm}$ and $K^{\pm}/\pi^{\pm}$ ratios respectively.

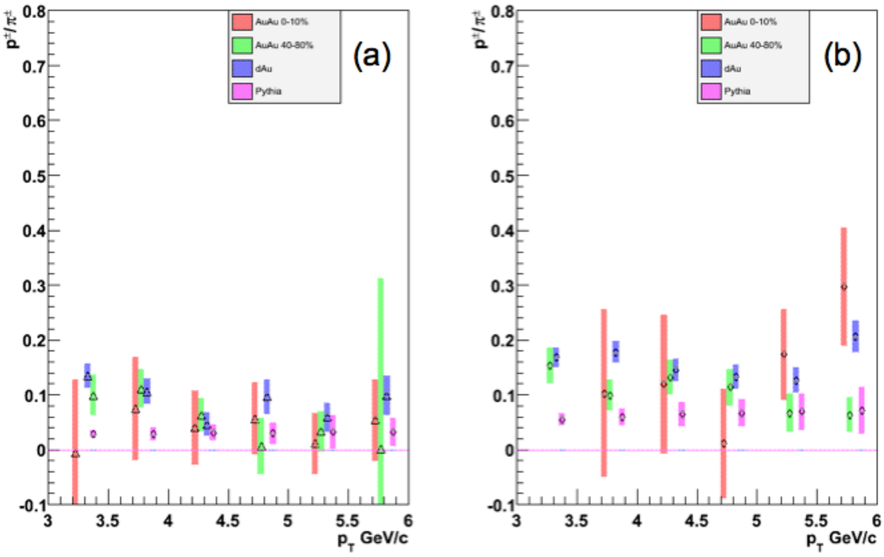

Figure 6.21: Background corrected $p^{\pm}/\pi^{\pm}$ ratio $Au + Au$ and $d + Au$ compared with Monte Carlo $p + p$ events. Figure (a) compares the $p + p$ simulated near side $p^{\pm}/\pi^{\pm}$ ratio with the near side $p^{\pm}/\pi^{\pm}$ ratios calculated from the central and peripheral $Au + Au$ data and the $d + Au$ data. Figure (b) compares the $p + p$ simulated away side $p^{\pm}/\pi^{\pm}$ ratio with the away side $p^{\pm}/\pi^{\pm}$ ratios calculated from the central and peripheral $Au + Au$ data and the $d + Au$ data.

The Pythia simulated data agrees with two of the observations that were made in the experimental data. Firstly that both the $p^{\pm}/\pi^{\pm}$ and $K^{\pm}/\pi^{\pm}$ ratios are independent of p_T. The second confirmation is that the away side hadron ratios are larger than the near side. The Pythia data points sit lower than the $d + Au$ and, at the lower end of the p_T range, the peripheral $Au + Au$ points. The indication here is that there remains a contribution from the background which was not subtracted due to a poor fit caused by fewer statistics in the background region. As the hadron ratios are independent of p_T in the Pythia data, there is no indication of a trigger bias that increases the $p^{\pm}/\pi^{\pm}$ ratio above $p_T = 5.5$ GeV/c on the away side jet. As the Pythia data used only π^0 triggers, that leaves the possibility that γ triggers cause this increase in the $p^{\pm}/\pi^{\pm}$ ratio assuming that the ratio is not artificially elevated by a poor fit.

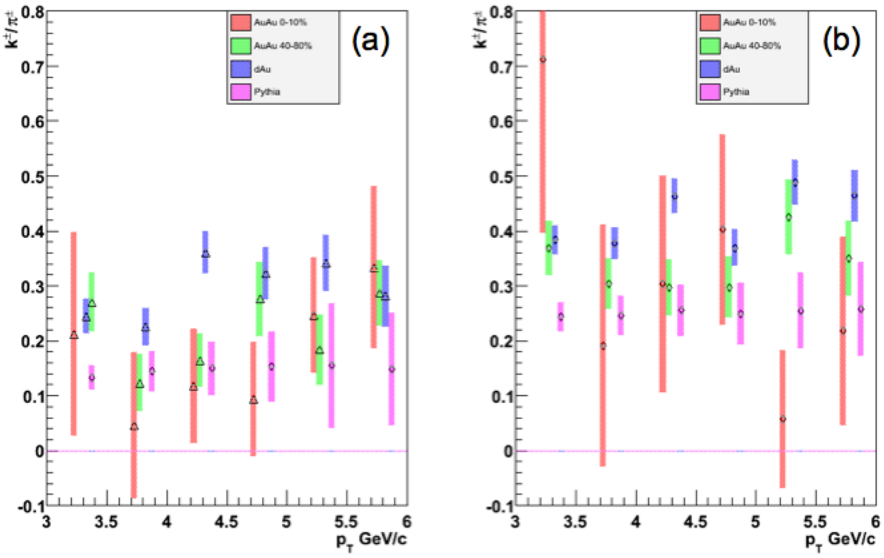

Figure 6.22: Background corrected $K^{\pm}/\pi^{\pm}$ ratio $Au + Au$ and $d + Au$ compared with Monte Carlo $p + p$ events. Figure (a) compares the $p + p$ simulated near side $K^{\pm}/\pi^{\pm}$ ratio with the near side $K^{\pm}/\pi^{\pm}$ ratios calculated from the central and peripheral $Au + Au$ data and the $d + Au$ data. Figure (b) compares the $p + p$ simulated away side $K^{\pm}/\pi^{\pm}$ ratio with the away side $K^{\pm}/\pi^{\pm}$ ratios calculated from the central and peripheral $Au + Au$ data and the $d + Au$ data.

6.4 Identified Hadron Ratios From Identified γ Triggered $\Delta\phi$ Correlations

The π^0 produces the largest background to direct photons in the *st-gamma* data. The symmetric decay of π^0s into two photons, where the two photons have very similar momentum and have a small opening angle, is the most prominent source of neutral triggers.

6.4.1 Direct photon identification

Once a neutral trigger has been found, it must then be identified using data from the barrel electromagnetic calorimeter shower max detector. As $p_T \sim 8$ GeV/c, the angular separation between the two photons at the barrel electromagnetic calorimeter face is typically smaller than the tower size. As there are two photons showering within the tower, a π^0 shower is generally broader than those produced from a single photon. The single direct photon is the desired trigger that can be used to identify γ-jet events. A transverse shower shape analysis, using the barrel electromagnetic calorimeter shower maximum detector, will be used to discriminate between direct photons and photons from the decay of high p_T π^0. To quantify the γ/π^0 discriminating power of the shower maximum detector, simulated direct photons and π^0s where embedded into actual *Au* + *Au* collision data [114]. The shower shape analysis was then implemented to see how effective the analysis technique was at discriminating between direct photons and π^0s.

The identified simulated particles are shown in figure 6.23. The transverse shower analysis looks at how the total energy of the particle is distributed radially from the centre of the shower in the shower maximum detector. The ratio $E_{total}/\sum_i e_i r_i^{1.5}$, where e_i is the energy of a shower maximum detector strip and r_i is the radius of the hit from the centre of the shower, is expected to be small for dual photon showers as the shower should be larger and the energy distribution less centralised given that there are effectively two showers overlapping. In the simulation, equal numbers of direct photons and π^0s were used therefore figure 6.23 does not represent a true physical interpretation of actual data. In the actual *st-gamma* data the γ/π^0 ratio is expected to be less than unity, which decreases the ability of this particular shower analysis to identify direct photons. In order to obtain a γ rich sample, only those triggers with $E_{total}/\sum_i e_i r_i^{1.5}$ between 0.25 and 6 were selected.

In addition to the shower analysis another factor can be used to improve the γ/π^0 discrimination. As the shower radius from two photons is generally larger than a single photon, the dual photon shower is more likely to fall across two towers in the barrel electromagnetic calorimeter. By comparing the energy of the highest energy tower with the highest energy neighbour tower such that, $\alpha = (E_1 - E_2)/(E_1 + E_2)$, where E_1 is the energy of the highest energy tower and E_2 is the energy of the highest energy neighbour tower, a second dimension is produced on which to identify direct photons. It is expected that α would be close to unity for the majority of direct photons while the full range in α is probable for π^0s. To isolate a γ rich sample, a cut on α was performed where only triggers with α greater than 0.6 were sampled.

The method for identifying γ triggers using the shower maximum detector was outlined in section 6.4.1. By using the shower maximum detector shower data, single photon trigger candidates should be identifiable. The two parameters required to isolate single photon triggers are α = (E1 - E2)/(E1 + E2), where E1 is the energy of the highest energy tower in the event and E2 is the second highest

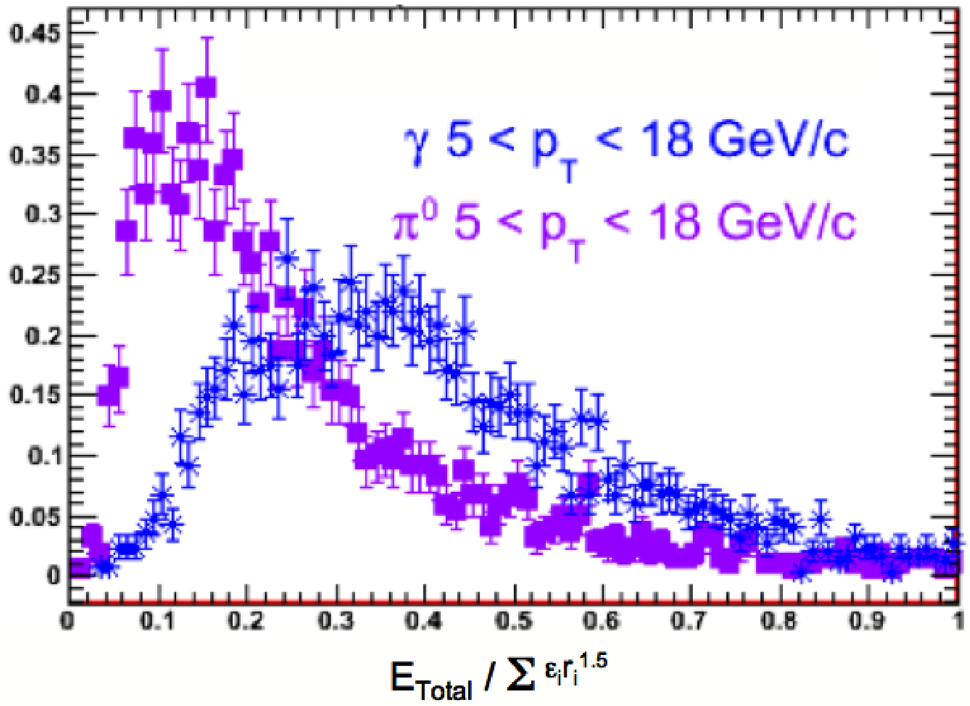

Figure 6.23: Identified direct photons and π^0 from $Au + Au$ events at $\sqrt{s_{NN}}$ = 200 GeV embedded with simulated direct photons and π^0 [114].

energy tower that is adjacent to the highest energy tower, and the total.

The energy parameters required to calculate α are compared in figure 6.24(a). The requirements for points to be selected were that they were the highest energy point in the event and that they had a total energy greater than 6 GeV. A point is a reconstructed particle detected using the shower maximum detector of the electromagnetic calorimeter. The energy in each shower maximum detector strip associated with the point is called a hit. A point may be reconstructed across a number of towers if a particle showers close to tower boundaries.

The biases introduced by the *st-gamma* level 2 trigger are easily identified. Firstly, there is a disjoining of the distribution where the trigger requirement of one tower registering an energy 5.75 GeV or greater. What can also be determined is that the tower that caused the level 2 trigger to fire, is not necessarily the highest energy point in the event. The data points where E1 is below 5 GeV is where these high energy points can be found that most fall across tower boundaries depositing similar quantities of energy in each tower.

It is important to remember that two or three towers can make up one point. Therefore it is not

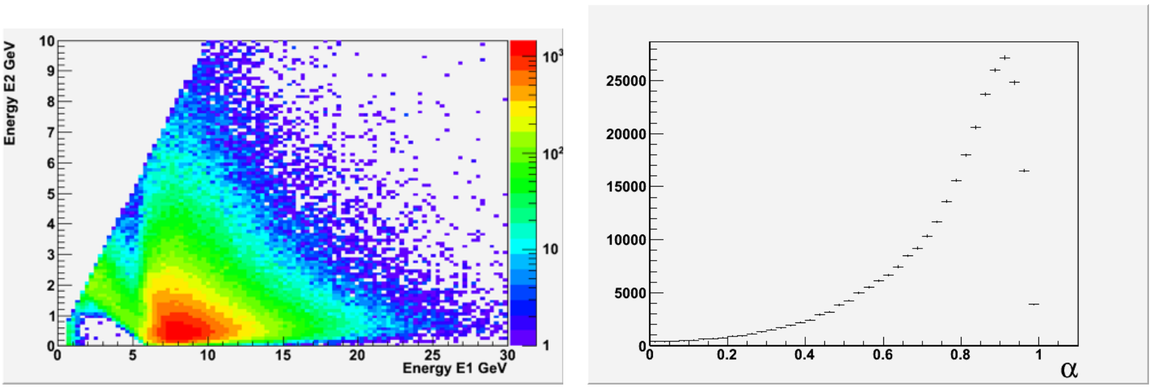

(a) (b)

Figure 6.24: Comparison between the the two highest energy towers where the total point energy greater than 6 GeV. Figure (a) compares the energy of the two highest energy towers in each point trigger. Figure (b) reveals the α distribution of the point triggers

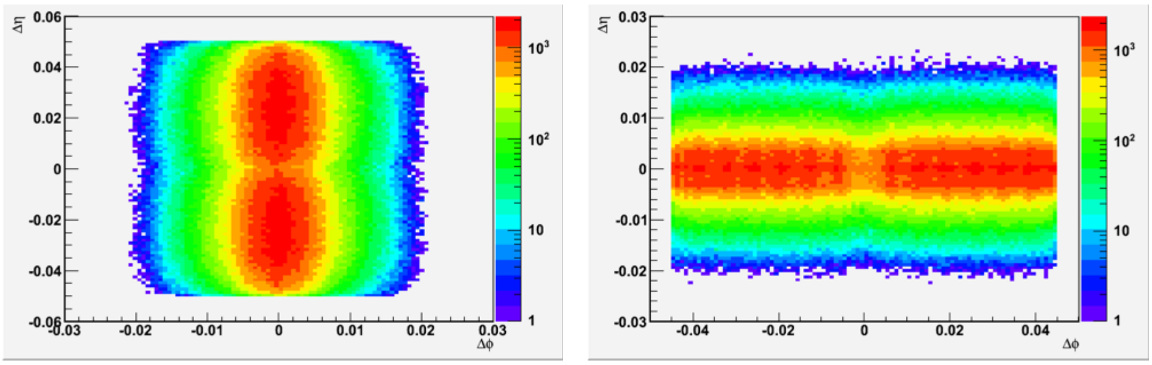

(a) (b)

Figure 6.25: Energy weighted strip position from centre of trigger point. The ϕ strips are shown in figure (a) and η strips are shown in figure (b). The positions are shown as a function of azimuth and pseudorapidity from the point centre.

necessary for $E1+E2$ to be greater than 6 GeV. The few events found in the bottom left hand corner are most likely caused by points where the third tower was corrupted and not included in the data set however the point energy stored in the data retained the corrupt tower data. α is shown in figure 6.24(b) and reveals that the distribution is heavily skewed to points that have deposited the majority of energy in a single tower.

To analyse the shower maximum detector shower data, the hits on the shower maximum detector η and ϕ strips need to be matched to calculate the distance from the point centre. The coordinates of each strip indicate the centre of the strip and not where the hit actually occurred. Therefore, in order to identify one hit, data from both sets of strips are required. Figure 6.25 displays the energy weighted $\Delta\phi\Delta\eta$ distribution of η and ϕ strip positions with respect to the point coordinates. The

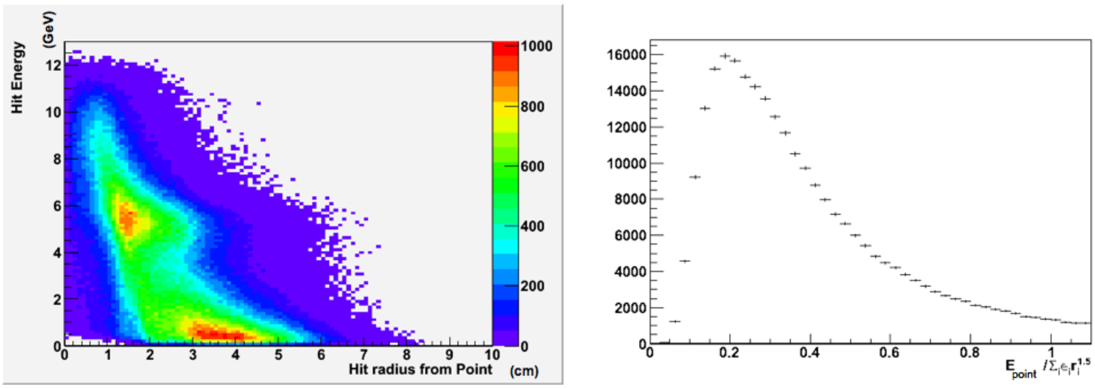

(a) (b)

Figure 6.26: Figure (a) shows the distribution of the point energy on the shower maximum detector from point centre. Figure (b) shows the total point energy to the sum of radius weighted hit energy ratio for each point trigger.

energy weighting emphasises how the energy is also focused at the centre of the point. As a reminder, each tower is 0.05 wide in both η and ϕ thus a strip can be a maximum of a single tower away from the point coordinates.

Once the hits have been identified on the η and ϕ strips the radius, from the centre of the point, can be calculated and compared to the hit energy. Each tower is roughly 10 cm in diameter and what is shown in figure 6.26(a) is that the hits are mainly well within this diameter. There appears to be two peaks in the distribution, where the smaller peak at 5 GeV is a consequence of the level 2 trigger. The other peak appears to be the second closest hit associated with the point. This observation implies that the majority of the energy is deposited in a single hit, with secondary hits contributing a much smaller proportion of the energy.

Figure 6.26(b) is the experimental equivalent of the simulated data shown in figure 6.23. The shape of the curve, when compared the the simulated data, indicates that there are contributions from both dual photon (π^0) and single photon (direct γ) triggers as neither of the simulated curves describes the experimental data. However, the distribution suggests that the triggers are dominated by π^0 mesons.

By combining α with the shower shape energy weighted analysis, a zone that is rich in γ triggers on the two dimensional plot can be selected as shown in figure 6.27. The zone corresponds to where the peak in the simulated γ triggers was found and also to points where the energy in highest energy

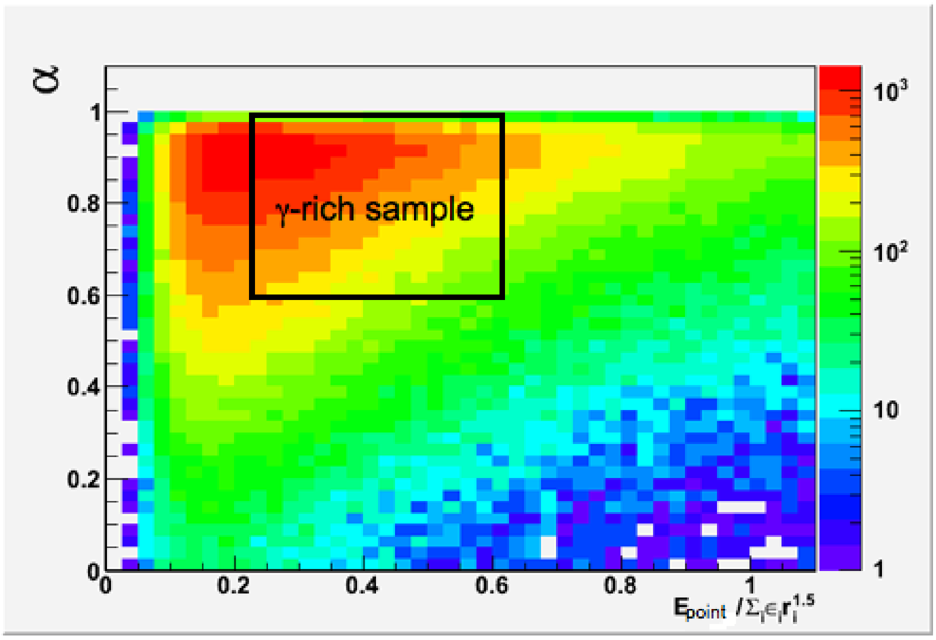

Figure 6.27: γ trigger identification method using α and the total energy to sum of radius weighted hit energy ratio. The black square indicates the region where the majority of the single photon showers are expected to be found.

tower is much greater than the energy in the second tower.

6.4.2 Jet hadron ratios determined from γ - charged hadron correlations

Having selected triggers from the γ rich zone of figure 6.27, two particle correlations were performed to produce the three $\Delta\phi$ regions required to calculate the jet hadron ratios. The correlations in figure 6.28 were created using the γ rich trigger set. Apart from a smaller number of tracks, there does not appear to be a great difference between the γ rich trigger data and the unidentified neutral trigger data. This is not surprising when the fact that 70% of all the triggers fall under the γ rich selection criteria. For a true γ - jet event, there should not be any associated particles, above the background on the near side as photons do not fragment into a jet-like cone of particles.

The simulated data in figure 6.23 used a 1:1 ratio of γs and $\pi^0 s$. The estimated γ/π^0 ratio from figure 3.13 using the current trigger energy of 6 GeV would be closer to 0.25. The conclusion from the γ isolation analysis must therefore be that the *st-gamma* data set is dominated by π^0 at 6 GeV. Even if it is assumed that the selection criteria for γ triggers removed only π^0 triggers, the γ rich sample would only have a maximum of 36% γ triggers. The sample will remain named *gamma*

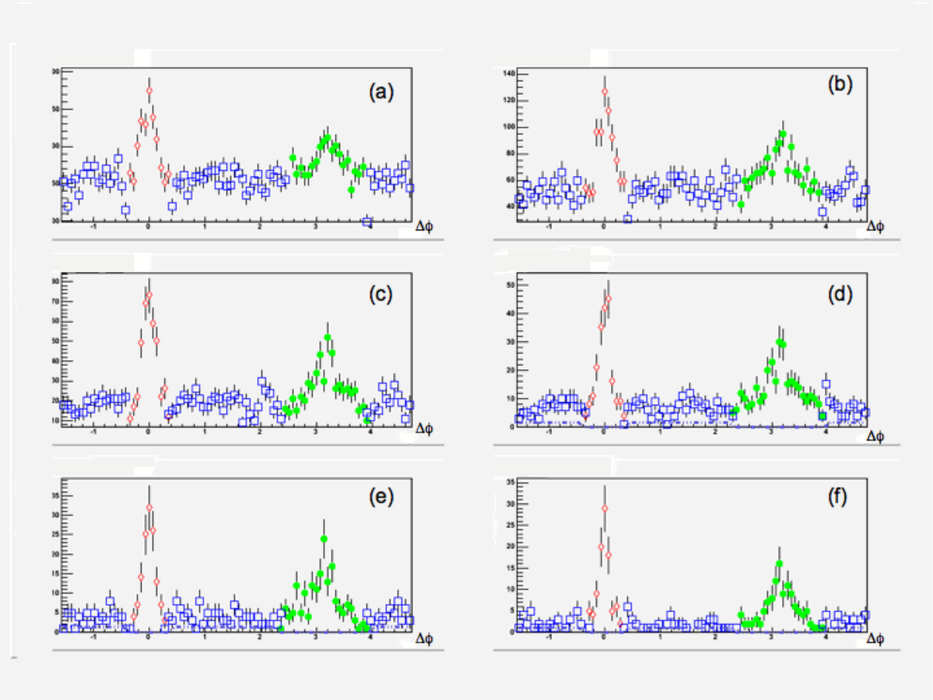

Figure 6.28: Identified γ trigger correlations with unidentified charged tracks from central $Au + Au$ events. From (a) to (f) the associated p_T is increasing in 0.5 GeV/c intervals from 3-3.5 GeV/c to 5.5-6 GeV/c. The red, green and blue markers indicate the near side jet, away side jet and background regions in azimuth respectively.

rich, not to indicate high purity, but to distinguish between the data set where all neutral triggers were considered and the data set where the γ selection cut was performed.

The $\frac{dE}{dx}$ data were analysed for the γ rich sample of triggers using the method developed for the central $Au + Au$ data. The results from the γ rich sample from central events were compared to the previously calculated results from section 6.3.5 for peripheral $Au + Au$ and $d + Au$. Even though only a 30% loss of statistics was sustained, the fits were evidently not as successful as those performed with the full neutral trigger data. Figure 6.29(b) and figure 6.29(a) show the uncorrected $p^{\pm}/\pi^{\pm}$ and $K^{\pm}/\pi^{\pm}$ ratios respectively.

In both figures there appears to be less distinction between the three regions than the calculation performed with the full data. The background regions have not been fit accurately in the final two bins making a background correction in these bins obsolete. There is however no rise in the $p^{\pm}/\pi^{\pm}$ on the away side of the γ rich data in these last two bins that cannot be explained simply by a dip in the $K^{\pm}/\pi^{\pm}$. This would seem to contradict the suggestion that γ-jet events were causing the peak seen in figure 6.19. The background corrected $K^{\pm}/\pi^{\pm}$ and $p^{\pm}/\pi^{\pm}$ ratios are shown in figures

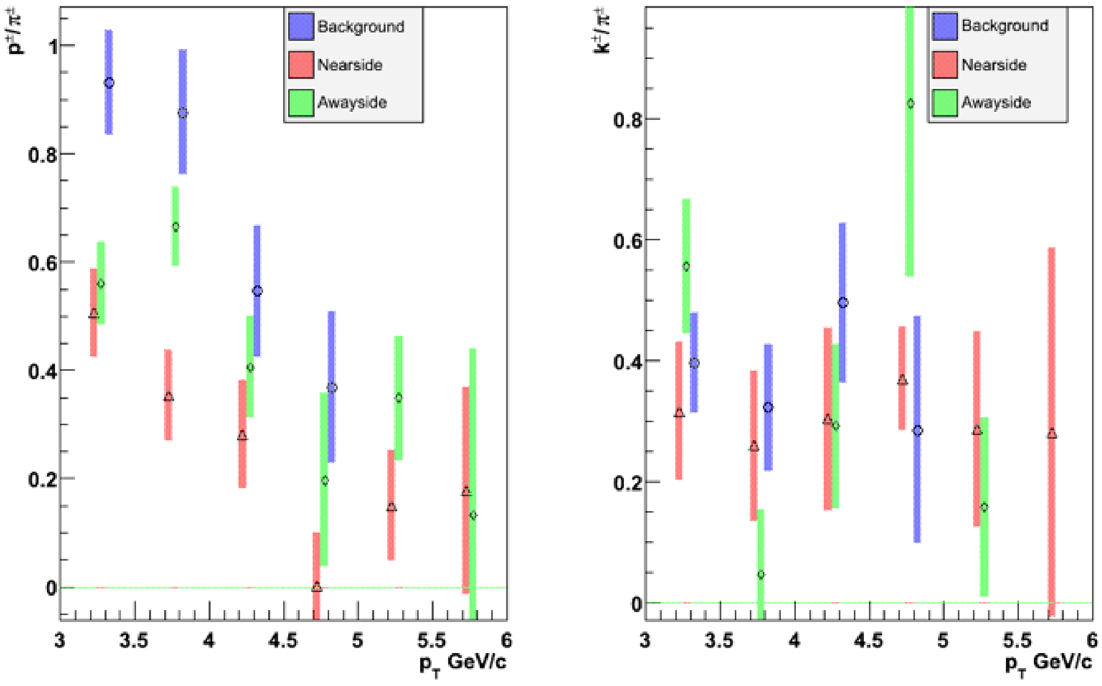

(a) (b)

Figure 6.29: Figure (a) reveals the $p^{\pm}/\pi^{\pm}$ ratios for the near side jet, away side jet and background regions of $\Delta\phi$, without the background correction, using γ rich central $Au + Au$ event selection. Figure (b) reveals the $K^{\pm}/\pi^{\pm}$ ratios for the near side jet , away side jet and background regions of $\Delta\phi$, without the background correction, using γ rich central $Au + Au$ event selection.

6.30(a) and 6.30(b) yet unfortunately, due to large errors and fluctiations, no clear conclusions can be drawn from them.

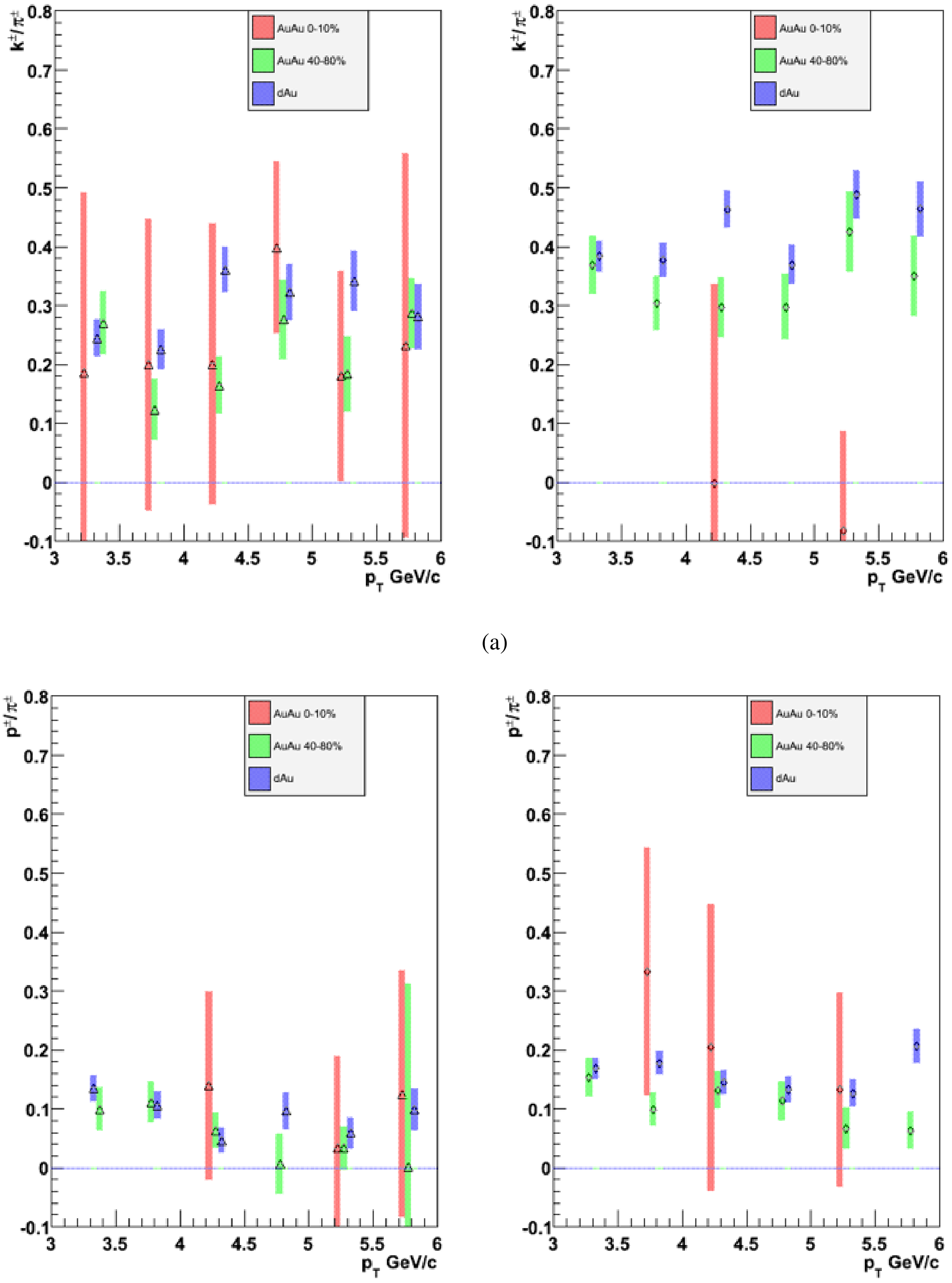

(a)

(b)

Figure 6.30: Background corrected $K^{\pm}/\pi^{\pm}$ and $p^{\pm}/\pi^{\pm}$ ratios using γ rich central $Au + Au$ event selection. Each figure shows the near side jet on the left and the away side jet on the right with the $K^{\pm}/\pi^{\pm}$ ratios shown in figure (a) and the $p^{\pm}/\pi^{\pm}$ ratios shown in figure (b).

Chapter 7

INTERPRETATION AND OUTLOOK

7.1 Discussion of Results

The goal of this analysis was to search for evidence of possible jet modification in the presence of a QGP via the study of jet particle spectra. In summary, the analysis has not been able to demonstrate that such modification occurs when hard probes interact with the QGP.

The main result from the overall analysis is that the corrected hadron ratios for the three system sizes, using the unidentified neutral triggers data, compared well with the simulated $p + p$ events. Although a single photon trigger identification method was tested, it was unable to produce conclusive results when the $\frac{dE}{dx}$ data was analysed. A summary of the results from chapter 6 are given below:

- In $Au + Au$ collisions, the ratio of the away side jet yield to the near side jet yield is roughly twice as large in peripheral $Au + Au$ than in central $Au + Au$ indicating that a larger attenuation, by interacting with the medium, is experienced in central $Au + Au$. In both cases the ratio of the yields was found to be independent of p_T.
- In $Au + Au$ collisions, the $p^{\pm}/\pi^{\pm}$ ratio is highest in the uncorrelated background and the away side jet $p^{\pm}/\pi^{\pm}$ ratio is larger than the $p^{\pm}/\pi^{\pm}$ ratio in the near side jet. The background $p^{\pm}/\pi^{\pm}$ ratio reveals a p_T dependence in central $Au + Au$ consistent with the baryon enhancement observed in the intermediate p_T region (2-5 GeV/c). This is not observed in

the jet spectra.

- In $Au + Au$ collisions, the $K^{\pm}/\pi^{\pm}$ ratio was found to be p_T independent and was larger in the away side jet than the near side jet.
- In $d + Au$ collisions, the $p^{\pm}/\pi^{\pm}$ ratio and $K^{\pm}/\pi^{\pm}$ ratio showed the same ordering as $Au + Au$ collisions where the away side ratios were found to be higher than the near side ratios.
- In $d + Au$ collisions, the $p^{\pm}/\pi^{\pm}$ ratio and $K^{\pm}/\pi^{\pm}$ ratio where found to be p_T independent in the background and jet spectra.
- The background corrected near and away side jet $p^{\pm}/\pi^{\pm}$ ratios showed no p_T dependence in any of the colliding systems. This was verified using simulated $p + p$ data.

The analysis provides evidence that two particle correlations are a simple yet effective way of extracting information about the particle composition of jets. The track density study has shown, in $Au + Au$ events, that the background $\Delta\phi$ regions contain particles created from soft processes (steep slope) while the jet regions particles have a significantly flatter p_T distribution, which is to be expected for hadrons produced by fragmentation.

Though developing the methodology used for analysing the $\frac{dE}{dx}$ relativistic rise data was challenging , the resulting fits produced hadron ratios trends and values that agreed with simulated $p + p$ data. The method developed was the first used at STAR not to use constraints on the hadron yields, such as fixing the $K^{\pm}$ yield with the K^0_{Short}, and fit the proton and kaon yields separately.

Overall, subject to sufficient statistics and detector performance, the analysis techniques used are a powerful jet analysis tool.

As expected, the study of γ-jet events proved to be very difficult. Although the technique has been shown to produce a near pure sample of π^0s and a γ rich sample of triggers, the reduced statistics destabilised the fit function when applied to the three regions in $\Delta\phi$ [114].

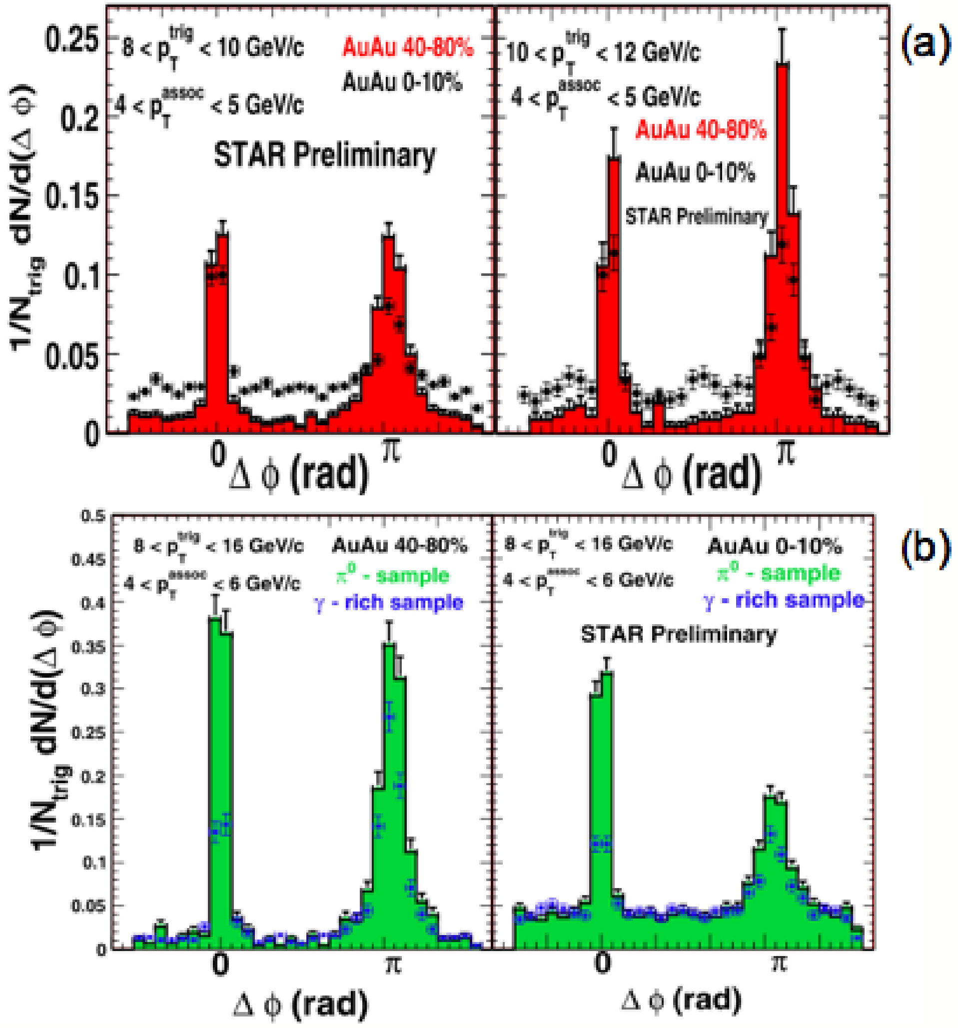

Figure 7.1: Identified photon trigger correlations with unidentified charged tracks from central (0-10%) and peripheral (40-80%) $Au + Au$ events at $\sqrt{s_{NN}} = 200$ GeV. Figure (a), with red correlations, use unidentified neutral triggers, while figure (b), with green correlations, compare correlations with π^0 and γ rich triggers [114].

7.1.1 Interpretation of results

Figure 7.1(a) is a two particle correlation using neutral triggers and unidentified charged tracks for central and peripheral $Au + Au$ collisions at $\sqrt{s_{NN}} = 200$ GeV. Figure 7.1(b) shows how the near side yield per trigger is reduced when using the γ rich trigger sample when compared to the near pure π^0 sample. The away side yield per trigger is also slightly reduced when using γ triggers. The reduced away side is caused by two processes: a reduced surface bias from using a photon trigger and π^0 triggered events containing a trigger with a higher initial parton energy.

If the second process is the dominant process, this supports the theory that the energy loss experienced by high p_T particles occurs at the parton level before fragmentation. This could lead to the conclusion that the fragmentation process is unaffected by interactions with the medium, which is supported by the results of this analysis.

There is a second scenario that would permit modification of the jet fragments whilst traversing the medium without being detected in the two particle correlation. If a parton were to fragment, the fragment may only remain correlated to the initial parton if it suffered no further interactions. Once part of the medium, the fragment parton is subject to the colour rich medium and therefore is likely to become thermalised with its surroundings. Even if the hadronisation process has changed due to interactions with the medium, the initial fragmented parton is no longer correlated to the parent parton and thus is not detected as part of the jet signal.

The theoretical study described in section 3.4.4 that predicted a shifting of the jet spectra to heavier hadrons, caused by enhanced parton splitting, was able to track each jet fragment throughout the fragmentation event [83]. The study also used LHC scale energy with jet energies an order of magnitude higher than those accessible at RHIC. Therefore jet modification at RHIC energy may occur at lower p_T than the range analysed. By using high energy jets only, there is an increased chance that any jet fragments that interacted with the medium may retain some correlation to the jet axis. However pushing the trigger energy threshold higher would have significantly reduced the available statistics in this analysis.

7.1.2 Further observations

There has been extensive study to learn how the spatial features of a jet are effected by the medium produced in $Au + Au$ collisions. One prominent piece of evidence for jet modification is a broadening of the near side jet peak along pseudorapidity, in hadron triggered two particle correlations in central $Au + Au$, known as the ridge. There are many theories as to what causes the ridge seen in figure 7.2(a), for example splash back from a quenched jet [115], linked to the anisotropic flow experienced in the event [116], or caused by a parton cascade that broadens with the longitudinal expansion of the medium [117]. This analysis was seen as an opportunity to strengthen the argument that the ridge is caused by the away side jet if the γ jet data produced a ridge.

Figure 7.2(a) shows a typical jet plus ridge image from a $\Delta\phi\Delta\eta$ correlation situated at $\Delta\phi = 0$ in the η plane. There is no away side peak as jets are not back-to-back in $\Delta\eta$ due to the initial scattering partons having varying longitudinal momentum. The correlation was exclusively between charged tracks where the trigger p_T was between 3-6 GeV/c and the associated p_T was greater than 2 GeV/c but less than that of the trigger. Figure 7.2(b) is a two particle correlation from $d + Au$ events that uses the same trigger and associated track p_T cuts as in figure 7.2(a).

There is no broadening of the near side jet peak along pseudorapidity in $d + Au$ as no medium is expected to be created. Figure 7.2(c) was created using the *st-gamma* data from central $Au + Au$ collisions and used a trigger E_T greater than 6 GeV with an associated charged track p_T between $3 - 3.5$ GeV/c . The $\Delta\phi\Delta\eta$ correlation from the *st-gamma* data strikes a far greater resemblance to the correlation from $d + Au$. There is no sign of the ridge in the *st-gamma* data where previous studies have shown that with these trigger and associated parameters the ridge is still visible [107].

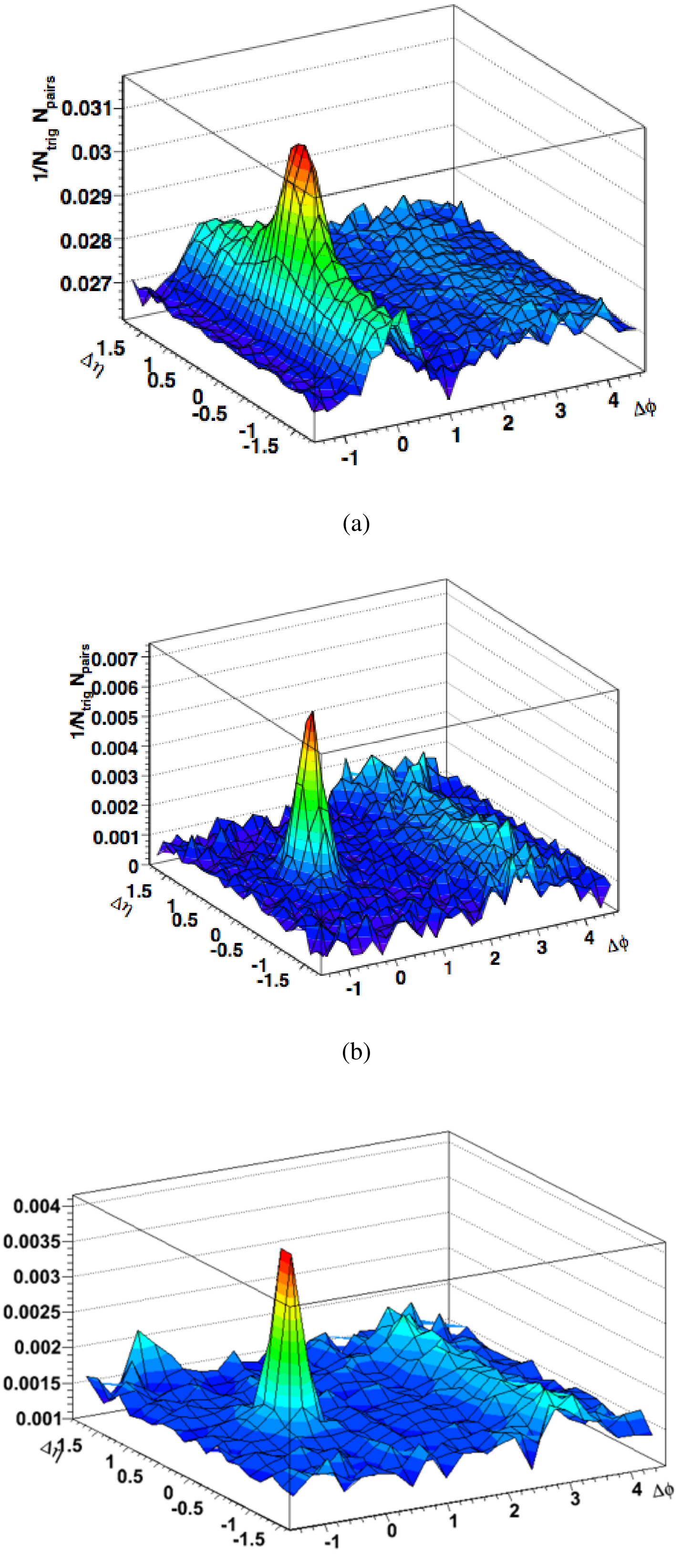

(a)

(b)

(c)

Figure 7.2: Comparison between, (a)$\Delta\phi\Delta\eta$ charged-charged correlation in central $Au + Au$ collisions, where trigger p_T between 3-6 GeV/c and associated p_T between 2 and the trigger p_T, with (b) the same correlation except performed for $d + Au$ collisions, and (c) barrel electromagnetic calorimeter triggered neutral-charged correlations in central $Au + Au$ collisions, where trigger E_T is greater than 6 GeV and associated p_T is between $3 - 3.5$ GeV/c .

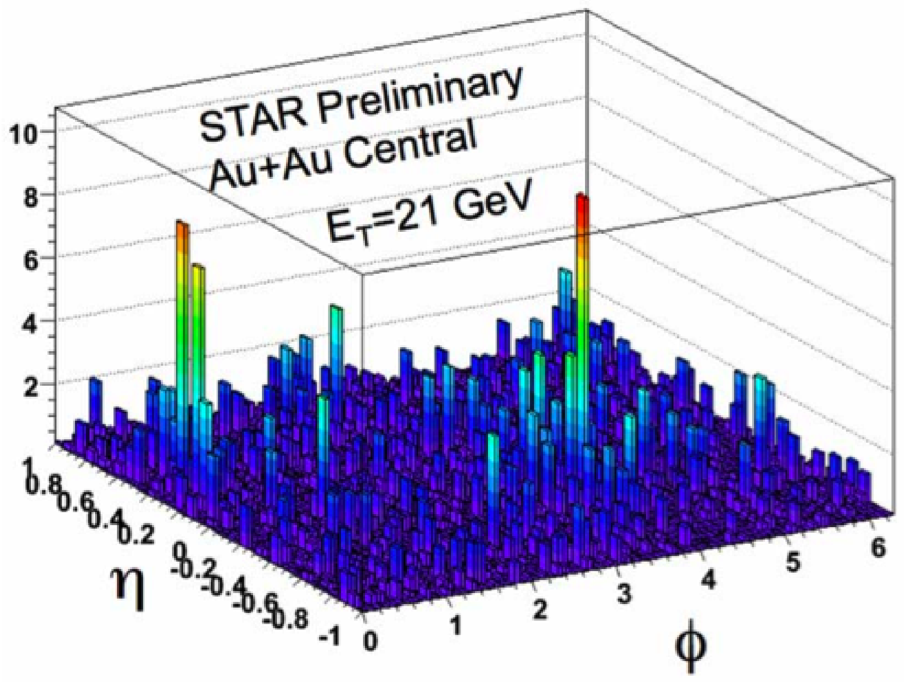

Figure 7.3: Reconstructed dijet from a single central $Au + Au$ event [118]. The jet consists of both charged track momentum and neutral energy deposited in the STAR BEMC.

7.2 Outlook for Jet Studies in Heavy Ion Collisions

7.2.1 Recent jet identification studies in $Au + Au$ collisions

Two particle correlations are not the only tool being used to identify jets in heavy ion collisions. Jet reconstruction algorithms have been developed to reconstruct jets in a high multiplicity environment such as a central $Au + Au$ collisions [118]. If jets can be successfully reconstructed and have the background contribution removed, using algorithms on an event by event basis, they would not suffer the same geometric biases as those seen in two particle correlations, which are dominated by relatively low energy jets that have had little interaction with the medium and then fragment into a few higher p_T particles [72]. Cone algorithms are not new to jet finding and have been used since the early 1980s yet they have until now only been used in leptonic or hadron collisions not nuclear collisions.

The algorithm looks for jet ”seeds” in the event with a minimum energy of 4.6 GeV. A jet cone with a radius of 0.4 in the $\eta - \phi$ plane is placed around the seed and the energy of all the particles

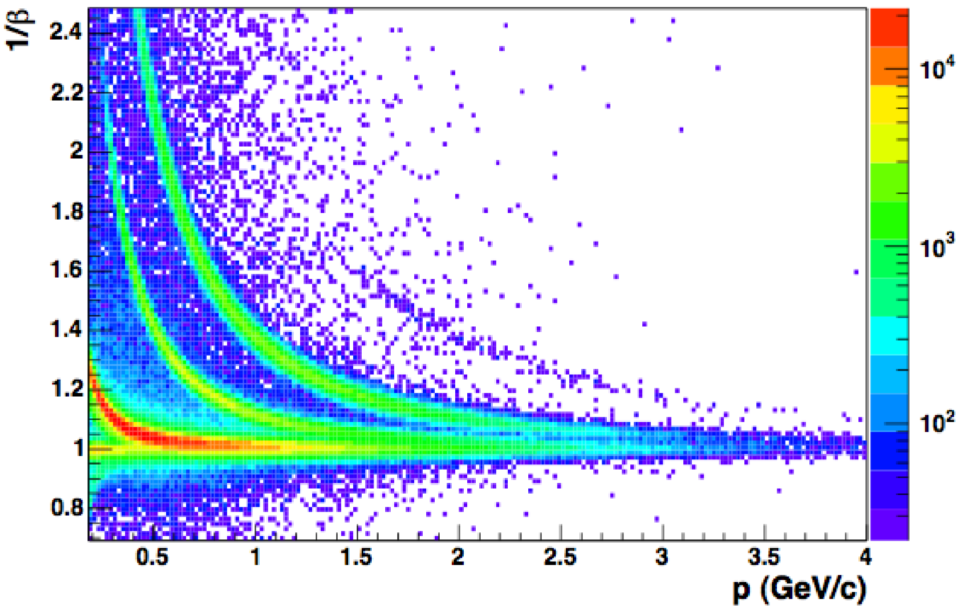

Figure 7.4: $1/\beta$ vs. momentum for pions, kaons and (anti-)protons from the STAR TOF [109].

within the cone are summed to give a raw jet energy. The average energy of two unseeded cones is used to estimate the background energy that is then subtracted on an event by event basis for each seeded cone. In summary, jet reconstruction is feasible in heavy ion collisions and the initial jet yield results have matched reasonably well with N_{binary} scaled $p + p$ yields using the seeded cone algorithm, given the relatively large systematic errors [118].

7.2.2 Time of flight STAR upgrade

A limitation of the $\frac{dE}{dx}$ data is that it cannot be used to identify charged hadrons between momentum 1.2 - 3.0 GeV/c. A Time of Flight (TOF) detector with full azimuth coverage was 70% complete in 2009 and is now complete for the 2010 run [119]. The TOF extends the particle identification range for protons up to a momentum of 3.0 GeV/c and separates kaons from pions up till 1.6 GeV/c as shown in figure 7.4. The addition of a full azimuth coverage TOF will allow for an analysis of the identified particle spectra created in heavy ion collisions at RHIC over a large p_T range.

7.2.3 Proposed Improved jet spectra analysis

In the previous two sections, sections 7.2.1 and 7.2.2, two improvements to the analysis performed in this thesis were described. By combining the jet reconstruction algorithms with the jet spectra analysis, a more conclusive jet study could be performed. Utilising the TOF would increase the associated hadron p_T range that could be analysed. The observed increase in the $p^{\pm}/\pi^{\pm}$ ratio in central $Au + Au$ collisions ranges from p_T = 1.5 - 6 GeV/c. The entire increased range could be analysed providing a comprehensive study of the mid and low p_T jet spectra.

7.3 Final Outlook

When RHIC operations began in 2000, an era of hard probes in heavy ion collisions began. During the last ten years a large collaborative effort has been engaged in studying and understanding the strong interaction in a QCD medium. This analysis is a small part of that large collaborative effort to provide experimental evidence to complement theoretical models that are looking to quantify the critical parameters of the medium created at RHIC.

The experiment is not complete yet and there are several new avenues to explore at RHIC and future heavy ion experiments. The commissioning of the LHC at CERN in 2009 announced the arrival of a new frontier for heavy ion physics. With an anticipated $\sqrt{s_{NN}}$= 5500 GeV, the experiments at the LHC are well suited for hard probe analysis. The hadron identification method developed in this analysis may prove to be a useful technique for jet studies at ALICE. The ALICE experiment is the only purpose built heavy ions experiment at the LHC and benefits from a barrel time projection chamber. ALICE will be able to track charged particles with a momentum from 100 MeV/c to 100 GeV/c with a momentum resolution ranging from 1-10% [120]. The ALICE experiment represents an ideal tool for jet studies at the LHC.

There are new challenges to be faced at the LHC. At $\sqrt{s_{NN}}$ = 5500 GeV a $Pb + Pb$ collision is likely to yield several hard scattering events per collision due to the increased hard scattering cross section plus access to higher energy jets. Jet reconstruction may be more difficult when several dijets are present in a single event. In addition, a higher average Q^2 may lead to a less strongly coupled QGP that would have implications for energy loss models applied to LHC collisions. As the LHC will cross a new boundary in energy, there could be new and exciting physics that have yet to be observed in any high energy experiment.

References

[1] David J. Gross and Frank Wilczek. Ultraviolet behavior of Non-Abelian Gauge Theories. *Physics Review Letter*, 30(26):1343–1346, 1973.

[2] Günther Dissertori, Ian Knowles, and Michael Schmelling. *Quantum Chromodynamics*. Oxford Science Publications, 2003.

[3] M. Gell-Mann. A schematic model of baryons and mesons. *Physics Letters*, 8(3):214, 1964.

[4] Ch. Berger et al. Evidence for gluon bremsstrahlung in e^+ e^- annihilations at high energies. *Physics Letters B*, 86(3-4):418, 1979.

[5] Manfred Böhm, Ansgar Denner, and Hans Joos. *Gauge Theories of the strong and electroweak interaction*. B. G. Teubner, 2001.

[6] ALEPH Collaboration. Measurement of α_s from scaling violations in fragmentation fuctions in e^+e^- annihilation. *Physics Letters B*, 357:487–499, 1995.

[7] L3 Collaboration. Study of hadronic events and measurements of α_s between 30 and 91 GeV. *Physics Letters B*, 411(3-4):339, 1997.

[8] J. C. Collins and M. J. Perry. Superdense matter: Neutrons or asymptotically free quarks? *Physics Review Letter*, 34:1353–1356, 1975.

[9] N. F. Mott. Metal-insulator transition. *Reviews of Modern Physics*, 40(4):677–683, 1968.

[10] Gao and Mingshen. Debye screening in the QCD gluonic plasma. *Physics Review Letter D*, 41(2):626–633, Jan 1990.

[11] F. Karsch. Lattice Results on QCD Thermodynamics. *Nuclear Physics*, A(698):199c–208c, 2002.

[12] Dirk H. Rischke. The quark-gluon plasma in equilibrium. *Prog.Part.Nucl.Phys*, 52:197–296, 2004.

[13] Peter Braun-Munzinger and Johanna Stachel. The quest for the quark-gluon plasma. *Nature*, 442:302–309, 2007.

[14] J. Bjorken. Highly relativistic nucleus-nucleus collisions: The central rapidity region. *Physics Review Letter*, 27(1), 1983.

[15] S. A. Bass et al. Microscopic models for ultrarelativistic heavy ion collisions. *Prog.Part.Nucl.Phys*, 41:255–369, 1998.

[16] BRAHMS Collaboration. Quark gluon plasma and color glass condensate at RHIC? The perspective from the BRAHMS experiment. *Nuclear Physics*, A757:1–27, 2005.

[17] PHENIX Collaboration. Formation of dense partonic matter in the relativistic nucleus-nucleus collisions at RHIC: Experimental evaluation by the PHENIX collaboration. *Nuclear Physics A*, 757:184–283, 2005.

[18] PHOBOS Collaboration. The PHOBOS Perspective on Discoveries at RHIC. *Nuclear Physics A*, 757:28–101, 2005.

[19] STAR Collaboration. Experimental and Theoretical Challenges in the Search for the Quark Gluon Plasma: The STAR Collaboration's Critical Assessment of the Evidence from RHIC Collisions. *Nuclear Physics A*, 757:102–183, 2005.

[20] J. Bjorken. Energy loss of energetic partons in quark-gluon plasma: Possible extinction of high p_t jets in hadron-hadron collisions. *FERMILAB-PUBLICATIONS*, 82(059), 1982.

[21] Sangyong Jeon and Joseph Kapusta. Linear extrapolation of ultrarelativistic nucleon-nucleon scattering to nucleus-nucleus collisions. *Physics Review Letter C*, 56(1):468–480, 1997.

[22] STAR Collaboration. Evidence from d+Au measurements for final-state suppression of high-p_{T} in Au+Au collisions at RHIC. *Physics Review Letter*, 91(072304), 2003.

[23] D. Antreasyan and J. W. Cronin et al. Production of hadrons at large transverse momentum in 200-, 300, and 400-GeV p-p and p-nucleus collisions. *Physics Review Letter D*, 19(3):764 – 778, 1979.

[24] STAR Collaboration. Centrality Dependence of High-p_{T} hadron Suppression in Au+Au collisions at $\sqrt{s_{\mathrm{NN}}}$ = 130 GeV. *Physics Review Letter*, 89(202301), 2002.

[25] PHENIX Collaboration. Centrality Dependence of Direct Photon Production in $\sqrt{s_{NN}}$ = 200 GeV Au + Au Collisions. *Physics Review Letter*, 94(23), 2005.

[26] PHENIX Collaboration. Common Suppression Pattern of η and π^0 Mesons at High Transverse Momentum in Au+Au Collisions at $\sqrt{S_{NN}}$ = 200 GeV. *Physics Review Letter*, 96(20), 2006.

[27] Raghunath Sahoo et al. Probing the QGP Phase Boundary and Estimation of Plasma Lifetime with Thermal Propertes of ϕ Mesons. *Physics Review Letter C*, arXiv:1007.4335v1, 2010.

[28] V. Hedberg et al. Study of Jet reconstruction algorithms for deep inelastic events at HERA. *Zeitschrft Fur Physik C - Particles and Fields*, 63(1):49–62, 1994.

[29] J. Ashkin and R. E. Marshak. Bremsstrahlung in high energy nucleon-nucleon collisions. *Physics Review Letter*, 76(1):58–60, 1949.

[30] STAR Collaboration. Disappearance of back-to-back high-p_{T} hadron correlations in central Au+Au collisions at $\sqrt{s_{\mathrm{NN}}}$ = 200 GeV. *Physics Review Letter*, 90(082302), 2003.

[31] STAR Collaboration. Direct observation of dijets in central Au+Au collsions at $\sqrt{s_{\mathrm{NN}}}$ = 200 GeV. *Nuclear Physics*, A774:573–576, 2006.

[32] P. F. Kolb, J. Sollfrank, and U. Heinz. Anisotropic flow from AGS to LHC energies. *Physics Letters B*, 459:667–673, 1999.

[33] H. Sorge. Soft transverse expansion in PB(158 AGeV) on Pb collisions: preequilibrium motion or first order phase transition. *Physics Letters B*, 402:251–256, 1997.

[34] P. F. Kolb, J. Sollfrank, and U. Heinz. Anisotropic transverse flow and the quark-hadron phase transition. *Physics Review Letter C*, 62(5), 2000.

[35] S. Voloshin and Y. Zhang. Flow study in relativistic nuclear collisions be fourier expansion of the azimuthal particle distributions. *Zeitschrft Fur Physik C - Particles and Fields*, 70:665–672, 1996.

[36] STAR Collaboration. Elliptic flow in Au + Au collisions at $\sqrt{s_{\mathrm{NN}}}$ = 130 GeV. *Physics Review Letter*, 86(402), 2001.

[37] STAR Collaboration. Azimuthal Anisotropy in Au + Au Collisions at $\sqrt{s_{NN}}$ = 200 GeV. *Physics Review Letter C*, 72(14904), 2005.

[38] PHENIX Collaboration. Scaling Properties of Azimuthal Anisotropy in Au + Au and Cu + Cu Collisions at $\sqrt{s_{NN}}$ = 200 GeV. *Physics Review Letter*, 98(162301), 2007.

[39] STAR Collaboration. Identified baryon and meson distributions at large transverse momenta from Au + Au collisions at $\sqrt{s_{NN}}$ = 200 GeV. *Physics Review Letter*, 97(152301), 2006.

[40] Dénes Molnár and Sergei A. Voloshin. Elliptic flow at large transverse momenta from quark coalescence. *Physics Review Letter*, 91(9), 2003.

[41] R. J. Fries et al. Hadron production in heavy ion collisions: Fragmentation and recombination from a dense parton phase. *Physics Review Letter C*, 68(4), 2003.

[42] R. J. Fries et al. Hadronisation in heavy ion collisions: Recombination and fragmentation of partons. *Physics Review Letter*, 90(20), 2003.

[43] C. Nonaka et al. Hadronisation at RHIC: interplay of recombination and fragmentation. *Acta Physica Hungarica A - Heavy Ion Physics*, 24(1-4):227–233, 2005.

[44] Rudolf C. Hwa and C. B. Yang. Recombination of shower partons at high p_T in heavy-ion collisions. *Physics Review Letter C*, 79(024905), 2004.

[45] N. Werner. Measurements of proton structure functions, α_s and parton distribution functions at HERA. *arXiv:hep-ex/0305109v2*, 2003.

[46] Daniel de Florian. Resummed cross section for jet production at hadron colliders. *Physics Review Letter D*, 76(074031), 2007.

[47] B. A. Kniehl, G. Kramer, and B. Pötter. Fragmentation functions for pions, kaons, and protons at next-to-leading order. *Nuclear Physics B*, 582:514–536, 2000.

[48] UA1 Collaboration. Jet fragmentation into charged particles at the CERN proton-antiproton collider. *Physics Letters B*, 132(1-3):223–229, 1983.

[49] SLD Collaboration. Production of π^+, K^+, K^0, K^{*0}, ϕ, p and Λ^0 in hadronic Z^0 decays. *Physics Review Letter D*, 59(052001), 1999.

[50] S. Kretzer. Fragmentation functions from flavor-inclusive and flavor-tagged e^+e^- annihilation. *Physics Review Letter D*, 62(054001), 2000.

[51] G. Boca et al. Average fraction of jet momentum carried by high p_t to leading hadrons. *Zeitschrft Fur Physik C - Particles and Fields*, 49(4):543–553, 1991.

[52] M. Jacob. Large Transverse Momentum and Jet Studies. *Physics Reports*, 48(4):285–350, 1978.

[53] B. Andersson et al. Parton fragmentation and string dynamics. *Physics Reports*, 97(2-3):31–145, July 1983.

[54] R. D. Field and R. P. Feynman. A parametrization of the properties of quark jets. *Nuclear Physics B*, 136(1):1–76, 1978.

[55] R. D. Field and S. Wolfram. A QCD model for e^+e^- annihilation. *Nuclear Physics B*, 213(65), 1983.

[56] J.-C. Winter, F. Krauss, and G. Soff. A modified cluster-hadronisation model. *The European Physical Journal C*, 36(3):381–395, 2004.

[57] H. Aihara et al. Tests of models for quark and gluon fragmentation in e^+e^- annihilation at $\sqrt{s} = 29$ GeV. *Zeitschrft Fur Physik C - Particles and Fields*, 28(1):31–44, 1985.

[58] Klaus Geiger. Particle production in high-energy nuclear collisions: Parton cascade-cluster hadronisation model. *Physics Review Letter D*, 47(1):133–159, 1993.

[59] Andrey Korytov. Soft QCD phenomena in events with high-E_T jets at Tevatron. *European Physical Journal C*, 33(s01):s425–s326, 2004.

[60] Xavier Artru. Classical string phenomenology. how strings work. *Physics Reports*, 97(2-3):147–171, 1983.

[61] H. Aihara et al. Tests of Models for Parton Fragmentation by means of Three-Jet Events in e^+e^- annihilation at $\sqrt{s} = 29$ GeV. *Physics Review Letter*, 54(270), 1985.

[62] Xavier Artru. String model with baryons: Topology; classical motion. *Nuclear Physics B*, 85(2):442–460, 1975.

[63] B. Andersson, G. Gustafson, and T. Sjostrand. Baryon production in jet fragmentation and upsilon-decay. *Physica Scripta*, 32(6):574–580, 1985.

[64] H. Aihara et al. Baryon Production in e^+e^- Annihilation at $\sqrt{s} = 29$ GeV: Clusters or Diquarks? *Physics Review Letter*, 55(10):1047–1050, 1985.

[65] OPAL Collaboration. Evidence for chain-like production of strange baryon pairs in jets. *Physics Letters B*, 305(4):415–427, 1993.

[66] TOPAZ Collaboration. Study of baryon production mechanism in e^+e^- annihilation into hadrons. *Physics Letters B*, 440(3-4):386–392, 1998.

[67] K. J. Eskola, V. J. Kolhinen, and P. V. Ruuskanen. Scale evolution of nuclear parton distributions. *Nuclear Physics B*, 535:351–371, 1998.

[68] Rudolf Baier, Alex Kovner, and Urs Achim Wiedermann. Saturation and parton level Cronin effect: Enhancement verses suppression of gluon production in p-A and A-A collisions. *Physics Review Letter D*, 68(5), 2003.

[69] K. J. Eskola, H. Paukkunen, and C A. Salgado. An improved global analysis of nuclear parton distribution functions including RHIC data. *JHEP*, 7(102), 2008.

[70] BRAHMS Collaboration. Evolution of the Nuclear Modification Factors with Rapidity and Centrality in d + Au Collisions at$\sqrt{s_{NN}}$ = 200 GeV. *Physics Review Letter*, 93(242203), 2004.

[71] Xin-Nian Wang, Miklos Gyulassy, and Michael Plümer. Landau-Pomeranchuk-Migdal effect in QCD and radiative energy loss in a quark-gluon plasma. *Physics Review Letter D*, 51(7):3436–3446, 1995.

[72] R. Baier, Yu. L. Dokshitzer, A. H. Mueller, S. Peigné, and D. Schiff. Radiative energy loss of high energy quarks and gluons in a finite volume quark-gluon plasma. *Nuclear Physics B*, 483:291–320, 1997.

[73] A. Dainese, C. Loizides, and G. Paic. Leading-particle suppression in high energy nucleus-nucleus collisions. *European Physical Journal C*, 38(4):461–474, 2005.

[74] K. J. Eskola et al. The fragility of high p_T hadron spectra as a hard probe. *Nuclear Physics A*, 747:511–529, 2005.

[75] M. Gyulassy, P. Levai, and I. Vitev. Reaction operator approach to non-abelian energy loss. *Nuclear Physics B*, 594:371–419, 2001.

[76] P. Levai et al. Discovery of Jet Quenching at RHIC and the Opacity of the Produced Gluon Plasma. *Nuclear Physics A*, 698:631–634, 2001.

[77] I. Vitev. Testing the theory of QGP-induced energy loss at RHIC and the LHC. *Physics Letters B*, 639:38–45, 2006.

[78] PHENIX Collaboration. Nuclear Modification of Electron Spectra and Implications for Heavy Quark Energy Loss in Au + Au collisions at $\sqrt{S_{NN}}$ = 200 GeV. *Physics Review Letter*, 96(032301), 2006.

[79] Yu. L. Dokshitzer and D. E. Kharzeev. Heavy-quark colorimetry of QCD matter. *Physics Letters B*, 519(3-4):199–206, 2001.

[80] Jan e Alam, Abhee K. Dutt-Mazumder, and Pradip Roy. Collisional energy loss and the suppression of high p_{T} hadrons. *Nuclear Physics*, A785:245c–248c, 2007.

[81] Carlos A. Salgado and Urs Achim Wiedermann. Calculating quenching weights. *Physics Review Letter*, D68(014008), 2003.

[82] A. Majumder. A comparative study of jet-quenching schemes. *Journal of Physics G: Nuclear Particle Physics*, 34(8), 2007.

[83] Sebastian Sapeta and Urs Achim Wiedermann. Jet hadrochemistry as a characteristic of jet quenching. *European Physical Journal C*, 55(2), May 2008. CERN-PH-TH/2007-111.

[84] R. Kirschner. Jet properties and the parton interpretation of the leading logarithmic approximation scheme. *Journal of Physics G: Nuclear Particle Physics*, 6:569–582, 1980.

[85] Y. I. Azimov et al. Similarity of parton and hadron spectra in QCD jets. *Zeitschrft Fur Physik C - Particles and Fields*, 27(1):65–72, 1985.

[86] CDF Collaboration. Momentum distribution of charged particles in jets in dijet events in $p\bar{p}$ collisions at $\sqrt{s}$ 1.8 TeV and comparisons to perturbative QCD predictions. *Physics Review Letter D*, 68(012003), 2003.

[87] STAR Collaboration. Longitudinal double-spin asymmetry and cross section for inclusive jet production in polarized prton collisions at $\sqrt{s} = 200$ GeV. *Physics Review Letter*, 97(25), 2006.

[88] DELPHI Collaboration. Identified charged particles in quark and gluon jets. *European Physical Journal C*, 17(2):207–222, 2000.

[89] W. Liu and R. J. Fries. Probing nuclear matter with jet conversions. *Physics Review Letter C*, 77(5), 2008.

[90] S. Jeon, J. Jalilian-Marian, and I. Sarcevic. Prompt Photon and Inclusive π^0 Production at RHIC and LHC. *Nuclear Physics*, A715:795c–798c, 2003.

[91] Sangyong Jeon, Jamal Jalilian-Marian, and Ina Sarcevic. The Origin of Large-p_T π^0 Suppression at RHIC. *Physics Letters B*, 562(1-2):45–50, 2003.

[92] H. Hahn et al. The RHIC design overview. *Nuclear Instruments and Methods in Physics Research Section A*, 499(2-3):245–263, 2003.

[93] STAR Collaborationr. STAR detector overview. *Nuclear Instruments and Methods in Physics Research Section A*, 499(2-3):624–632, 2003.

[94] PHENIX Collaboration. PHENIX detector overview. *Nuclear Instruments and Methods in Physics Research Section A*, 499(2-3):469–479, 2003.

[95] BRAHMS Collaboration. The BRAHMS experiment at RHIC. *Nuclear Instruments and Methods in Physics Research Section A*, 499(2-3):437–468, 2003.

[96] PHOBOS Collaboration. The PHOBOS detector at RHIC. *Nuclear Instruments and Methods in Physics Research Section A*, 499(2-3):603–623, 2003.

[97] M. Anderson et al. The STAR Time Projection Chamber: A Unique Tool for Studying High Multiplicity Events at RHIC. *Nuclear Instruments and Methods*, A499(659), 2003.

[98] M. Beddo et al. The STAR Barrel Electromagnetic Calorimeter. *Nuclear Instruments and Methods*, A499(725), 2003.

[99] F. S. Bieser et al. The STAR trigger. *Nuclear Instruments and Methods in Physics Research Section A*, 499:766–777, 2003.

[100] Hans Bichsel. Comparison of Bethe-Bloch and Bichsel functions. STAR Note SN0439, March 2002.

[101] Hans Bichsel. PARTICLE IDENTIFICATION AT STAR-TPC WITH IONIZATION MEASUREMENTS. In M. Barone, editor, *Astroparticle, Particle and Space physics, Detector and Medical Physics application*, volume 8th. World Scientific, October 2003.

[102] W. M. Yao et al. Review of particle physics. *Journal of Physics*, G33(1), 2006.

[103] Hans Bichsel. A method to improve tracking and particle identification in TPCs and silicon detectors. *Nuclear Instruments and Methods in Physics Research Section A*, 562:154–197, 2006.

[104] STAR Collaboration. $\Delta\phi\Delta\eta$ Correlations in Central Au+Au collisions at $\sqrt{s_{\mathrm{NN}}}$ = 200 GeV. *Physics Review Letter*, C75(034901), 2007.

[105] Thomas Dietel. Azimuthal correlations of high p_{T} photons and hadrons in AuAu collisions at RHIC. *Nuclear Physics*, A774:569–572, 2006.

[106] STAR Collaboration. Transverse-momentum p_{T} correlations on (η, ϕ) from mean p_{T} fluctuations in Au+Au collisions at $\sqrt{s_{\mathrm{NN}}}$ = 200 GeV. *Journal of Physics*, G32(L37), 2006.

[107] Léon Gaillard. *A study of jets at the STAR experiment at the relativistic heavy ion collider via two particle correlations*. PhD thesis, University of Birmingham, 2008.

[108] S. Wicks et al. Elastic, inelastic, and path length fluctuations in jet tomography. *Nuclear Physics A*, 784:426–442, 2007.

[109] M. Shao et al. Extensive Particle Identification with TPC and TOF at STAR Experiment. *Nuclear Instruments and Methods*, A558:419–429, 2006.

[110] B. I. Abelev. High p_T correlations with strange particle in STAR. *Journal of Physics G: Nuclear Particle Physics*, 35(044010), 2008.

[111] Anne Sickles. Identified particle jet correlations from PHENIX. *Journal of Physics G: Nuclear Particle Physics*, 34:S685–S688, 2007.

[112] STAR Collaboration. Measurements of Strange Particle Production in $p+p$ Collisions at $\sqrt{s}$= 200 GeV. *Physics Review Letter C*, 75(064901), 2007.

[113] Y. Xu et al. Calibration of ionization energy loss at relativistic rise with STAR Time Projection Chamber. arXiv:0807.4303v1.

[114] A. M. Hamed. Modified fragmentation function in heavy ion collisions at RHIC via direct γ-jet measurements. *European Physical Journal C*, 61:597–601, 2009.

[115] V. S. Pantuev. ”Jet - Ridge” effect in heavy ion collisions as a back splash from stopped parton. *arXiv:0710.1882v1 [hep-ph]*, 2007.

[116] N. K. Pruthi. Elliptic flow and the high p_T ridge in Au + Au collisions. *European Physical Journal C*, 62:165–167, 2009.

[117] G. L. Ma et al. Longitudinal broadening of near-side jets due to parton cascade. *European Physical Journal C*, 57:589–593, 2008.

[118] Sevil Salur. A short review of jet identification. *European Physical Journal C*, 62:119–125, 2009.

[119] J. Wu and M. Xu. A barrel TOF for STAR at RHIC. *Journal of Physics: Nuclear Particle Physics*, G34:5729–5732, 2007.

[120] Andreas Morsch. Jet physics in heavy-ion collisions at the LHC with the ALICE detector. *Journal of Physics: Nuclear Particle Physics*, G31:5597–5602, 2005.